AFRL-RV-HA-TR-2010-1067

SEISMIC OBSERVATIONS AND INTERPRETATION IN NE CHINA, INFRASOUND OBSERVATIONS AND INTERPRETATION IN UTAH

Rong Mao Zhou, Tae Sung Kim, Relu Burlacu, Brian W. Stump, Chris Hayward, Zhi-Xian Yang, Yun-Tai Chen, Robert B. Herrmann, Stephen Arrowsmith, Kristine Pankow, Sue Nava, Jessie Bonner, Sebastian Hoch, David Whiteman, Aileen Fisher, Ray Kubacki, Mark Leidig, James Britton, David Drobeck, Pete O’Neill, Kevin Jensen, Ken Whipp, Gordon Johanson, Paul Roberson, Ray Read, Ronald Brogan and Steve Masters

Southern Methodist University
Roy M. Huffington Department of Earth Sciences
PO Box 750395
Dallas, Texas 75275-0395

Final Report

30 July 2010

AIR FORCE RESEARCH LABORATORY
Space Vehicles Directorate
29 Randolph Rd
AIR FORCE MATERIEL COMMAND
HANSCOM AFB, MA 01731-3010

NOTICES

AFRL-RV-HA-TR-2010-1067 HAS BEEN REVIEWED AND IS APPROVED FOR PUBLICATION IN ACCORDANCE WITH ASSIGNED DISTRIBUTION STATEMENT.

//signature//	//signature//
ROBERT J. RAISTRICK	Domenic Thompson, Maj, USAF, Chief
Contract Manager	Battlespace Surveillance Innovation Center

REPORT DOCUMENTATION PAGE

Form Approved
OMB No. 0704-0188

1. REPORT DATE
30-Jul-2010

2. REPORT TYPE
Final Report

3. DATES COVERED *(From - To)*
16-Apr-2005 to 15-Apr-2010

4. TITLE AND SUBTITLE
Seismic Observations and Interpretation in NE China, Infrasound Observations and Interpretation in Utah

5a. CONTRACT NUMBER
FA8718-05-C-0020

5b. GRANT NUMBER

5c. PROGRAM ELEMENT NUMBER
62601F

6. AUTHOR(S)
Rong Mao Zhou, Tae Sung Kim, Relu Burlacu, Brian W. Stump, Chris Hayward, Zhi-Xian Yang, Yun-Tai Chen, Robert B. Herrmann, Stephen Arrowsmith, Kristine Pankow, Sue Nava, Jessie Bonner, Sebastian Hoch, David Whiteman, Aileen Fisher, Ray Kubacki, Mark Leidig, James Britton, David Drobeck, Pete O'Neill, Kevin Jensen, Ken Whipp, Gordon Johanson, Paul Roberson, Ray Read, Ronald Brogan and Steve Masters

5d. PROJECT NUMBER
1010

5e. TASK NUMBER
SM

5f. WORK UNIT NUMBER
A1

7. PERFORMING ORGANIZATION NAME(S) AND ADDRESS(ES)

Southern Methodist University
Roy M. Huffington Department of Earth Sciences
PO Box 750395
Dallas, Texas 75275-0395

8. PERFORMING ORGANIZATION REPORT NUMBER

9. SPONSORING / MONITORING AGENCY NAME(S) AND ADDRESS(ES)

Air Force Research Laboratory
29 Randolph Rd.
Hanscom AFB, MA 01731-3010

10. SPONSOR/MONITOR'S ACRONYM(S)
AFRL/RVBYE

11. SPONSOR/MONITOR'S REPORT NUMBER(S)
AFRL-RV-HA-TR-2010-1067

12. DISTRIBUTION / AVAILABILITY STATEMENT

Approved for Public Release; Distribution Unlimited.

13. SUPPLEMENTARY NOTES

14. ABSTRACT

A set of fifteen broadband seismic instruments provided to the project by the Program for Array Seismic Studies for Continental Lithosphere (PASSCAL) were deployed in NE China for the purposes of characterizing both the regional structure of the area as well as record local seismic events. During the course of this project the instruments were installed in two separate areas. The first deployment was in and around the Yanqing-Huailai Basin, NW of Beijing. The first chapter in this report documents a portion of the data recorded by this deployment and the utilization of regional and teleseismic signals to constrain the crust and upper mantle structure in the region. This paper has been published in Bulletin of the Seismological Society of America. The second instrument deployment was in the Haicheng and Xiuyan Area of NE China, the location of the 1975 Haicheng Earthquake. The second chapter of this report documents the analysis of regional and teleseismic data from this deployment and the resulting crust and upper mantle for the region. The infrasound component of this project involved the installation and operation of three infrasound arrays in Utah as well as the experimental support of a separately funded project to quantify infrasound signals from large surface explosions conducted at the Utah Test and Training Range (UTTR). The third chapter documents infrasonic observations from the Wells Nevada earthquake sequence that occurred during this deployment. The fourth chapter describes the experimental characterization of the UTTR explosions. The fifth chapter documents an analysis and modeling effort of regional infrasound observations from the UTTR explosions in order to quantify the time varying nature of the atmosphere.

15. SUBJECT TERMS
Seismology, Infrasound, Receiver functions, Crustal structure

16. SECURITY CLASSIFICATION OF:			**17. LIMITATION OF ABSTRACT**	**18. NUMBER OF PAGES**	**19a. NAME OF RESPONSIBLE PERSON**
a. REPORT	**b. ABSTRACT**	**c. THIS PAGE**			Robert Raistrick
UNC	UNC	UNC	SAR	131	**19b. TELEPHONE NUMBER** *(include area code)* 781-377-3726

Table of Contents

Figures

Tables

Foreword

A set of fifteen broadband seismic instruments provided to the project by the Program for Array Seismic Studies for Continental Lithosphere (PASSCAL) were deployed in NE China for the purposes of characterizing both the regional structure of the area as well as record local seismic events. During the course of this project the instruments were installed in two separate areas. The first deployment was in and around the Yanqing-Huailai Basin, NW of Beijing. The first chapter in this report documents a portion of the data recorded by this deployment and the utilization of regional and teleseismic signals to constrain the crust and upper mantle structure in the region. This paper has been published in Bulletin of the Seismological Society of America. The second instrument deployment was in the Haicheng and Xiuyan Area of NE China, the location of the 1975 Haicheng Earthquake. The second chapter of this report documents the analysis of regional and teleseismic data from this deployment and the resulting crust and upper mantle for the region. The infrasound component of this project involved the installation of operation of three infrasound arras in Utah as well as the experimental support of a separately funded project to quantify infrasound signals from large surface explosions conducted at the Utah Test and Training Range (UTTR). The third chapter documents infrasonic observations from the Wells Nevada earthquake sequence that occurred during this deployment. The fourth chapter describes the experimental characterization of the UTTR explosions. The fifth chapter documents an analysis of modeling effort of regional infrasound observations from UTTR explosions in order to quantify the time varying nature of the atmosphere.

CHAPTER 1

Teleseismic Receiver Function and Surface Wave Study of Velocity Structure Beneath the Yanqing-Huailai Basin, NW of Beijing

Authors: Rong-Mao Zhou(1), Brian W. Stump (2), Robert B. Herrmann (3)
Zhi-Xian Yang and Yun-Tai Chen(4)

Affiliation and Addresses of Authors:

(1) Geophysics Group, MS D443
Los Alamos National Laboratory
Los Alamos, NM 87544, USA
(2) Roy M. Huffington Department of Earth Sciences
Southern Methodist University
Dallas, TX 75275, USA
(3) Department of Earth & Atmospheric Sciences
Saint Louis University
St. Louis, MO 63103, USA
(4) Institute of Geophysics
China Earthquake Administration
Beijing, P. R. China, 100081

E-mail Addresses:
rzhou@lanl.gov (R.-M. Z.), bstump@smu.edu (B. W. S.), rbh@eas.slu.edu (R. B. H.)
zhixiany@cea-igp.ac.cn (Z.-X. Y.) and chenyt@cea-igp.ac.cn (Y.-T. C.)
Phone: 1-505-606-0839 (R.-M. Z.)
Fax: 1-505-667-8487

Published (2009) **Bulletin of Seismological Society of America, 99**, 1937-1952.

ABSTRACT

Shear wave velocities beneath the Yanqing-Huailai Basin, 90 – 140 km northwest of Beijing are estimated from the joint inversion of surface wave phase velocities and teleseismic receiver functions. The data set is from a temporary broadband seismic network supported by PASSCAL in the basin and includes 34 teleseismic events from 2003 to 2005. Receiver functions from the teleseismic events are similar for the stations around the Yanqing-Huailai Basin and exhibit little variation with azimuth. The velocity models constrained by receiver functions and surface wave dispersion curves are also similar. The resulting models reflect the low-velocity basin sediments to 2 km followed by a positive velocity gradient to 15 km with shear wave velocity increasing from 2.0 to 3.55 km/sec. Evidence of a mid-crust low-velocity layer starts at 15 km with a shear velocity decrease to 3.3 km/sec that extends to approximately 25 km. The total crustal thickness is 38 to 42 km with a smooth Moho transition to an upper mantle shear velocity of 4.3 km/sec. The low velocity zone is consistent with recent extension, geothermal activity, and earthquake locations above this depth. The average shear velocity model for the basin has similarities to other regional and global models, but provides more detailed structure in the uppermost and lower portions of the crust. The new model includes the effect of the sediments in the basin, the low velocity layer, and the gradual Moho transition. Predicted P and S travel times are 1 to 3.5 seconds slower than the previous models at regional distances.

INTRODUCTION

Motivation

The Yanqing-Huailai Basin is the geographic focus of this study and is one of the extensional features in the North China Block (NCB). It is located between 40°00′N – 40°38′N and 115°04′E – 116°14′E, 90 to 140 km northwest of Beijing, China (Fig. 1b and 1c) and is part of the active Zhangjiakou-Bohai seismic zone that passes through the northern part of China (Zhao *et al.*, 2005). Eight historic earthquakes with magnitude greater than 5 have occurred in the Yanqing-Huailai region since 294AD (Zhang *et al.*, 1996) and thus earthquake risk assessment is important in light of the population of near-by Beijing and other large cities. Numerous underground mines in the region regularly experience rock bursts and collapses resulting in the disruption of mining operations. Development of crust and upper mantle models for this region are designed to improve the understanding of crustal development, the occurrence of earthquakes and mine related events and the locations of seismic events in the region. The political and economic importance of this region has motivated a number of geophysical studies in the area, including refraction/wide-angle reflection surveys (Zhang *et al.*, 1996; Zhu *et al.*, 1997; and Zhao *et al.*, 2005); a large earthquake risk study (Liu *et al.*, 1997); a neotectonics and seismicity study (Wu *et al.*, 1979) and a tectonic stress study (Xu *et al.*, 1997) that provide a foundation for our study.

Regional Tectonic Setting

The Yanqing-Hualai Basin is in the NCB, part of the Sino-Korean Block, the largest and oldest cratonic region in China, with a total area greater than 1,500,000 km^2 (Figure 1). It is bordered to the north by the Yinshan-Yanshan orogenic belt, to the south by the Qingling-Dabie belt and extends into the Gulf of Bohai and the northern Yellow Sea to the east (Rowley et al., 1997; Zhao et al., 1999; Zhao et al., 2002; and Lin et al., 2004). As discussed and modeled by Lin et al., 2004, the NCB has undergone two distinct phases of tectonics and resulting crustal deformation that affects the velocity structure and seismicity in the region. Their modeling shows that the first phase involved N-S compression and explains compressional structures including the two bounding E-W orogenic belts and crustal thickening before the late Jurassic. The second phase of deformation is responsible for NNE-trending extensional basins in the region and suggests E–W-directional crustal stretching and thinning during the late Mesozoic moderated by the Tan-Lu fault to the east.

Seismicity – NCB

The NCB is currently a region of intraplate seismicity and active crustal deformation. The China Historical Earthquake Catalogue Database (World Data Center for Seismology, Beijing, http://210.72.96.21:8080/wdc/cezhen/historycatalog_query.jsp) and the China Seismograph Network (CSN) Catalog (http://210.72.96.165/wdcd/csn_catalog_p001.jsp) list a total of 323 earthquakes with magnitude greater than 4.0 in the region occurring between 231B.C. and 2002, with 36 events larger than magnitude 6.0 including the destructive Tangshan earthquake of 1976. Recent seismicity (January 01, 2002 through December 31, 2006) in the Capital Circle Region (Longitude: 114°E-120°E; Latitude: 38.5°N-41°N) is well constrained by the Capital Circle Seismic Network (http://www.csndmc.ac.cn/newweb/data.htm#) (Fig. 1b).

Yanqing-Hualai Basin

The Yanqing-Huailai Basin consists of four intermountain basins: Yanqing, Huailai, Fanshan and Zhuolu extending in a NNE-SSW direction. These represent sub parallel elongated half-grabens bounded by normal faults to the NNW (Pavlides *et al.*, 1999) and reflect the crustal stretching introduced earlier. The basin basement is composed of Archaean metamorphic rocks, Proterozoic and Palaeozoic dolomites, gneisses and clastic rocks, interbedded with thin layers of coal as well as Mesozoic volcanics (andesite, rhyolite, tuff) and pyroclastics. Granitic and granodioritic bodies intruded into the Proterozoic and Palaeozoic rocks of the area from the late Jurassic to the Cretaceous. Mafic dykes are aligned along NNE–SSW tectonic structures. Sedimentation in the basins, initiated in the Pliocene, produced deposits of cemented gravels, overlain by clays, marls, sands and unconsolidated conglomerates in the middle and upper parts (Pavlides *et al.*, 1999). An unconformity exists between Pliocene and Pleistocene sediments with the younger deposits consisting of fluvial and lacustrine sands, gravels, silts, and clays interbedded with palaeosoil layers. Total estimated Pliocene sediment thickness reaches 1500 m, with Pleistocene thicknesses of 800 m (Wu *et al.*, 1979). These layer thicknesses decrease as the southern edge of the basin is approached in the half-graben structure (Pavlides *et al.*, 1999).

Two, large historic earthquakes have occurred in Yanqing-Huailai Basin: the Huailai earthquake (magnitude 6.5) on September 8, 1337; and the Shacheng earthquake (magnitude 6.75), on July 12, 1720 (Fig. 1c). The Beijing Telemetered Seismograph Network operated by the China Seismological Bureau (now China Earthquake Administration) provides enhanced earthquake monitoring capability in this area and records 15 to 20 earthquakes with magnitude equal or greater than 2.0 every year in the Yanqing-Huailai basin and its adjoining area (Chen *et al.*, 1998). A M_L 4.1 earthquake occurred in the Yanqing-Huailai Basin on July 20, 1995, followed by approximately 450 aftershocks (Chen *et al.*, 1998). Xu *et al.* (1999 and 2001). Chen *et al.* (2005) have studied the rupture process and focal mechanism of this earthquake and the following earthquake sequence.

Analysis Approach

We follow previous approaches and develop velocity models for the study area using the joint inversion of surface wave dispersion and receiver functions. Data were recorded by 7 temporary broadband seismic stations deployed in and around the Basin (Fig. 1, Table 1) that were part of the temporary broadband seismic network operated by the Southern Methodist University (SMU) and the Institute of Geophysics, China Earthquake Administration (IGPCEA) with support from the IRIS (Incorporated Research Institutions for Seismology) PASSCAL (Program for Array Seismic Studies of the Continental Lithosphere) Instrument Center (Zhou *et al.*, 2003a).

Teleseismic receiver functions have been used to provide constraints on crust and upper-mantle shear wave structure in a number of regions (Langston, 1977, 1979; Owens *et al.*, 1984; Zheng *et al.*, 2005) but the resulting models using typical problem formulation are non-unique as they contain little absolute velocity information (Ammon *et al.*, 1990). The inability to constrain absolute velocity leads to trade-offs between velocity and depth and results in a range of final velocity models with different average velocities that fit the observed receiver functions equally well. Özalaybey *et al.* (1997) addressed this non-uniqueness by proposing the joint inversion of receiver functions and surface wave phase velocities. Several authors (Du and Foulger, 1999; Julia *et al.*, 2000, 2003; and Herrmann *et al.*, 2000 and 2001; Yoo *et al.*, 2007) have determined shear-wave structures using the joint inversion of receiver functions and surface waves, and their results have illustrated the value of including even a limited band of dispersion data to reduce the trade-offs between crustal thickness and velocity. Our analysis combines local phase velocity estimates from teleseismic events with the teleseismic receiver functions in order to develop improved crust and upper mantle velocity models.

DATA SET AND ANALYSIS TOOLS

The seven, temporary, stations in the study consist of STS-2 seismometers, Quanterra Q330 data acquisition systems and Quanterra PB14 Packet Baler. Two separate vaults were constructed at each site, one for the seismometer and the other for the rest of the equipment in order to reduce noise. Seismometers were deployed in hard rock after excavating the l m x l m x l m vaults. They were covered with a 10 cm thick foam box for additional temperature stability (Zhou *et al.*, 2003a). Data were archived at the IRIS-DMC (Data Management Center).

Seismic Events

Thirty-four, high signal-to-noise ratio teleseismic events with great circle epicentral distances of 30-85 degrees occurring between 2003 and 2005 were chosen for analysis. Source parameters were obtained from the Preliminary Determination of Epicenters (PDE) bulletins provided by the United States Geology Survey (USGS) National Earthquake Information Center (NEIC) (Table 2). The distribution of the 34 teleseismic events is displayed in an azimuthal equidistant projection centered on station AYPU (Figure 2).

Receiver Functions

Receiver functions were extracted from the three-component broadband recordings of the teleseismic *P* waveforms with epicentral distances between 30° and 85° (Özalaybey *et al.*, 1997) (Figure 2). The nearly vertically incident *P* waves dominate the vertical component, while *P*-to-*S* converted waves are recorded primarily on the horizontal component. The receiver functions are sensitive to the shear-wave velocity structure beneath the station since *P* to *S* conversions make significant contributions to the horizontal components corrected for source effects (Owens *et al.*, 1984). Ammon *et al.* (1991) argue that the absolute amplitude of a receiver function provides additional constraint on the near-surface shear wave velocity and can be used to assess the presence of dipping layers (Cassidy, 1992).

Receiver functions were computed using the iterative, time-domain deconvolution technique of Ligorría and Ammon (1999), an implementation of the Kikuchi and Kanamori (1982) procedure. Three-component seismograms at six stations from a magnitude 6.2 event (Event code: 2003089; location: -3.17°N and 127.54°E on March 30, 2003) are presented in Figure 3. The radial receiver functions for the event with Gaussian filter parameter, $\alpha = 1$, are included, illustrating the strong similarity of receiver functions across the region. Low amplitude transverse components are an indication of limited anisotropic effects or non-plane layering near the stations. The radial component receiver functions ($\alpha = 1.0$) for all the events in this study at AYPU and XJYAO are plotted as a function of source azimuth in Figure 4. These receiver functions exhibit very modest azimuthal variation. Similar comparisons at other stations motivated the development of different plane layer velocity models for each station as a first step in the analysis. For the 34 events, AYPU, BAKOU, CJPU, MJPU, XJYAO, YFANG, and ZSPO recorded 27, 25, 6, 15, 27, 23 and 10 events, respectively.

Surface Waves

Phase velocities under the network are estimated applying the technique of McMechan and Yedlin (1981) to teleseismic fundamental mode Rayleigh waves. Observations at each station are projected onto a pseudo-linear array using a great circle path assumption. A p-τ stack is applied and followed by transformation into the p-ω domain in order to estimate the phase velocity dispersion curves. By simultaneously analyzing the data from the seven stations in our deployment, we assume a uniformity of structure beneath the network at depths greater than about one-third of the shortest wavelength observed.

Fundamental mode Rayleigh waves for the 34 events are extracted using Multiple Filter Analysis (Dziewonski *et al.*, 1969) followed by Phase Matched Filtering (Herrin and Goforth, 1977). An example set of fundamental mode Rayleigh waves extracted using this procedure for event 2003089 in the 20 to 100 s period range is displayed in Figure 5. Phase velocity dispersion is estimated by applying the p-τ stacking technique. The resulting mean phase velocities and standard deviations at a total of 288 frequencies for all of the events are plotted in Figure 6. The estimated phase velocities range from 3.06 to 4.06 km/s over the period range of 15 to 95 seconds with standard deviations between 0.01 and 0.28 km/s. The depth sensitivity of the Rayleigh wave phase velocity dispersion is between one-third and one-half of a wavelength (Beaty *et al.*, 2002; Li and Detrick 2006). The long-period phase velocityies help constrain the upper mantle structure. The estimated phase velocity dispersion curves display limited scatter attributable to the small array aperture, local site effects, and local departure from the assumption of a plane wave across the array. We use the estimated mean phase velocity at each frequency with the standard deviations as weights in the joint inversions.

JOINT INVERSION

Starting Model

The receiver function inversion utilizes a linearized and iterative, least-squares waveform fitting procedure (Herrmann and Ammon, 2002). Surface-wave dispersion partial derivatives are computed analytically while receiver function partial derivatives are computed numerically. The shear wave velocities in each layer are the only parameters in the inversion as a result of fixing the Vp/Vs ratio in each layer and computing layer density from the P-wave velocity after each iteration. A differential smoothing constraint is applied so that the simplest model that fits the observations is identified. The smoothing constraint is implemented by solving for the change in the velocity contrast at boundaries. The starting model has 42 plane-layers extending from surface to a depth of 200 km. Layer thicknesses are 1 km for the top 3 km (3 layers), 2 km to a depth of 5 km (1 layer), 2.5 km for 45 km (18 layers), 5 km for 50 km (10 layers), and 10 km below 100 km (10 layers). The upper 50 km of the starting model has the single velocity value of AK135-F at 50 km depth and below 50 km it follows the AK135-F continental model (Kennett *et al.*, 1992 and Montagner and Kennett, 1995). The high initial crustal velocities provide a uniform unbiased starting model for the inversion. No *a priori* assumptions were made concerning the Moho depth or the location of any internal layering in the crust. Starting with a continental upper mantle and only permitting significant departure from the starting model in the upper 80 km ensures that the lower part of the model does not depart from the experience of global seismology. We tested the model’s sensitivity to layer thicknesses in the top 50 km using: (1) 3 layers with 1 km thickness, 1 layer with 2 km thickness and 18 layers with 2 km thickness; (2) 25 layers with 2 km thickness; (3) 2 km for the top layer and 4.0 km for the rest to 50 km. These three test cases produced similar final velocity models below 2 km. Results from the first case are used for illustration taking into account the possible effects of the basin where the stations are located.

Weighting the Receiver Functions and Surface Wave Dispersion Curves in the Inversions

The goal of the joint inversion is to find a model that fits the two different types of data simultaneously. The joint inversion approach of Herrmann and Ammon (2002) includes a parameter *p* to control the relative weights applied to the receiver functions and surface wave dispersion curves. This parameter varies from 0.0 to 1.0 with 0.0 corresponding to an inversion with only the receiver functions and 1.0 to an inversion with only the surface-wave dispersion data. Figure 7 compares the inverted models using different *p* values and provides some idea of the importance of each type of data in constraining the velocity model. The partial derivatives of the surface wave dispersion curves with respect to the model parameters have values about 5 times larger than the partial derivatives of the receiver functions with respect to the model parameters. Based on these characteristics, we argue that inversions using *p* values close to 0.15 may provide the best weighting between the two types of data used in this study. This *p* value has been used by one of the authors, Herrmann, in a separate study of the Korean Peninsula (Yoo *et al.*, 2007). Herrmann found that synthetic seismograms computed from the model with *p* value of 0.15 gave the best fit to observed waveforms from an earthquake further motivating our preference for this *p* value.

Inversion Results

A joint inversion of the receiver functions and surface wave dispersion curves at each station across the Yanqing-Huailai Basin was conducted. Figure 8 illustrates the starting model in gray and the final velocity model in black with AK135F included for comparison. Observed (black) and predicted receiver functions (gray) at AYPU are also reproduced. The predicted receiver functions match the observed with 90% of the filtered radial signal power explained by the predictions for events at all azimuth and distance ranges. Observed phase velocities from teleseismic events are compared to predicted phase velocities in Figure 6.

An average velocity model for the region was determined by inverting all receiver functions from the 7 stations with the phase velocities from the teleseismic events. Figure 9 plots the station specific velocity models (dark) against the averaged model for the region (gray). The individual velocity models at depth exhibit little or no difference across the network as expected based on the common surface wave dispersion data. The models have a positive velocity gradient from the surface to approximately 15 km with shear wave velocity increasing from 2.0 km/sec to 3.55 km/sec. A slight negative gradient in velocity starts at about 15 km resulting in an extended low velocity layer to approximately 25 km with velocity near 3.3 km/sec. Subtle differences in the velocity models from ZSPO may reflect the smaller number of the events recorded at this station and its location outside of the Huailai Basin. There is evidence of a low velocity layer in the mid-crust at all stations. There is no sharp Moho interface with the Moho represented as a transition in velocity ranging from 38 to 42 km, consistent with other studies in the region (Zhang *et al.*, 1996; Zhao *et al.*, 2005). The transitional Moho, imaged with many thin layers, may be real or may a consequence of the particular data sets available, the band-limited receiver functions and dispersion data, as well as the assumption of a plane-layered underlying structure. The transitional Moho provides a good match to observed first arrival times used for earthquake location. Other authors (e.g., Fnais, 2004), have found that a transitional, rather than a sharp, Moho to be the norm.

MODEL COMPARISON AND DISCUSSION

During the instrument deployment, a 1.3 kiloton mining explosion occurred 240 to 280 km southeast of the network and generated intermediate period surface waves (2-16sec) (Zhou *et. al.*, 2003b, 2006). The vertical component seismograms from this shallow explosion superimposed with the extracted fundamental Rayleigh waves after using Multiple Filter Analysis (Dziewonski *et al.*, 1969) and Phase Matched Filtering (Herrin and Goforth, 1977) are reproduced in Figure 10. This figure also includes the mean group velocities and their standard deviations for the intermediate period surface waves estimated from the 4 stations that recorded the unique event. To explore the use of these high frequency surface waves to further constrain the shallow structures, we conducted an inversion that included these regional group velocities in addition to the teleseismic receiver functions and phase velocities. Figure 11 compares the resulting models with and without these high frequency group velocities for both AYPU and the average model for the region. The inverted models including the regional group velocities produce higher shear velocities from the surface to depth of 15 km and slightly lower velocities to the Moho. This comparison illustrates the importance of careful data set selection for the meaningful joint inversion. *Julia et al.* (2000) point out that, for joint inversion of surface wave and receiver functions, consistency requires that both signals sample the same portion of the propagating medium, so that the information contained in the waveforms references the same part of the Earth. The high frequency group velocities obtained from the mining explosion reflect the entire path effects across the Yanshan Uplift between the mine and the stations, which are different from the part of the crust sampled by the receiver functions and phase velocities estimates using the stations in and around the Huailai Basin. The fit of the dispersion curves by the resulting model that is included in Figure 10 also illustrates that the predicted group velocities are still underestimated and require even higher velocities models to fit the path effects of the Yanshan Uplift thus suggesting regional variations in the crust.

Three refraction/wide angle reflection profiles were conducted in 1993 in order to constrain the crust-mantle structures northwest of Beijing. One of these, the Beijing-Huailai-Fengzhen profile (H-20), passes in a west-to-east direction across the Yanqing-Huailai area (Figure 1. Liu *et al.*, 1997; Zhao *et al.*, 2005). The publication of the velocity models resulting from this data interpretation (Zhang *et al.*, 1996; Liu *et al.*, 1997; Zhu *et al.*, 1997; Zhao *et al.*, 2005) provides the basis for the comparison of these velocity models with our results in Figure 12. These earlier models are somewhat simpler than those produced in this study and do not include the effect of shallow basin structure nor the mid to lower crust low velocity zone.

Crustal thickness in the region identified in the refraction/reflection study was estimated between 37 and 41 km, which is consistent with our depth estimates from the joint inversion. Liu *et al.* (1997) inverted both P-wave velocity (Vp) and Vp/Vs ratio using the Seis83 program package from the Beijing-Huailai-Fengzhen (H-20) profile. Their results indicated that the crust in the Yanqing-Huailai Basin could be divided into an upper and lower part. Their model gives S wave velocities in the depth range 10 to 14 km that are similar to our models and are consistent with AK135F to 20 km depth. Predicted first arrival times of P and S waves from their models are compared to those from our work and the difference reflects the slower velocities in the very shallow crust in our models. The shallow details of our model are consistent with the known basin geology with total sediment thicknesses exceeding 2 km (Wu *et al.*, 1979). Although this study was not focused on earthquake location, our detailed velocity model could impact studies of regional earthquake location. Focal depths of historical earthquakes in the region range from 5 to 15 km, and are assumed to be located within the brittle upper crust, above the low-velocity region identified in this study and others (Zhu *et al.*, 1997). The lack of a low velocity region in the refraction interpretation illustrates the advantage of adding the receiver function and surface wave analysis to the interpretation. Che *et al.* (2001) suggest that the strength of the uppercrust has been decreased by the action of hot fluids consistent with the small and moderate earthquake locations and the existence of hot springs in the region. Detailed modeling and moment tensor inversion for the Huailai M_L event in 1995 Xu *et al*., 1999 and 2001 led to a source depth estimate of 5.5 km again in the higher velocity layers of our model. Sun *et al.* (1987) propose that the geothermal anomaly and tectonic extension are possibly related to the existence of the low velocity layers. Alternatively, Zhou and He (2002) hypothesize that the crustal low velocity layers in North China are controlled by Cenozoic rifting and mantle uplifting, which caused the rise of temperature and hence plastic deformation of the lower middle and lower crust. Our models are consistent with the existence of this mid-crustal region as a reflection of the tectonic evolution of the NCB, possibly the extensional processes discussed earlier.

CONCLUSION

Thirty-four teleseismic events recorded on 7 broadband seismic stations in and around the Yanqing-Huailai Basin have been acquired to constrain the shear velocity structure beneath and around the basin using the inversion of receiver functions and surface wave dispersion curves. The similarity of the receiver functions between stations supports the plane layered models used to represent the structure of this region. The inverted models indicate that the top 2 km beneath the Yanqing-Huailai area has a low shear velocity between 2.0 and 2.5 km/sec. Low velocity layers are identified in upper and mid crustal layers that do not appear in region specific models based on wide angle reflection/refraction analysis. Inversions with a variety of weighting between the receiver functions and phase velocity estimates illustrate the stability of this low velocity layer. Our estimates of a Moho depth of approximately 40 km are consistent with the results from refraction/wide-angle reflection profiles. Predicted receiver functions fit well with the observed for events at all azimuth and distance range with inverted models predicting on average 90% of filtered radial signal power. The calculated phase velocities match the observations. An average velocity model beneath the Basin is obtained from the joint inversion using all receiver functions and dispersion curves at the 7 stations. The predicted first arrival times of P and S wave from this average model when compared with results from the refraction/wide-angle reflection and global AK135F model are delayed by 1-3.5 sec at regional distances. The shear wave velocities of the average model are consistent with the two other models from 10 to 20 km and give more details for the shallow basin and the mid to lower crust (low velocity zone). The low velocity zone is consistent with recent extension, geothermal activity, and earthquake locations above this depth.

ACKNOWLEDGMENTS

The authors would like to thank Chris Hayward, Mary Templeton, Xiang-Wei Yu, Xiang-Tong Xu and Shi-Yu Bai for their help with network installation and data collection. A large portion of the success of this experiment is due to the outstanding help and support of the seismological bureaus and seismic station operators in this region. We thank Arthur Rodgers and one anonymous reviewer, and the associate editor Anton Dainty for numerous comments and suggestions that have improved the manuscript. George Randall's comments on the manuscript are also acknowledged. Zhou is grateful to Guochun Zhao for providing schematic tectonic map as Figure 1a. All topographic maps and Figure 2 were produced using the Generic Mapping Tools (GMT) software of Wessel and Smith (1998). This work was supported by the Air Force Research Laboratory Contracts DTRA01-02-C-0003 and FA8717005-C-0020. Z. -X. Y. and Y.- T. C. acknowledge the supports of NSFC (National Natural Science Foundation of China, No. 40574025) and MOST (Ministry of Science and Technology, No. 2001CB711005) of China. IRIS PASSCAL Instrument Center provided the STS-2 seismometers, Quanterra Q-330 and Baler systems.

REFERENCES

Ammon, C. J., G. E. Randall, and G. Zandt (1990). On the nonuniqueness of receiver functions, *J. Geophys. Res.* **95,** 15303-15318.

Ammon, C. J. (1991). The isolation of receiver effects from teleseismic P waveforms, *Bull. Seism. Soc. Am.* **81,** 2504-2510.

Beaty, K. S, D. R. Schmitt, and M. Sacchi (2002). Simulated annealing inversion of multimode Rayleigh wave dispersion curves for geological structure, *Geophys. J. Int.* **151,** 622-631.

Cassidy, J. F. (1992). Numerical experiments in broadband receiver function analysis, *Bull. Seism. Soc. Am.* **82,** 1453-1474.

Che, Y.-T., J.-H. Wang, J.-Z. Yu and W.-Z. Liu (2001). Character of thermal fluids in upper crust and relationship with seismicity in Yanqing-Huailai, Seismology and geology **23,** 49-54.

Chen, Y.-T., X.-T. Xu, X.-W. Yu and P.-D. Wang (1998). Observations and interpretation of seismic ground motion and earthquake hazard mitigation in Beijing area, *South China Journal of Seismology* **18,** 2-8 (in Chinese).

Chen, X. –Z., X.-T. Xu, and W.-J. Zhai (2005). Variation of stress during the rupture process of the 1995 M_L=4.1 Shacheng, Hebei, China, earthquake sequence, *ACTA Seismologica Sinica* **18,** 297-302.

Dziewonski, A., S. Bloch, and M. Landisman (1969). A technique for the analysis of transient seismic signals, *Bull. Seism. Soc. Am.* **59,** 427-444.

Du, Z. –J. and G. R. Foulger (1999). The crustal structure beneath the northwest fjords, Iceland, from receiver functions and surface waves, *Geophys. J. Int.* **139,** 419-432.

Fnais, M. S. (2004). The crustal and upper mantle shear velocity structure of eastern North America from the joint inversion of receiver function and surface-wave dispersion, *Ph.D. Dissertation*, Saint Louis University, pp228.

Herrin, E., and T. Goforth (1977). Phase-matched filters: application to the study of Rayleigh waves, *Bull. Seism. Soc. Am.* **67,** 1259-1275.

Herrmann, R. B., C. J. Ammon, and J. Julia (2000). Joint inversion of receiver functions and surface-wave dispersion for crustal structure, *Proceeding of the 22nd Annual DoD/DOE Seismic Research Symposium: Planning for verification of and compliance with the Comprehensive Nuclear-Test-Ban Treaty (CTBT)*, September 13-15, New Orleans, LA, 43-53.

Herrmann, R. B., C. J. Ammon, and J. Julia (2001). Application of joint receiver-function surface-wave dispersion for local structure in Eurasia, *Proceeding of the 23rd Seismic Research Review: Worldwide Monitoring of Nuclear Explosions*, October, 2001, LA-UR-01-4454, Los Alamos National Laboratory, Los Alamos, NM, 46-54.

Herrmann, R. B. and C. J. Ammon (2002). *Computer Programs in Seismology: Surface Waves, Receiver Functions and Crustal Structure*, Version 3.15.

Julia, J., C. J. Ammon, R. B. Herrmann, and A. M. Correig (2000). Joint inversion of receiver function and surface wave dispersion observations, *Geophys. J. Int.* 143, 99-112.

Julia, J., C. J. Ammon, and R. B. Herrmann (2003). Lithospheric structure of the Arabian Shield from the joint inversion of receiver functions and surface-wave group velocities, *Tectonophysics* **37,** 1-21.

Kennett, B. L. N., E. R. Engdahl, and R. Buland R. (1995). Constraints on seismic velocities in the earth from travel times, *Geophys. J. Int* **122,** 108-124.

Kiknchi, M., and H. Kanamori (1982). Inversion of complex body waves, *Bull. Seism. Soc. Am.* **72,** 491-506.

Langston, A. C. (1977). The effect of planar dipping structure on source and receiver responses for constant ray parameter, *Bull. Seism. Soc. Am.* **67,** 1029-1050.

Langston, A. C. (1979). Structure under Mount Rainier, Washington, inferred from teleseismic body waves, *J. Geophys. Res.* 84, 4749-4762.

Li, A., and R. S. Detrick (2006). Seismic structure of Iceland from Rayleigh wave inversions and geodynamic implications, *Earth Planet. Sci. Lett.* **241,** 901-912.

Ligorría, J. P., and C. J. Ammon (1999). Iterative deconvolution and receiver function estimation, *Bull. Seism. Soc. Am.* **89,** 1395–1400.

Lin, G.,Y.-H. Wang, F. Guo, Y.-J. Wang and W.-M. Fan (2004). Geodynamic modeling of crustal deformation of the North China block: a preliminary study, J. Geophys. Eng. **1,** 63-69, doi:10.1088/1742-2132/1/1/008.

Liu, C.-Q., S.-X. Jia, M.-J. Liu, and C.-F. Li (1997). Analysis and study of the large earthquake risk in Yanqing-Huailai Basin, *ACTA Seismologica Sinica*, **10,** 639-647.

McMechan, G. A., and M. J. Yedlin (1981). Analysis of dispersive waves by wave field transformation, *Geophysics* **46,** 869-874.

Montagner, J. P. and B. L. N. Kennett (1995). How to reconcile body-wave and normal-mode reference Earth models? *Geophys. J. Int.* **125,** 229-248.

Owens, J. T., G. Zandt and S. R. Taylor (1984). Seismic evidence for an ancient rift beneath the Cumberland Plateau, Tennessee: A detailed analysis of broadband teleseismic P waveforms, *J. Geophys. Res.* **89,** 7783-7795.

Özalaybey, S., M. K. Savage, A. F. Sheehan, J. N. Louie and J. N Brune (1997). Shear-wave velocity structure in the Northern Basin and Range Province from the combined analysis of receiver functions and surface waves, *Bull. Seism. Soc. Am.* 87, 183-199.

Pavlides, B. S., N. C. Zouros, Z.-J. Fang, S.-P. Cheng, M. D. Tranos and A. A. Chatzipetros (1999). Geometry, kinematics and morphotectonics of the Yanqing-Huailai active faults (northern China), *Tectonophysics* **308,** 99-118.

Rowley, D. B., F. Xue, R. D. Tucker, Z. X. Peng, J. Baker, and A. Davis (1997), Ages of Ultrahigh Pressure Metamorphism and Protolith Orthogneisses from the Eastern Dabie Shan: U/Pb Zircon Geochronology, *Earth Planet. Sci. Lett.* **151,** 191-203.

Sun, Wu-Cheng, Song-Lin, Li, Li-Lei, Luo and Hua-Fong Yue (1987). A preliminary study on low velocity layer in the crust in North China, *Seismol. and Geol.* **9(1)**, 17-26.

Wessel, P., and W. H. F. Smith (1998), New, improved version of the Generic Mapping Tools Released, *EOS Trans. AGU,* **79,** 579.

Wu, Z.-R., B.-Y. Yuan, J.-Z. Sun, and Z.-S. Liu (1979). Neotectonics and seismicity of Yan-Huai basin in Hebei Province. *Seismol. Geol.* **1(2)**, 46-56.

Xu, Y.-G., J.-L. Ma, F A. Frey, M D. Feigenson, and J.-F. Liu (2005). Role of lithosphere-asthenosphere interaction in the genesis of Quaternary alkali and tholeiitic basalts from Datong, western North China Craton, *Chem. Geol.* **224,** 247-271.

Xu, X.-T., Y.-T. Chen and P.-D. Wang (1997). The tectonic stresses in the Huailai basin, *Seismological and Geomagnetic Observation and Research* **18,** 1-8 (in Chinese with English abstract).

Xu, X.-T., Y.-T. Chen and P.-D. Wang (1999). Rupture process of the M_L=4.1 earthquake in Huailai basin on July 20, *Acta Seismologica Sinica* **12**, 618-631.

Xu, X.-T., Y.-T. Chen and P.-D. Wang (2001). Precise determination of focal parameters for July 20, 1995 M_L=4.1 earthquake sequence in the Huailai basin, *Acta Seismologica Sinica* **14,** 237-250.

Yoo, H. J., R. B. Herrmann, K. H. Cho, and K. Lee (2007). Imaging the three-dimension crust of the Korean Peninsula by joint inversion of surface-wave dispersion and teleseismic receiver functions, *Bull. Seismo. Soc. Am.* **97,** 1002-1011, doi:10.1785/0120060134.

Zhang, X.-K., C.-Y. Wang, G.-D. Liu, J.-L. Song, L.-L. Luo, T. Wu and J.-C. Wu (1996). Fine crustal structure in Yanqing-Huailai region by deep seismic reflection profiling, *Chinese J Geophys* **39,** 356~364 (in Chinese with English abstract).

Zhao, G.-C., S. A. Wilde, P. A. Cawood, and L.-Z. Lu (1999). Thermal evolution of two textural types of mafic granulites in the North China craton: evidence for both mantle plume and collisional tectonics, *Geol. Mag.* **136,** 223-240.

Zhao, G.-C., S. A. Wilder, P. A. Cawood and M. Sun (2002). Shrimp U-Pb Zircon ages of the Fuping Complex: implications for late archean to paleoprotezozoic accretion and assembly of the North China Craton, *Am. J. Sci.* **302,** 191-226.

Zhao, J.-R., X.-K. Zhang, C.-K. Zhang, J.-S. Zhang, B.-F. Liu, Q.-F. Ren, S.-Z. Pan and Y. Hai (2005). The heterogeneous characteristics of crust-mantle structures and the seismic activities in the northwest Beijing region, *ACTA Seismologica Sinica* **18,** 125-134.

Zheng, T.-Y., L. Zhao and L. Chen (2005). A detailed receiver function image of the sedimentary structure in the Bohai Bay Basin, *Phys. Earth Planet. Int.* **152,** 129-143.

Zhou, R.-M., B. W. Stump, Y.-T. Chen, C. T. Hayward, Z.-X. Yang, M. Templeton, X.-W. Yu, S.-Y. Bai and X.-T. Xu (2003a). Network installation in the Yanqing-Huailai Basin and preliminary study of natural and man-induced events. *Proceedings of the 25th Seismic Research Review — Nuclear Explosion Monitoring: Building the Knowledge Base*, September 2003, LA-UR-03-6029, Los Alamos National Laboratory, Los Alamos, NM, 504-513.

Zhou, R.-M., B. W. Stump, and Y.-T. Chen (2003b). A comparative study of intermediate-period surface waves from kiloton-size mining explosions in Northeast China and Western United States. *Eos Trans.* AGU, **84(46)**, Fall Meet. Suppl., Abstract S32B-0848.

Zhou, R.-M., B. W. Stump, and C. T. Hayward (2006). *M*s:*m*b discrimination study of mining explosions in Wyoming, USA and in Qianan, China, *Bull. Seism. Soc. Am.* **96 (5)**, 1742-1752, doi:10.1785/0120050178.

Zhou, Y.-S. and C.-R. He (2002). The relationship between low velocity layers and rheology of the crust in North China and its effect on strong earthquake, *Seismol. and Geol.* **24(1),** 125-131.

Zhu, Z.-P., X.-K. Zhang, J.-S. Zhang, C.-K. Zhang, J.-R. Zhao and Y.-J. Gai (1997). Study on crust-mantle tectonics and its velocity structure along the Beijing-Huailai-Fengzhen profile, *Acta Seismologica Sinica* **10,** 615~623.

List of Tables:

Table 1. The Geographical Distribution of the Broadband Seismic Stations

Station Name	**Station Code**	**Latitude (^{o}N)**	**Longitude (^{o}E)**	**Elevation (m)**
AnYingPu	AYPU	40.4936	115.5168	815
BaKou	BAKOU	40.4650	115.4025	741
ChenJiaPu	CJPU	40.3019	115.9233	674.9
MaJiaPu	MJPU	40.6667	115.6837	1075
XuJiaYao	XJYAO	40.2679	115.2133	789
YouFang	YFANG	40.7544	115.3188	1109
ZhaiShanPo	ZSPO	40.5278	114.9500	865

Table 2. List of Event Parameters

Event Code	Date (Y-M-D)	Time (hhmmss.mm)	Latitude (°N)	Longitude (°E)	Magnitude	Depth (km)	Distance to AYPU (degree)	AYPU Back-Azimuth (degree)
2003076	2003-03-17	163617.31	51.27	177.98	7.1	33	43.4	53.8
2003089	2003-03-30	181334.09	-3.17	127.54	6.2	33	45.0	162.9
2003141	2003-05-21	184420.10	36.96	3.63	6.9	12	80.6	311.3
2003166	2003-06-15	192433.15	51.55	176.92	6.5	20	42.7	53.6
2003174	2003-06-23	121234.47	51.44	176.78	7.0	20	42.6	53.8
2003339	2003-12-05	212609.48	55.54	165.78	6.7	10	35.9	48.0
2003360	2003-12-26	015652.44	29.00	58.31	6.8	10	47.5	274.7
2004039	2004-02-08	085851.80	-3.66	135.34	6.9	25	47.7	152.8
2004107	2004-04-16	215705.41	-5.21	102.72	6.0	44	47.2	197.5
2004114	2004-04-23	015030.22	-9.36	122.84	6.7	65	50.3	170.6
2004162	2004-06-10	151957.75	55.68	160.00	6.9	188	32.6	47.1
2004180	2004-06-28	094947.00	54.80	-134.25	6.8	20	67.7	35.8
2004316	2004-11-11	212641.15	-8.15	124.87	7.5	10	49.4	167.8
2004353	2004-12-18	064619.87	48.84	156.31	6.2	11	29.8	59.9
2005022	2005-01-22	203017.35	-7.73	159.48	6.5	29	62.9	129.4
2005023	2005-01-23	201012.15	-1.20	119.93	6.3	11	41.9	173.4
2005036	2005-02-05	033425.73	16.01	145.87	6.6	142	35.9	124.1
2005036-2	2005-02-05	122318.94	5.29	123.34	7.1	525	35.9	166.6
2005046	2005-02-15	144225.85	4.76	126.42	6.6	39	37.1	161.8
2005050	2005-02-19	000443.59	-5.56	122.13	6.5	10	46.5	170.9
2005061	2005-03-02	104212.23	-6.53	129.93	7.1	201	48.9	160.8
2005089	2005-03-30	161941.10	2.99	95.41	6.4	22	41.7	211.1
2005093	2005-04-03	005921.42	0.37	98.32	6.0	30	43.1	205.7
2005093-2	2005-04-03	031056.47	2.02	97.94	6.3	36	41.6	207.0
2005099	2005-04-09	151627.89	56.17	-154.52	6.0	14	57.3	41.4
2005100	2005-04-10	102911.28	-1.64	99.61	6.7	19	44.6	203.0
2005100-2	2005-04-10	172439.40	-1.59	99.72	6.4	30	44.5	202.9
2005106	2005-04-16	163803.90	1.81	97.66	6.4	31	41.9	207.3

2005118	2005-04-28	140733.70	2.13	96.80	6.3	22	41.9	208.7
2005130	2005-05-10	010905.10	-6.23	103.14	6.4	17	48.1	196.6
2005134	2005-05-14	050518.48	0.59	98.46	6.8	34	42.8	205.6
2005139	2005-05-19	015452.85	1.99	97.04	6.9	30	42.0	208.3
2005165	2005-06-14	171016.64	51.23	179.41	6.8	51	44.3	53.6
2005186	2005-07-05	015202.95	1.82	97.08	6.8	21	42.1	208.1

Figure Captions

Figure 1.

(a) Schematic tectonic map of China showing the major Precambrian blocks and Late Neoproterozoic and Paleozoic fold belts (courtesy of Prof. Guochun Zhao at the University of Hong Kong), and the NNE-SSW extended thick line indicating the Tan-Lu fault zone (modified from Xu *et al.*, 2005).

(b) Map of SMU-IGPCEA Huailai Seismic Network and seismicity (open circles) for the time period of January 01, 2002 through December 31, 2006 from the Capital Circle Seismic Network (http://www.csndmc.ac.cn/newweb/data.htm#). Black solid circles are locations of earthquakes with magnitude greater than 6 from 231B.C. to December 31, 2001. White dotted rectangle is the Yanqing-Huailai Basin and adjacent area (Figure 1c) and red solid rectangle denotes the source location of the 1.3-kiloton mining explosion in 2002.

(c) Topographic map of Yanqing-Huailai Basin (black dotted line) and adjacent area. Broadband seismic stations of the SMU-IGPCEA Huailai Seismic Network are designated as stars. The white line is the Beijing-Huailai-Fengzhen (H20) refraction/ wide angle reflection profile (Zhu *et al.*, 1997). Open circles are locations of two historical earthquakes in 1337 and 1720. Solid circle is the epicenter of a M_L 4.1 earthquake on July 20, 1995. Solid dots are towns in the area.

Figure 2. Map (azimuth equidistant projection centered at AYPU) of events (plus). Circles are 30, 60, and 90 great circle distances range from AYPU (dot).

Figure 3. (Left) Three-component seismograms at six stations from event 2003089 used for receiver function calculation. (Right) Receiver functions from event 2003089 with Gaussian window parameter, α of 1.0.

Figure 4. Plot of receiver functions (Gaussian window parameter $\alpha = 1.0$) versus back-azimuth for all events recorded at station AYPU (27 events) and XJYAO (27 events).

Figure 5. Fundamental Rayleigh waves (10-100s) extracted from vertical component seismograms using Multiple Filter Analysis and Phase Matched Filter for event 2003089.

Figure 6. Comparison of measured teleseismic phase velocities (thin gray) with the prediction (thick dark) based on the model determined by the joint inversion. The measured data are plot with ±1 standard deviation.

Figure 7. Comparison of models resulting from inversions with different *p* values that control the weighting of the receiver functions and surface wave phase velocities at AYPU.

Figure 8. (a) Plot of the shear wave velocity starting model (gray) and the final model (black) at AYPU. The AK135F model is plotted as a dash line; (b) Comparison between observed (black solid line) and predicted receiver functions (gray dashed line) after inversion. The receiver functions are labeled with the year/month/day (day of year) to the upper right of each trace, and with the station name, Gaussian filter parameter, the percentage of fit, and the ray parameter (sec/km) to the left of each trace.

Figure 9. Map of stations and shear-wave velocity models from joint inversions at each of the 7 stations (black) compared to the averaged model inverted using all 7 stations (gray) simultaneously. The number after each station is the number of events used for station specific inversion.

Figure 10. (a) Raw vertical component seismograms (thin gray) and fundamental mode Rayleigh waves (thick dark) from the 1.3 kiloton mining explosion.

(b) Comparison of measured regional group velocities (thin gray) with a prediction (thick dark) based on the velocity model from the joint inversion. The measured data are plot with ± 1 standard deviation.

Figure 11. Left: Comparison of the model from the joint inversion using receiver function, phase velocities and with (dashed) and without (solid) group velocities from the mining events observed at AYPU.

Right: Comparison of average models from the joint inversions for this region using receiver functions, phase velocities and with (dashed) and without (solid) group velocities from the mining events.

Figure 12. Left: Comparison between the model resulting from the joint inversion (receiver functions and phase velocities) using all station data (solid black) and the model from a refraction/wide-angle reflection survey (gray), and AK135F model (dotted). Right: Predicted first arrival times of P (upper) and S (lower) from the three different models.

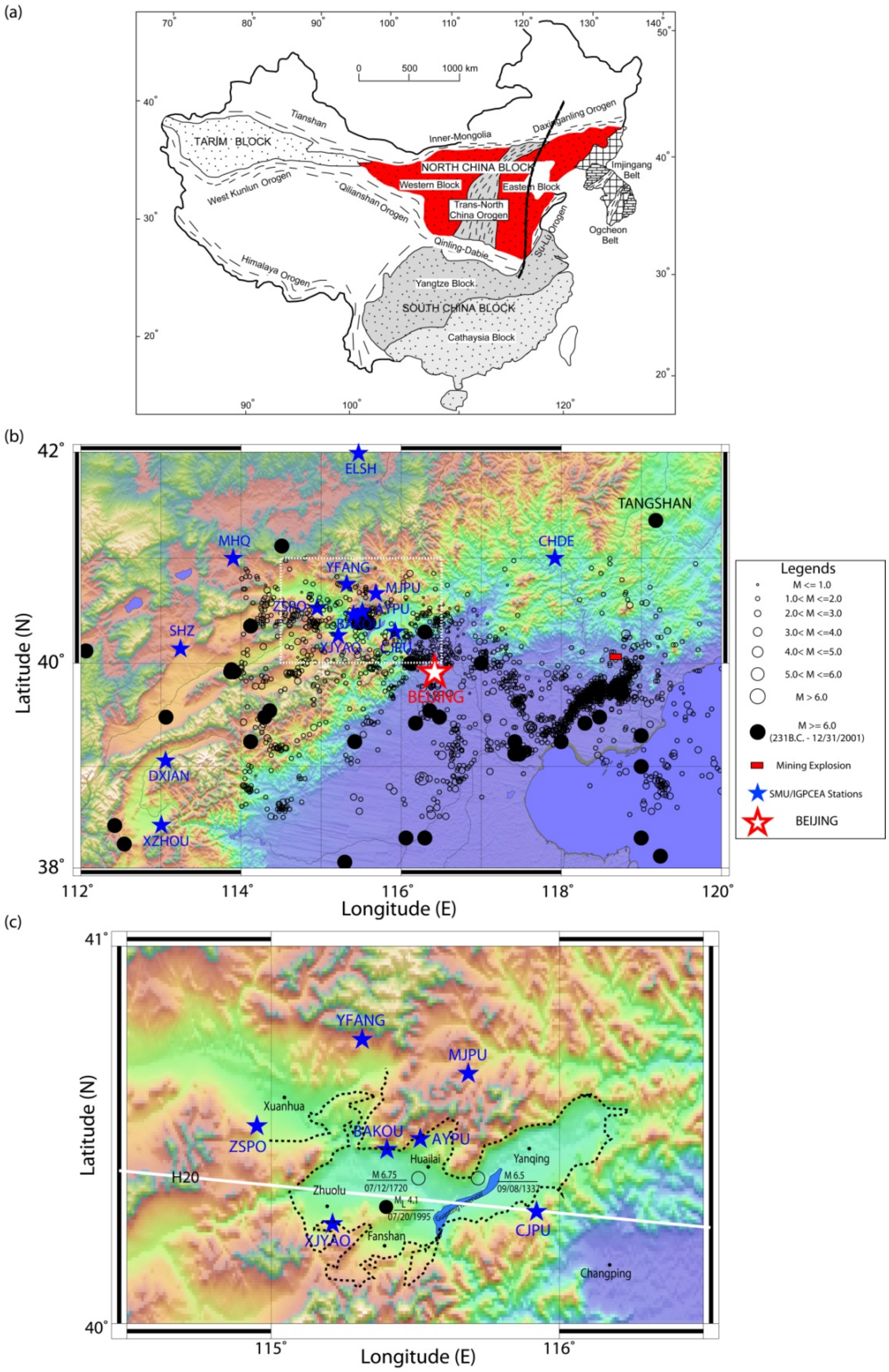
(a)
0
500
1000 km
TARIM BLOCK
Tianshan
Inner-Mongolia
Daxinganling Orogen
NORTH CHINA BLOCK
Western Block
Eastern Block
Trans-North China Orogen
Imjingang Belt
Ogcheon Belt
West Kunlun Orogen
Qilianshan Orogen
Qinling-Dabie
Su-Lu Orogen
Himalaya Orogen
Yangtze Block
SOUTH CHINA BLOCK
Cathaysia Block
(b)
ELSH
TANGSHAN
MHQ
CHDE
YFANG
MJPU
ZSPO
AYPU
BAKOU
SHZ
XJYAO
CJPU
BEIJING
DXIAN
XZHOU
Latitude (N)
Longitude (E)
Legends
M <= 1.0
1.0< M <=2.0
2.0< M <=3.0
3.0< M <=4.0
4.0< M <=5.0
5.0< M <=6.0
M > 6.0
M >= 6.0 (231B.C. - 12/31/2001)
Mining Explosion
SMU/IGPCEA Stations
BEIJING
(c)
YFANG
MJPU
Xuanhua
ZSPO
BAKOU
AYPU
Huailai
Yanqing
H20
M 6.75 07/12/1720
M 6.5 09/08/1337
Zhuolu
M_L 4.1 07/20/1995
XJYAO
CJPU
Fanshan
Changping
Latitude (N)
Longitude (E)

Figure 1.

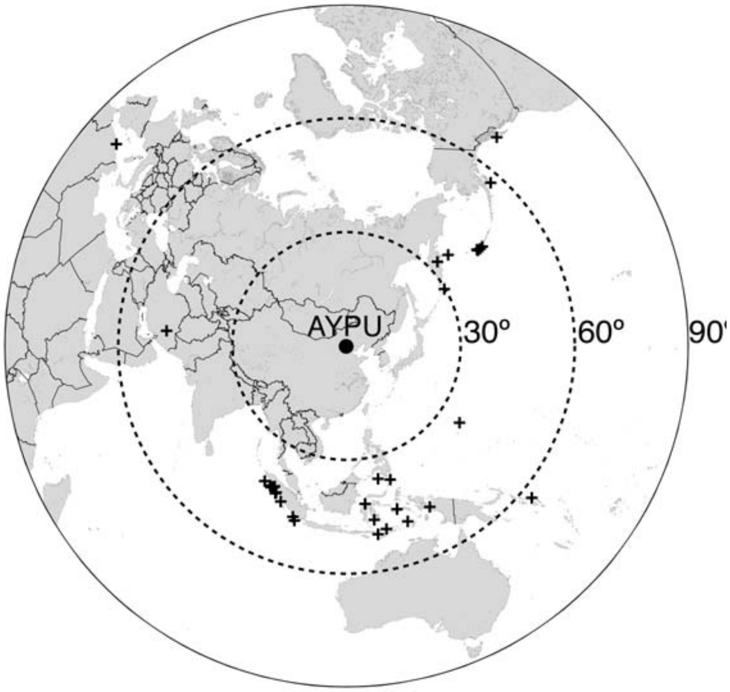

Figure 2.

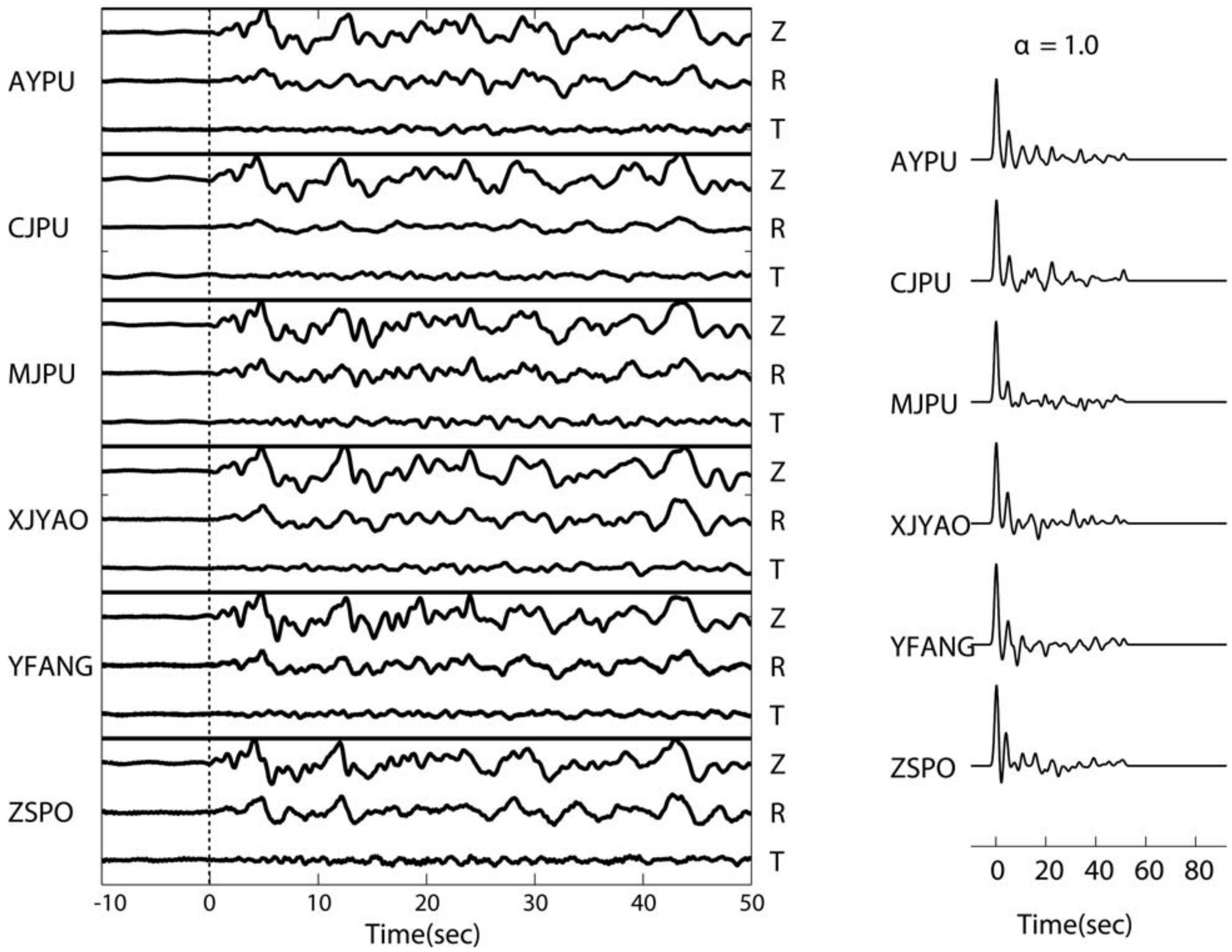
AYPU
CJPU
MJPU
XJYAO
YFANG
ZSPO
Z
R
T
-10
0
10
20
30
40
50
Time(sec)
α = 1.0
AYPU
CJPU
MJPU
XJYAO
YFANG
ZSPO
0
20
40
60
80
Time(sec)

Figure 3.

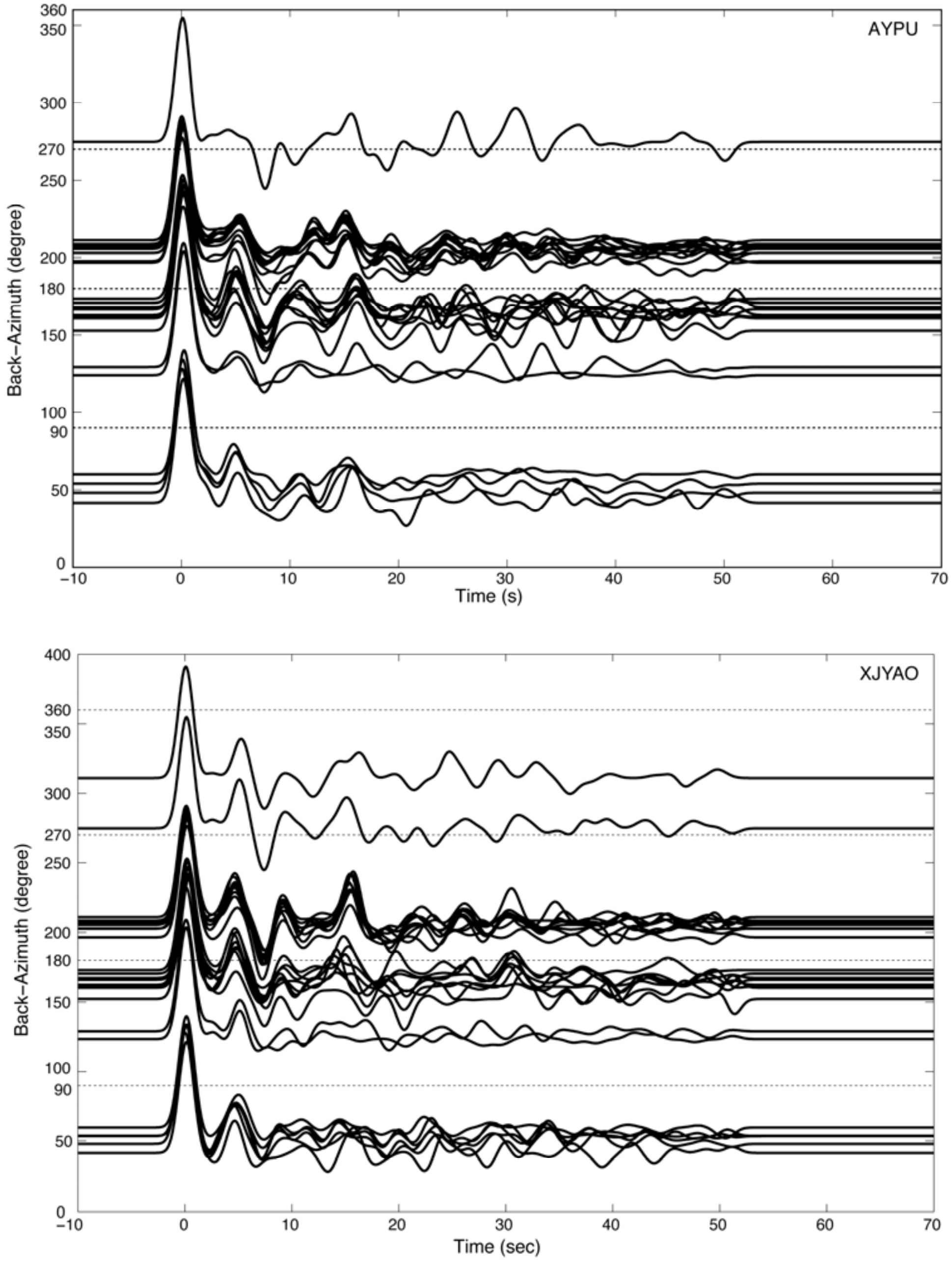
AYPU
Back−Azimuth (degree)
360
350
300
270
250
200
180
150
100
90
50
0
−10
0
10
20
30
40
50
60
70
Time (s)
XJYAO
Back−Azimuth (degree)
400
360
350
300
270
250
200
180
150
100
90
50
0
−10
0
10
20
30
40
50
60
70
Time (sec)

Figure 4.

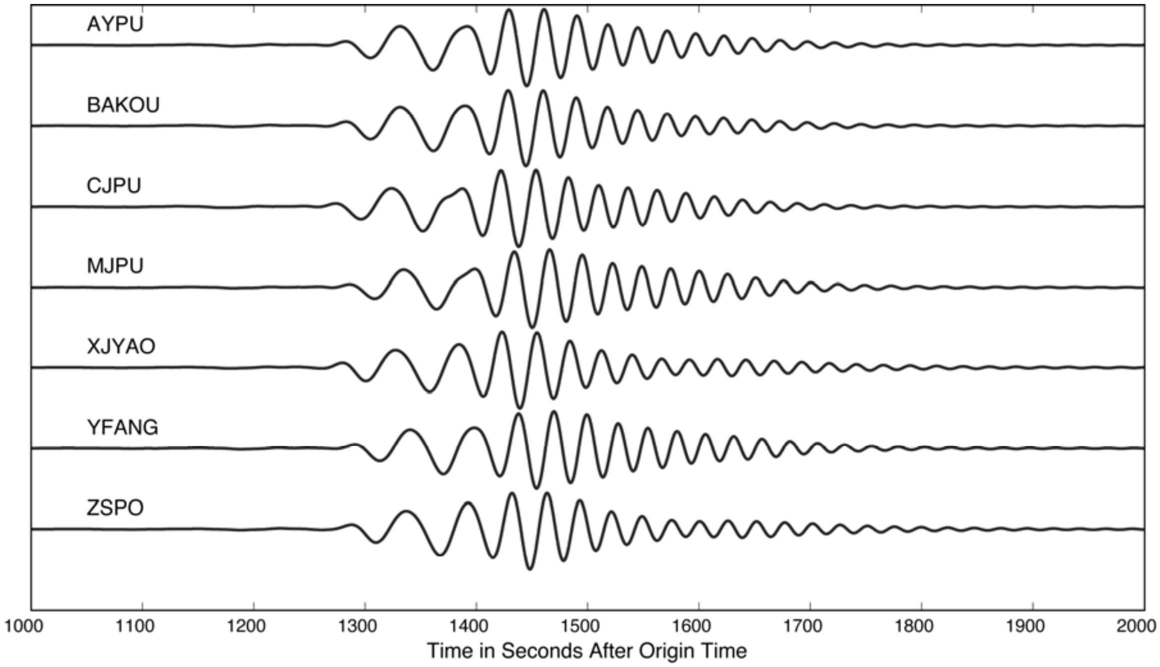
AYPU
BAKOU
CJPU
MJPU
XJYAO
YFANG
ZSPO
1000
1100
1200
1300
1400
1500
1600
1700
1800
1900
2000
Time in Seconds After Origin Time

Figure 5.

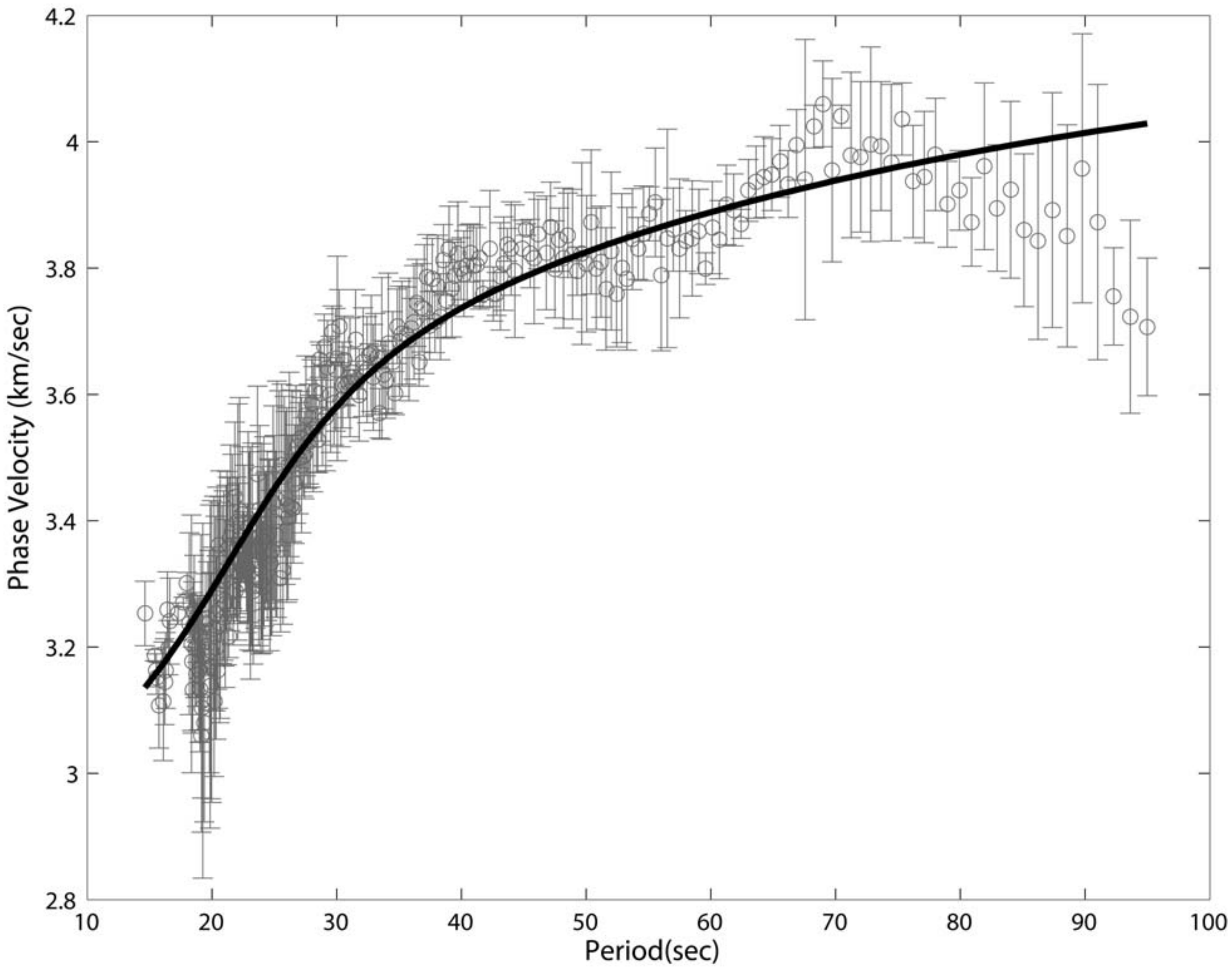
4.2
4
3.8
3.6
3.4
3.2
3
2.8
10
20
30
40
50
60
70
80
90
100
Phase Velocity (km/sec)
Period(sec)

Figure 6.

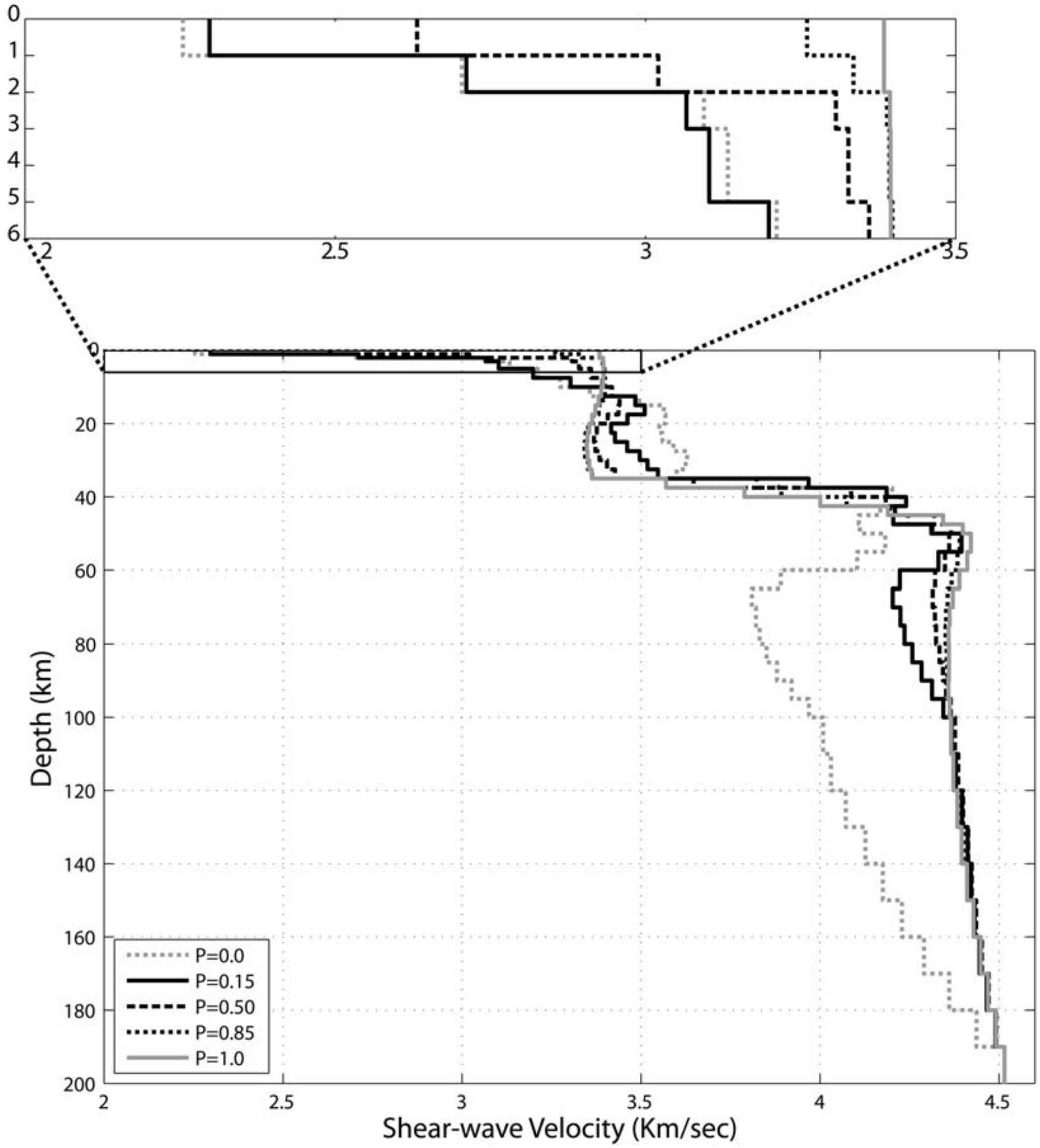
0
1
2
3
4
5
6
2
2.5
3
3.5
Depth (km)
0
20
40
60
80
100
120
140
160
180
200
2
2.5
3
3.5
4
4.5
Shear-wave Velocity (Km/sec)
P=0.0
P=0.15
P=0.50
P=0.85
P=1.0

Figure 7.

8(a)

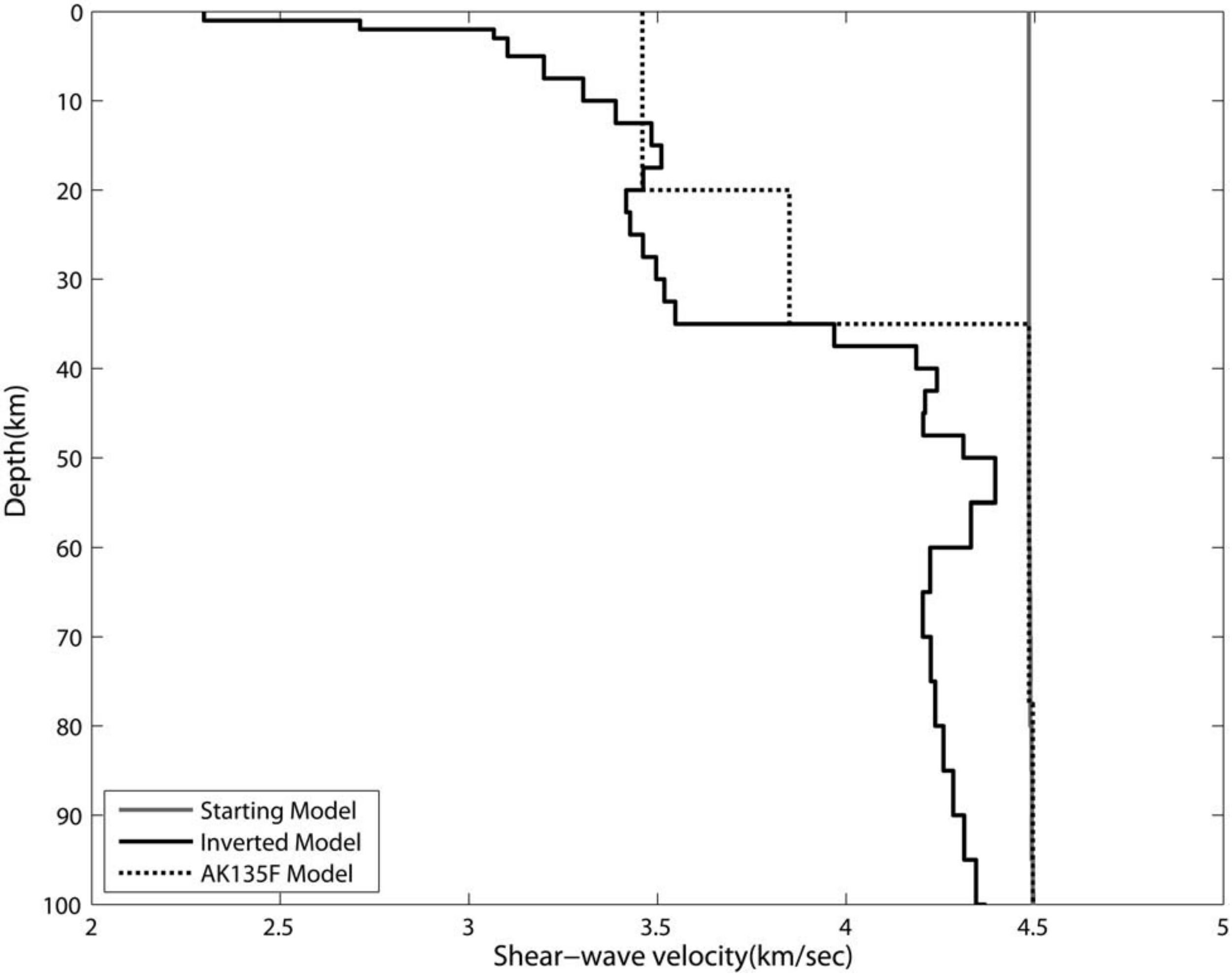

Depth(km)
0
10
20
30
40
50
60
70
80
90
100
2
2.5
3
3.5
4
4.5
5
Shear−wave velocity(km/sec)
Starting Model
Inverted Model
AK135F Model

8(b)

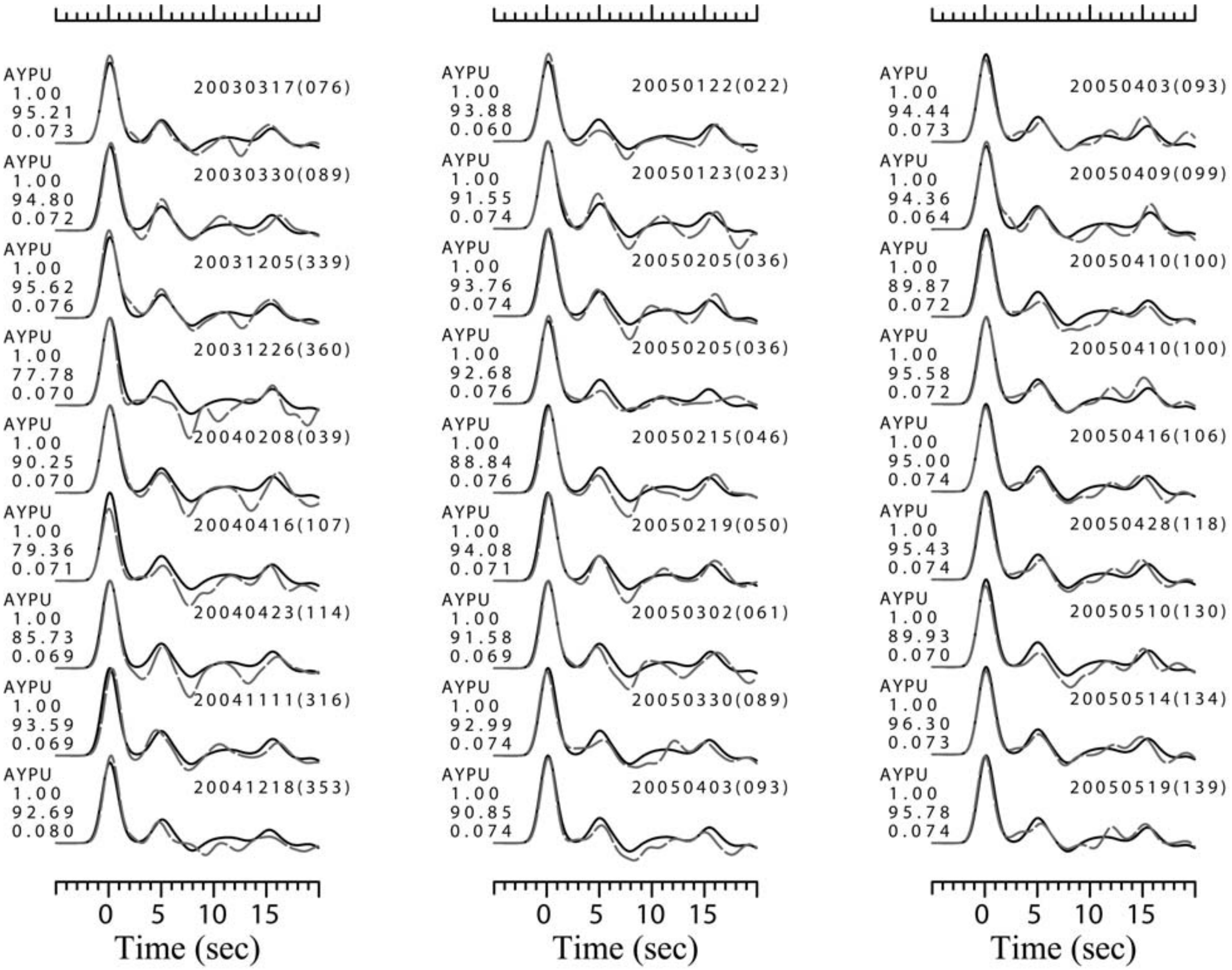

AYPU
1.00
95.21
0.073
20030317(076)
AYPU
1.00
94.80
0.072
20030330(089)
AYPU
1.00
95.62
0.076
20031205(339)
AYPU
1.00
77.78
0.070
20031226(360)
AYPU
1.00
90.25
0.070
20040208(039)
AYPU
1.00
79.36
0.071
20040416(107)
AYPU
1.00
85.73
0.069
20040423(114)
AYPU
1.00
93.59
0.069
20041111(316)
AYPU
1.00
92.69
0.080
20041218(353)
0
5
10
15
Time (sec)
AYPU
1.00
93.88
0.060
20050122(022)
AYPU
1.00
91.55
0.074
20050123(023)
AYPU
1.00
93.76
0.074
20050205(036)
AYPU
1.00
92.68
0.076
20050205(036)
AYPU
1.00
88.84
0.076
20050215(046)
AYPU
1.00
94.08
0.071
20050219(050)
AYPU
1.00
91.58
0.069
20050302(061)
AYPU
1.00
92.99
0.074
20050330(089)
AYPU
1.00
90.85
0.074
20050403(093)
0
5
10
15
Time (sec)
AYPU
1.00
94.44
0.073
20050403(093)
AYPU
1.00
94.36
0.064
20050409(099)
AYPU
1.00
89.87
0.072
20050410(100)
AYPU
1.00
95.58
0.072
20050410(100)
AYPU
1.00
95.00
0.074
20050416(106)
AYPU
1.00
95.43
0.074
20050428(118)
AYPU
1.00
89.93
0.070
20050510(130)
AYPU
1.00
96.30
0.073
20050514(134)
AYPU
1.00
95.78
0.074
20050519(139)
0
5
10
15
Time (sec)

Figure 8.

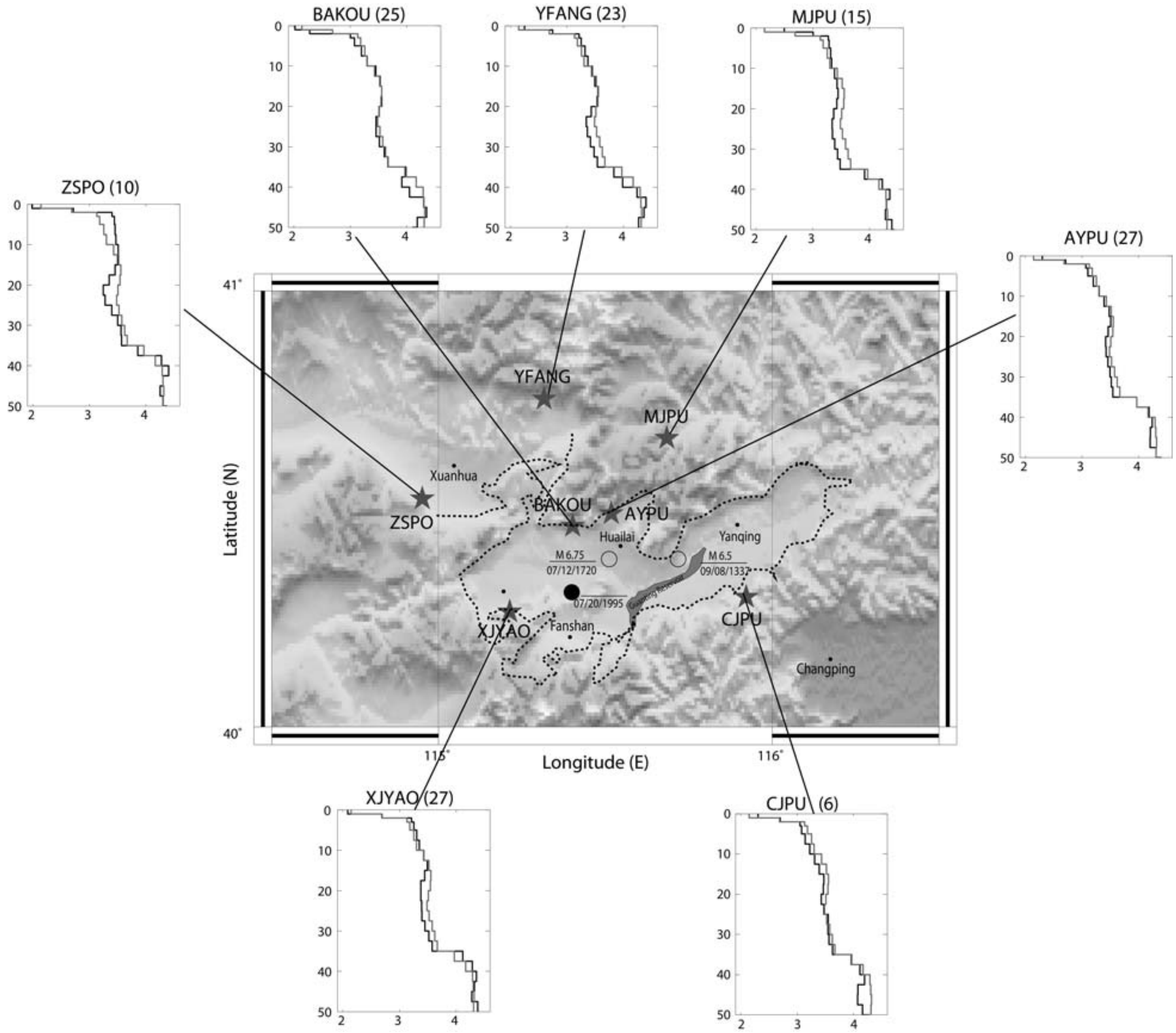
BAKOU (25)
YFANG (23)
MJPU (15)
ZSPO (10)
AYPU (27)
XJYAO (27)
CJPU (6)
0
10
20
30
40
50
2
3
4
41°
40°
115°
116°
Latitude (N)
Longitude (E)
YFANG
MJPU
Xuanhua
ZSPO
BAKOU
AYPU
Huailai
Yanqing
M 6.75
07/12/1720
M 6.5
09/08/1337
07/20/1995
XJYAO
Fanshan
CJPU
Changping

Figure 9.

10(a)

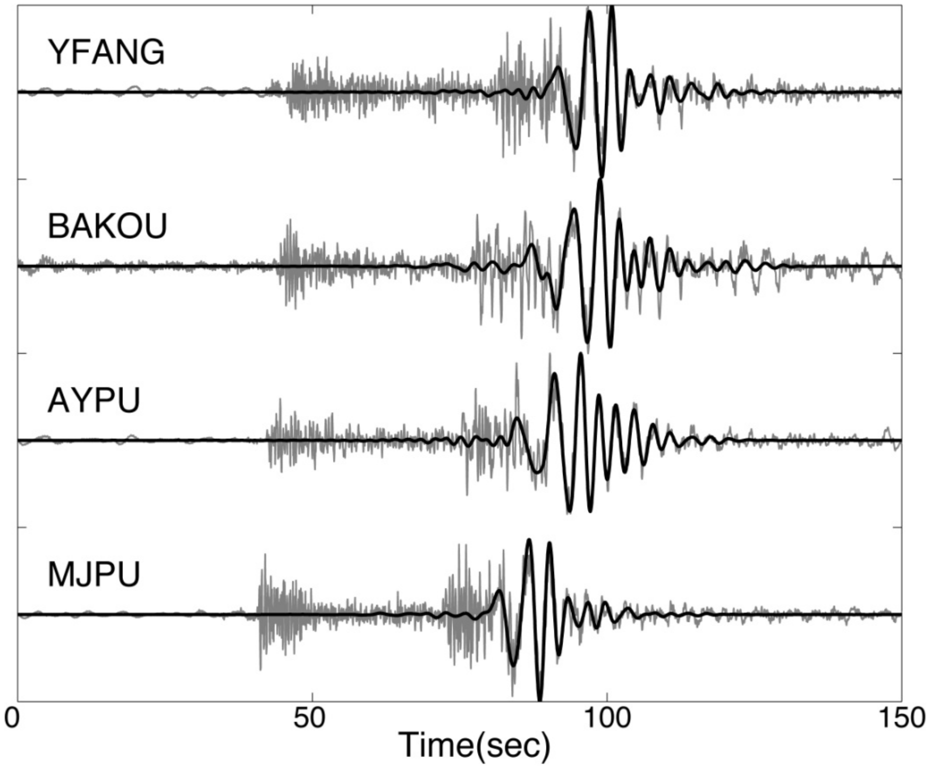

10(b)

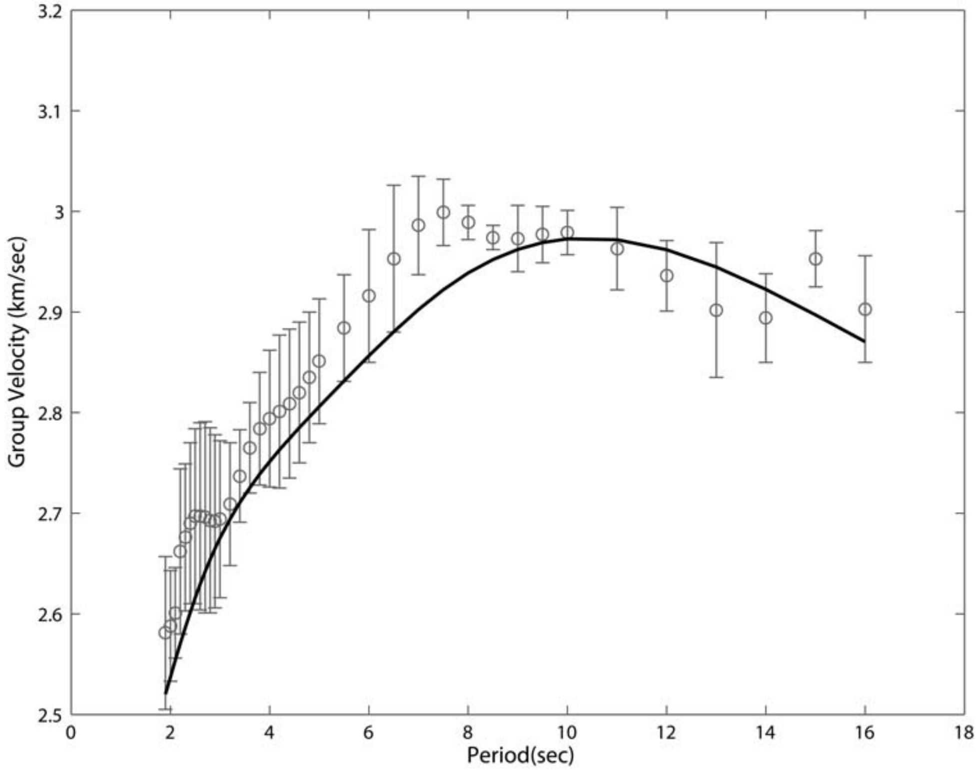

Figure 10.

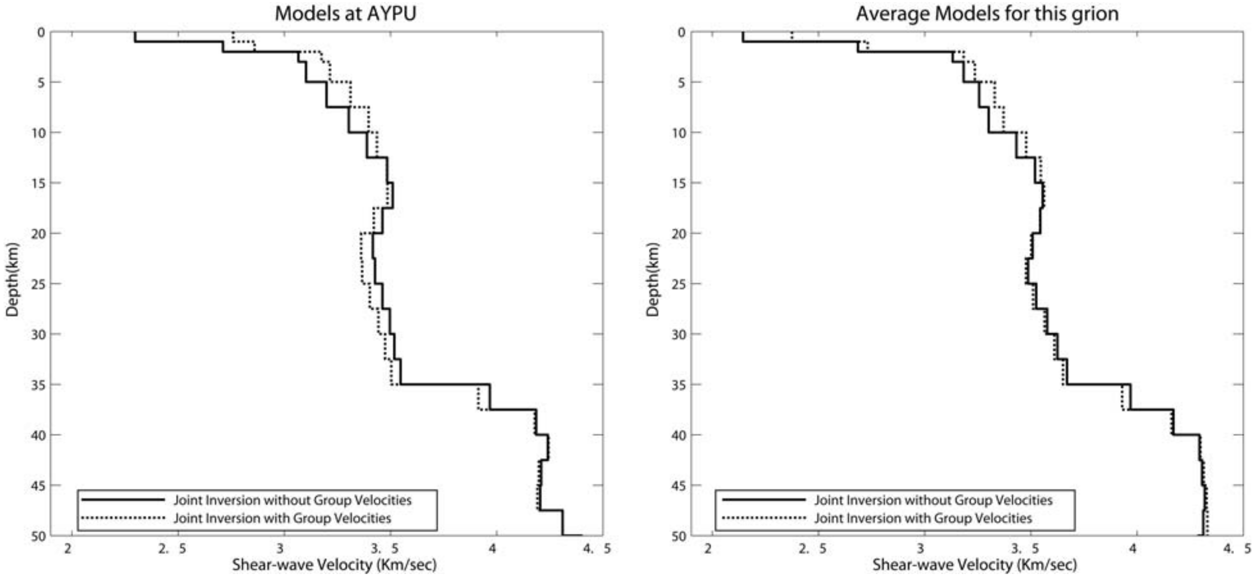
Models at AYPU
Average Models for this grion
Depth(km)
0
5
10
15
20
25
30
35
40
45
50
2
2. 5
3
3. 5
4
4. 5
Shear-wave Velocity (Km/sec)
Joint Inversion without Group Velocities
Joint Inversion with Group Velocities

Figure 11

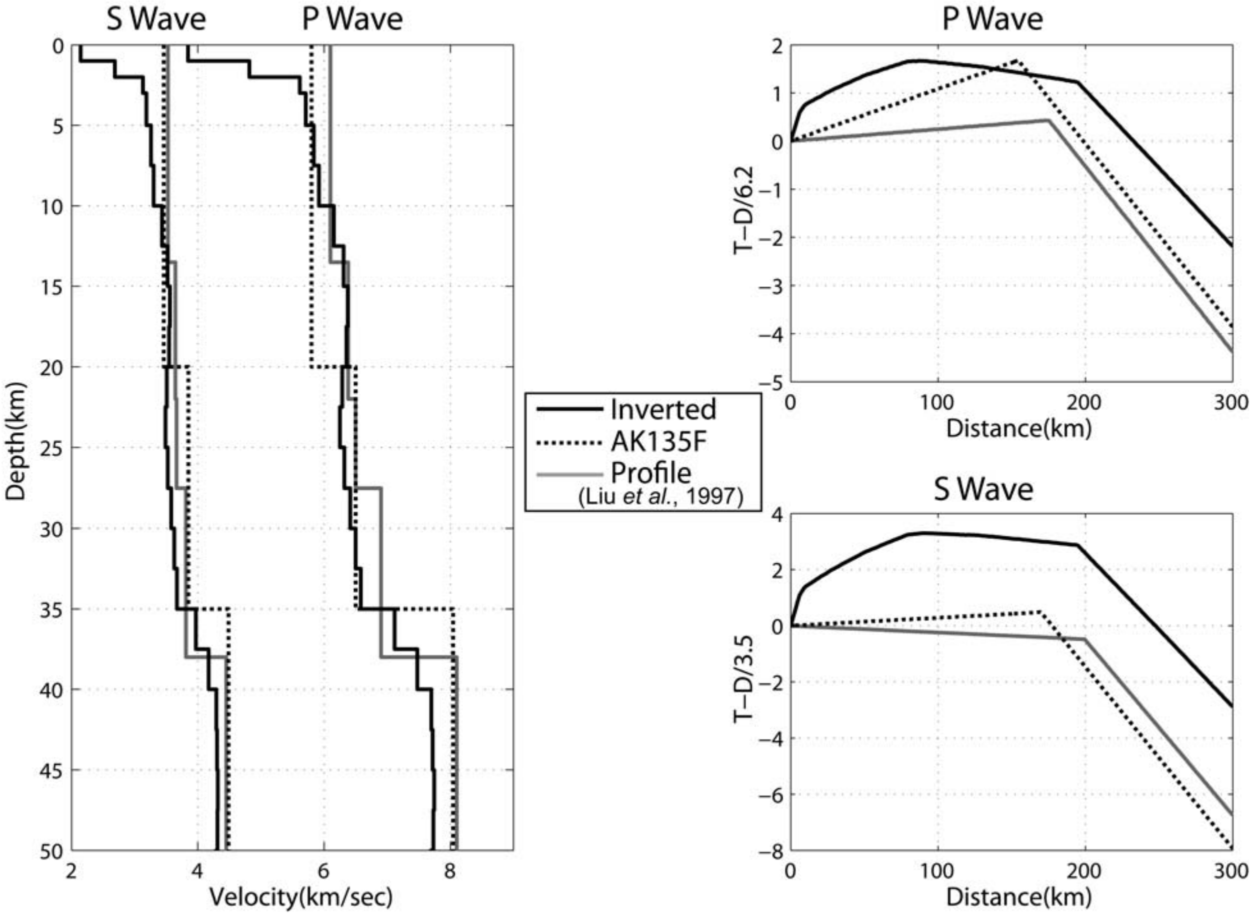
S Wave
P Wave
Depth(km)
0
5
10
15
20
25
30
35
40
45
50
2
4
6
8
Velocity(km/sec)
Inverted
AK135F
Profile
(Liu *et al.*, 1997)
P Wave
T−D/6.2
2
1
0
−1
−2
−3
−4
−5
0
100
200
300
Distance(km)
S Wave
T−D/3.5
4
2
0
−2
−4
−6
−8
0
100
200
300
Distance(km)

Figure 12.

CHAPTER 2

Teleseismic Receiver Function and Surface Wave Study of Velocity Structure in the Haicheng and Xiuyan Area, NE China

Authors: Rong-Mao Zhou(1*), Brian W. Stump (1), Robert B. Herrmann (2)
Zhi-Xian Yang and Yun-Tai Chen(3)

Affiliation and Addresses of Authors:
(1) Roy M. Huffington Department of Earth Sciences
Southern Methodist University
Dallas, TX 75275, USA
(2) Department of Earth & Atmospheric Sciences
Saint Louis University
St. Louis, MO 63103, USA
(3) Institute of Geophysics
China Earthquake Administration
Beijing, P. R. China, 100081
E-mail Addresses:
rongmaozhou@gmail.com (R.-M. Z.), bstump@smu.edu (B. W. S.),
rbh@eas.slu.edu (R. B. H.),
zhixiany@cea-igp.ac.cn (Z.-X. Y.) and chenyt@cea-igp.ac.cn (Y.-T. C.)
Phone: 1-281-409-3607 (R.-M. Z.)
**current address: Microseismic Inc. Houston, TX*

To be submitted **Bulletin of Seismological Society of America**

ABSTRACT

On November 29, 1999, an earthquake of M_S 5.9 occurred in Xiuyan, Liaoning, China. This earthquake was followed by a number of aftershocks. To study the characteristics of this fault system and the structure beneath this area, 10 portable broadband seismometers were deployed around this region beginning August 2004. Instrumentation consisted of STS-2 seismometers connected to Quanterra Q-330 digitizers and Balers located in hard rock vaults. The high-quality data set recorded by these 13 regional stations provides the opportunity to study the detailed velocity structure beneath this region using both teleseismic and regional signals.

Short-period surface wave dispersion curves from ambient noise were obtained using four months of data. Receiver functions and surface wave phase velocities from 95 teleseismic events that occurred between August 2004 and May 2008 have been determined. A joint inversion of these teleseismic receiver functions and surface wave group velocities from ambient noise analysis has been conducted and the shallow crustal shear velocity structure around the Xiuyan area estimated. Crustal thickness beneath the Xiuyan area is about 34 km, which is consistent with the results from other geophysical studies in this region.

STUDY AREA

The 1975 Haicheng Earthquake, the first predicted earthquake in China, occurred in this region and motivated an interest to understand seismicity for hazard reduction. The Haicheng area is also rich in natural resources such as iron, zinc, coal, oil and natural gas. Mining activities related to resource recovery provide additional sources of seismic waves. Historically, a few larger earthquakes in addition to the 1975 event have occurred in the Haicheng-Xiuyan seismogenic zone (Haichenghe-Dayanghe fault) and surrounding area. Three earthquakes with magnitude 5.25, 5.5, and 5.9 occurred near Yinkou on September 19, 1859; April 7, 1885; and May 18, 1978, respectively (Wang et al., 2002). According to the the Liaoning Digital Telemetry Network Bulletin, the 1999 Haicheng-Xiuyan earthquake swarm started with two earthquakes, M_L 4.1 and M_L 4.2 on November 9, 1999. By the time the mainshock, M_S 5.9, occurred on November 29, 1999, 205 earthquakes had been recorded, including 28 - M_L 2.0 ~ 2.9 earthquakes, 10 - M_L 3.0 ~ 3.9 earthquakes and five earthquakes with M_L 4.0 ~ 4.9. The largest foreshocks were two M_L 4.4 events that occurred on November 25 and 26. These events reflect the seismic activity in this region. Figure 1 is a map of major faults (Wang *et al.*, 2002) and historical earthquakes around the Haicheng and Xiuyan area with the 13 SMU-IGPCEA broadband seismic stations (Table 1) superimposed on the image.

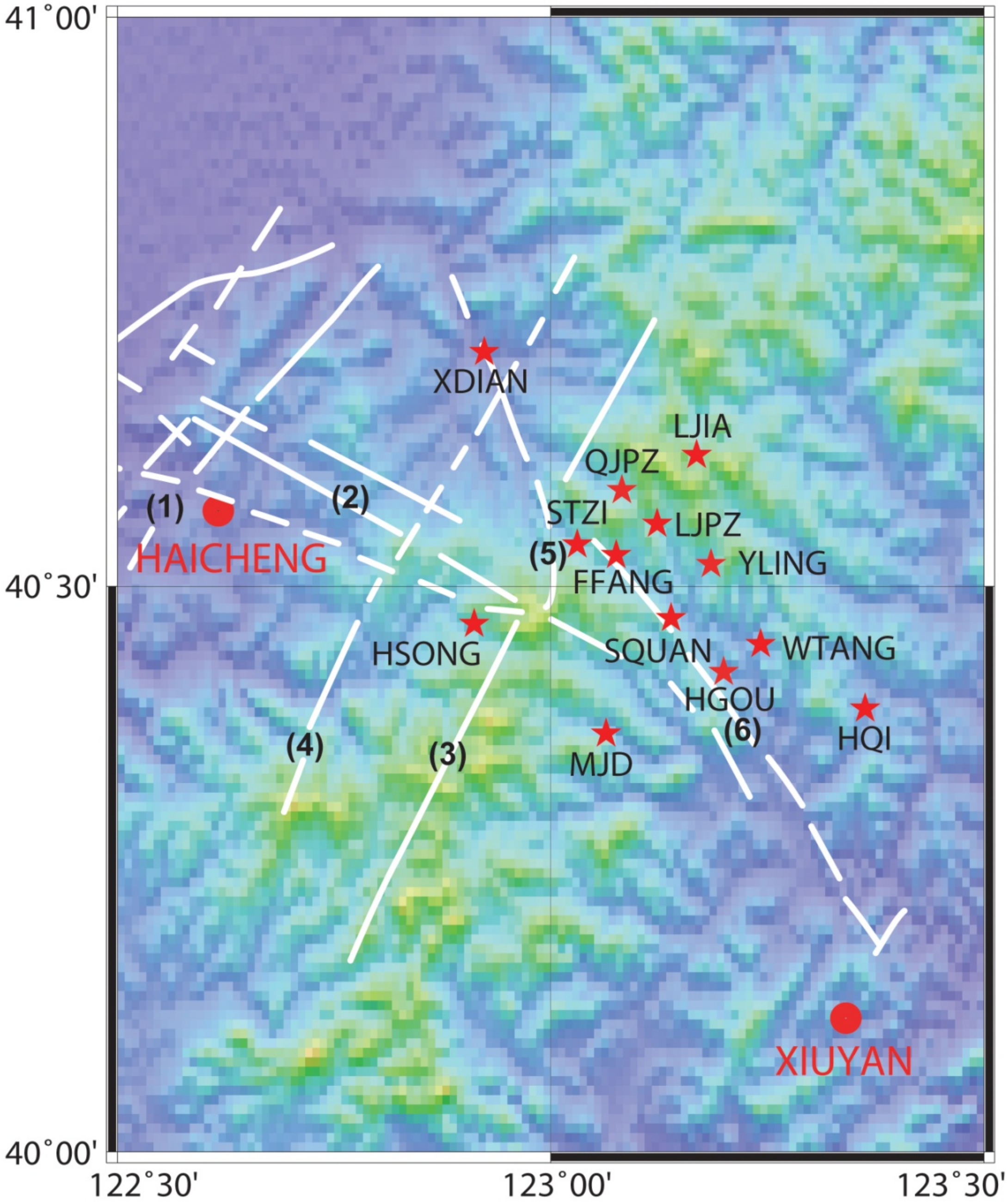

Figure 1. Map of major faults and historical earthquakes around Haicheng and Xiuyan area (after Wang et al., 2002) with the SMU-IGPCEA stations (red stars). Major faults: (1) Jinzhou Fault; (2) Haichenghe-Dayanghe Fault; (3)Tanghe-gushan Fault; (4) Ximu Fault; (5) Kangjialing Fault; and (6) Wangjiabuzi Fault.

Table 1. The Geographical Distribution of the Broadband Seismic Stations

Station Name	Station Code	Latitude (^{o}N)	Longitude (^{o}E)	Elevation (m)
Fenfang	**FFANG**	**40.5286**	**123.0754**	**343.6**
Hegou	**HGOU**	**40.4231**	**123.1966**	**206.9**
Housong	**HSONG**	**40.4678**	**122.9124**	**331.5**
Huangqi	HQI	40.3933	123.3629	198.6
Liangjia	LJIA	40.6167	123.1685	443.9
Liangjiapuzi	**LJPZ**	**40.5561**	**123.1225**	**366.5**
Majiadian	**MJD**	**40.3710**	**123.0640**	**250.7**
Qinjiapuzi	**QJPZ**	**40.5837**	**123.0819**	**321.4**
Suangquan	**SQUAN**	**40.4730**	**123.1387**	**281.2**
Songtuozi	**STZ**	**40.5381**	**123.0307**	**274.6**
Wangtang	**WTANG**	**40.4565**	**123.2385**	**246.0**
Xiandian	**XDIAN**	**40.7072**	**122.9231**	**107.8**
YaoLing	**YLING**	**40.5183**	**123.1837**	**328.1**

DATA SET AND ANALYSIS TOOLS

The seven, temporary, stations in the study consisted of STS-2 seismometers, Quanterra Q330 data acquisition systems and Quanterra PB14 Packet Baler. Two separate vaults were constructed at each site, one for the seismometer and the other for the rest of the equipment in order to reduce noise. Seismometers were deployed where possible in hard rock after excavating the l m x l m x l m vaults. They were covered with a 10 cm thick foam box for additional temperature stability (Zhou *et al.*, 2003a). Data was retrieved during site visits and archived at the IRIS-DMC (Data Management Center).

Seismic Events

Ninety-five, high signal-to-noise ratio teleseismic events with great circle epicentral distances of 30-85 degrees occurring between 2004 and 2008 were chosen for analysis. Source parameters were obtained from the Preliminary Determination of Epicenters (PDE) bulletins provided by the United States Geology Survey (USGS) National Earthquake Information Center (NEIC) (Table 2). The distribution of the 95 teleseismic events is displayed in Figure 2.

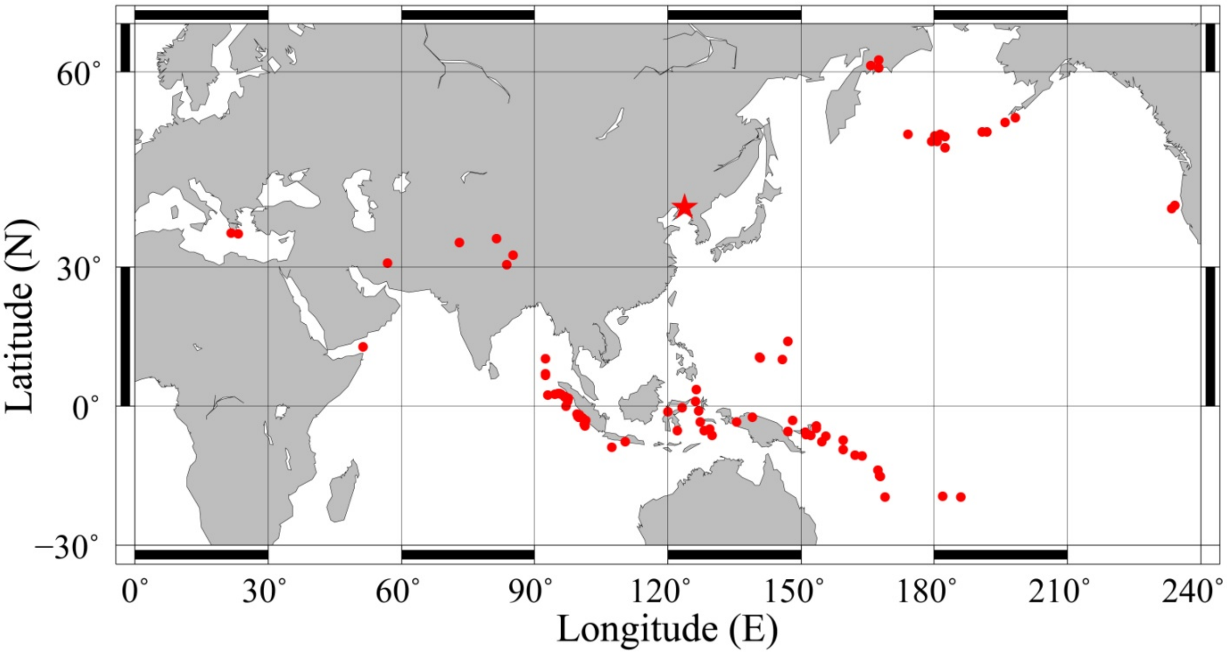

Figure 2. Map of seismic events (red dots). Red start denotes the SMU-IGPCEA seismic network (Fig. 1).

Table 2: List of Event Parameters in the Study

Event Code	Date (yyyy-mm-dd)	Time (hh:mm:ss)	Latitude (N)	Longitude (E)	Magnitude	Depth (km)	Distance to FFANG	FFANG Back Azimuth
2004263	2004-09-19	20:26:04.10	52.21	174.03	6.2	25	36.2	53.7
2004278	2004-10-04	19:20:34.98	14.55	146.99	6	7	33.3	134.4
2004282	2004-10-08	08:27:53.54	-10.95	162.16	6.8	36	62.9	135.9
2004314	2004-11-09	23:58:23.65	-11.15	163.71	6.9	13	63.9	134.6
2004331	2004-11-26	02:25:03.31	-3.61	135.40	7.1	10	45.6	162.6
2005016	2005-01-16	20:17:52.76	10.93	140.84	6.6	24	33.5	147.1
2005017	2005-01-17	10:50:32.56	10.99	140.68	6.1	12	33.4	147.3
2005022	2005-01-22	20:30:17.35	-7.73	159.48	6.4	29	58.7	136.5
2005023	2005-01-23	20:10:12.15	-1.20	119.93	6.3	11	41.8	184.7
2005024	2005-01-24	04:16:47.44	7.33	92.48	6.3	30	43.0	227.8
2005026	2005-01-26	22:00:42.57	2.70	94.60	6.2	22	45.7	221.7
2005039	2005-02-08	14:48:21.97	-14.25	167.26	6.7	206	68.4	133.4
2005050	2005-02-19	00:04:43.59	-5.56	122.13	6.5	10	46.1	181.3
2005053	2005-02-22	02:25:22.92	30.75	56.82	6.4	14	53.5	281.8
2005061	2005-03-02	10:42:12.23	-6.53	129.93	7.1	201	47.5	170.7
2005097	2005-04-07	20:04:41.06	30.49	83.66	6.3	11	33.3	265.1
2005106	2005-04-16	16:38:03.90	1.81	97.66	6.4	31	45.0	217.3
2005118	2005-04-28	14:07:33.70	2.13	96.80	6.2	22	45.2	218.6
2005165	2005-06-14	17:10:12.28	51.24	179.31	6.8	17	39.5	54.8
2005166	2005-06-15	02:50:54.19	41.29	-125.95	7.2	16	77.0	46.1
2005168	2005-06-17	06:21:42.59	40.77	-126.57	6.6	12	77.0	46.8
2005252	2005-09-09	07:26:43.73	-4.54	153.47	7.6	90	53.0	140.8
2005281	2005-10-08	10:46:28.79	34.73	73.10	6.4	8	39.5	278.1
2005309	2005-11-05	10:48:21.22	-3.15	148.14	6.4	25	49.3	146.1
2005323	2005-11-19	14:10:13.03	2.16	96.79	6.5	21	45.1	218.6
2005324	2005-11-20	12:53:02.95	53.84	-164.09	6.2	30	48.9	48.4
2005345	2005-12-11	14:20:45.00	-6.58	152.22	6.6	17	54.2	143.4
2006002	2006-01-02	22:13:40.49	-19.93	-178.18	7.2	582	81.4	125.6
2006008	2006-01-08	11:34:55.64	36.31	23.21	6.7	66	73.7	304.2
2006027	2006-01-27	16:58:53.67	-5.47	128.13	7.6	397	46.2	173.0
2006073	2006-03-14	06:57:33.86	-3.60	127.21	6.7	30	44.3	174.1
2006090	2006-03-31	21:14:45.20	3.80	126.34	6.2	37	36.8	174.6
2006111	2006-04-21	11:14:15.33	61.35	167.52	6.1	12	33.9	37.1
2006115	2006-04-25	18:26:17.15	1.99	97.00	6.3	21	45.2	218.3
2006119	2006-04-29	16:58:06.32	60.49	167.52	6.6	11	33.6	38.5
2006123	2006-05-03	15:26:40.29	-20.19	-174.12	8	55	84.2	122.9
2006130	2006-05-10	02:42:51.03	52.51	-169.26	6.4	18	46.3	51.2
2006136	2006-05-16	15:28:25.92	0.09	97.05	6.8	12	46.8	217.0
2006142	2006-05-22	11:12:00.80	60.77	165.74	6.6	19	32.9	37.6
2006146	2006-05-26	22:53:58.92	-7.96	110.45	6.3	12	49.9	196.4
2006172	2006-06-21	12:34:52.68	6.94	92.45	6	16	43.3	227.5
2006175	2006-06-24	21:15:00.92	-0.39	123.19	6.3	26	40.9	179.8
2006189	2006-07-08	20:40:00.98	51.21	-179.31	6.6	22	40.4	54.7
2006198	2006-07-17	08:19:26.68	-9.28	107.42	7.7	20	51.9	199.8
2006219	2006-08-07	22:18:55.09	-15.80	167.79	6.8	150	70.0	133.9
2006244	2006-09-01	10:18:51.60	-6.76	155.51	6.8	38	55.9	140.0

Table 2. Continued.

Event Code	Date (yyyy-mm-dd)	Time (hh:mm:ss)	Latitude (N)	Longitude (E)	Magnitude	Depth (km)	Distance to FFANG	FFANG Back Azimuth
2006290	2006-10-17	01:25:12.23	-5.88	150.98	6.7	32	53.0	144.4
2006311	2006-11-07	17:38:33.80	-6.48	151.20	6.6	11	53.7	144.4
2006356	2006-12-22	19:50:44.63	10.65	92.36	6.2	24	40.3	230.9
2006364	2006-12-30	08:30:49.79	13.31	51.37	6.6	15	67.6	268.5
2007051	2007-02-20	08:04:25.28	-1.03	126.98	6.7	12	41.7	174.1
2007051	2007-02-20	14:25:26.34	-1.03	126.97	6	11	41.7	174.1
2007076	2007-03-17	17:42:26.29	1.13	126.22	6.2	35	39.5	175.1
2007097	2007-04-07	09:51:51.62	2.92	95.70	6.1	30	45.0	220.5
2007119	2007-04-29	12:41:57.39	52.01	-179.97	6.2	117	39.9	53.6
2007179	2007-06-28	02:52:10.99	-7.98	154.63	6.7	18	56.5	141.6
2007206	2007-07-25	23:37:31.52	7.16	92.52	6.1	15	43.1	227.6
2007213	2007-08-01	17:08:51.40	-15.60	167.68	7.2	120	69.7	133.9
2007227	2007-08-15	20:22:11.12	50.32	-177.55	6.5	9	41.6	55.8
2007228	2007-08-16	08:39:28.44	-9.83	159.46	6.5	15	60.5	137.8
2007229	2007-08-17	03:04:03.09	-5.26	129.43	6.4	10	46.2	171.2
2007255	2007-09-12	23:49:03.72	-2.62	100.84	7.9	35	47.7	210.7
2007255	2007-09-12	11:10:26.83	-4.44	101.37	8.5	34	49.2	209.2
2007256	2007-09-13	16:09:16.87	-3.17	101.52	6	53	47.9	209.6
2007256	2007-09-13	09:48:45.13	3.80	126.34	6.3	26	36.8	174.6
2007257	2007-09-14	06:01:32.27	-4.07	101.17	6.4	23	48.9	209.6
2007263	2007-09-20	08:31:14.49	-2.00	100.14	6.7	30	47.4	211.9
2007269	2007-09-26	12:36:26.89	-4.99	153.50	6.8	40	53.4	141.1
2007269	2007-09-26	15:43:01.44	-1.79	99.49	6.1	26	47.5	212.9
2007273	2007-09-30	02:08:30.17	10.45	145.72	6.9	14	36.1	140.0
2007275	2007-10-02	18:00:06.87	54.51	-161.71	6.3	32	50.1	47.0
2007277	2007-10-04	12:40:31.13	2.54	92.90	6.2	35	46.7	223.6
2007326	2007-11-22	08:48:27.53	-5.76	147.10	6.8	53	51.3	148.7
2007353	2007-12-19	09:30:27.93	51.36	-179.51	7.2	34	40.3	54.5
2007356	2007-12-22	12:26:17.47	2.09	96.81	6.1	23	45.2	218.6
2007356	2007-12-22	07:11:08.10	-2.41	139.07	6.2	20	45.4	157.2
2007360	2007-12-26	22:04:54.67	52.56	-168.22	6.4	25	46.9	50.9
2008004	2008-01-04	07:29:18.30	-2.78	101.03	6	35	47.8	210.4
2008009	2008-01-09	08:26:45.49	32.29	85.17	6.4	10	31.3	267.0
2008022	2008-01-22	17:14:57.95	1.01	97.44	6.2	20	45.8	217.1
2008045	2008-02-14	10:09:22.72	36.50	21.67	6.9	29	74.6	305.2
2008051	2008-02-20	08:08:30.52	2.77	95.96	7.4	26	45.0	220.1
2008055	2008-02-24	14:46:21.47	-2.40	99.93	6.5	22	47.8	212.0
2008056	2008-02-25	18:06:03.90	-2.33	99.89	6.6	25	47.8	212.1
2008056	2008-02-25	21:02:18.42	-2.24	99.81	6.7	25	47.8	212.2
2008056	2008-02-25	08:36:33.03	-2.49	99.97	7.2	25	47.9	211.9
2008063	2008-03-03	02:37:27.12	-2.18	99.82	6.2	25	47.7	212.2
2008075	2008-03-15	14:43:26.50	2.71	94.60	6	25	45.7	221.7
2008080	2008-03-20	22:32:57.93	35.49	81.47	7.2	10	32.9	274.8
2008082	2008-03-22	21:24:11.27	52.18	-178.72	6.2	132	40.6	53.2
2008089	2008-03-29	17:30:50.15	2.86	95.30	6.3	20	45.2	221.0
2008100	2008-04-09	12:46:12.72	-20.07	168.89	7.3	33	74.1	135.5
2008106	2008-04-15	22:59:51.50	51.86	-179.36	6.4	11	40.3	53.7
2008107	2008-04-16	05:54:19.69	51.88	-179.16	6.6	13	40.4	53.7
2008123	2008-05-02	01:33:37.24	51.86	-177.53	6.6	14	41.4	53.5

Receiver Functions

Three-component (3C), broadband recordings of teleseismic P waves with distances from 30 to 85° were used to estimate receiver functions following the procedure outlined by Özalaybey *et al.*, 1997 (Figure 2). P waves dominate the vertical seismograms as a result of the near-vertical incidence with P to S converted waves observed on the horizontal channels. As a result of these converted phases, the 3C receiver functions are strongly affected by the shear wave structure beneath the stations (Owens *et al.*, 1984). Further, as discussed by Ammon *et al.* (1991) the absolute amplitudes of these receiver functions provide some additional information related to the shallow shear velocities and can document the existence of dipping layers in the region (Cassidy, 1992).

The iterative, time-domain deconvolution technique of Ligorría and Ammon (1999) was used to compute the receiver functions following the approach of the Kikuchi and Kanamori (1982). Vertical-component seismograms at 11 of the total 13 stations from a magnitude 6.3 event (Event code: 2007256-2; location: 3.8°N and 126.34°E on September 13, 2007) are presented in Figure 3 to illustrate data quality. Radial receiver functions for this example (Gaussian filter parameter, $\alpha = 1$) are reproduced in Figure 4, documenting the nearly identical receiver functions across the area.

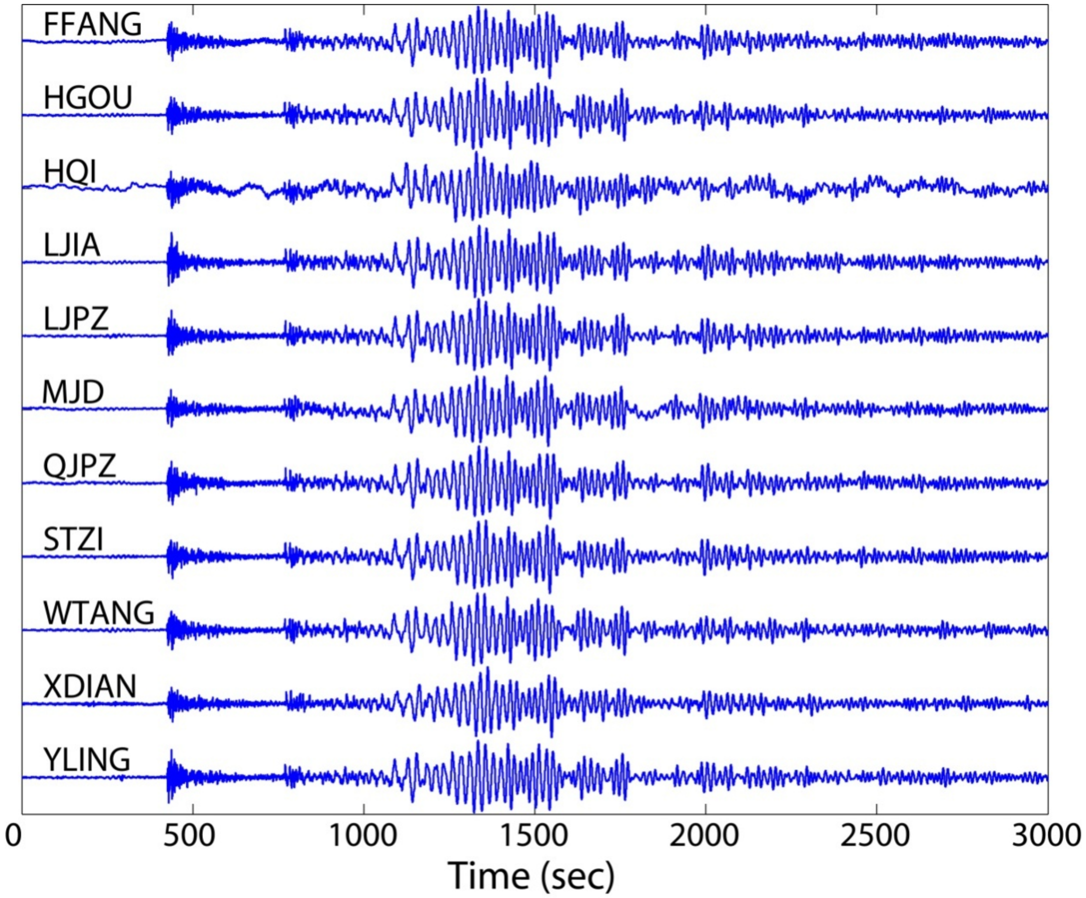

Figure 3. Vertical component seismic waveforms recorded at 11 of total 13 stations for event 2007256_2 (Table 2).

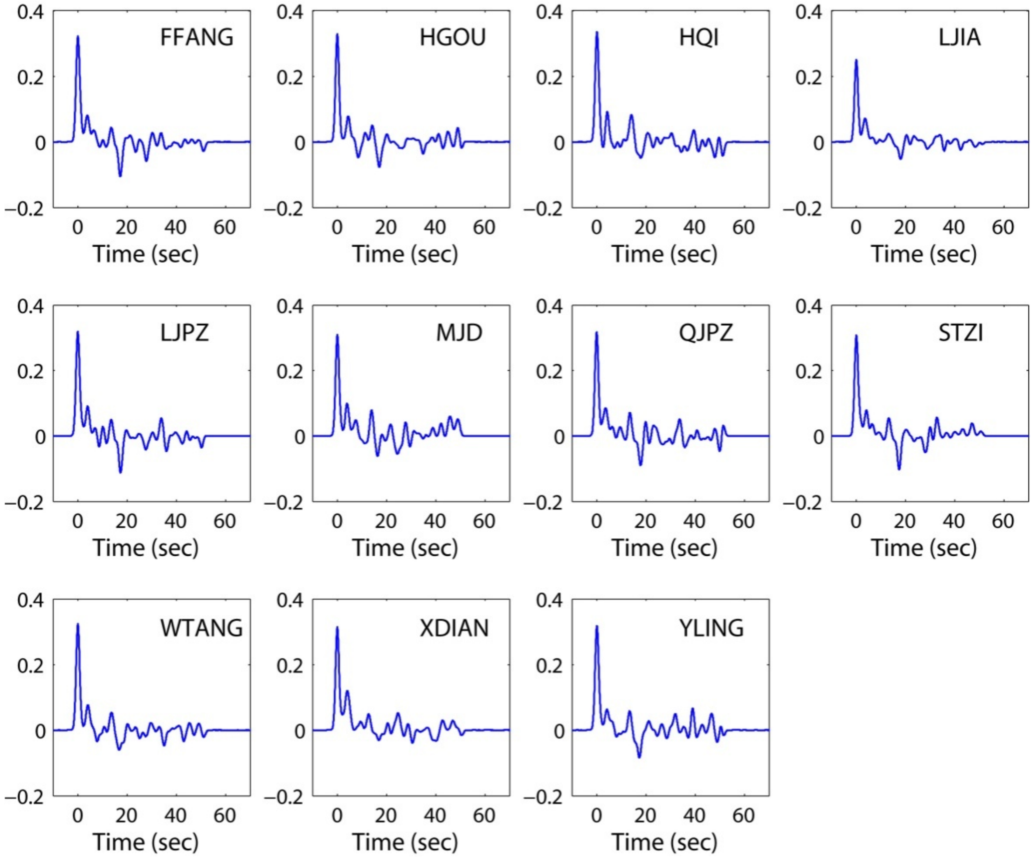

Figure 4. Receiver functions from event 2007256_2 with a Gaussian window parameter, α, of 1.0.

The radial component receiver functions ($\alpha = 1.0$) for all the events in this study at FFANG (93 of 95 events) and LJIA (78 of 95 events) are plotted as a function of source azimuth in Figure 5. These receiver functions exhibit very modest azimuthal variation.

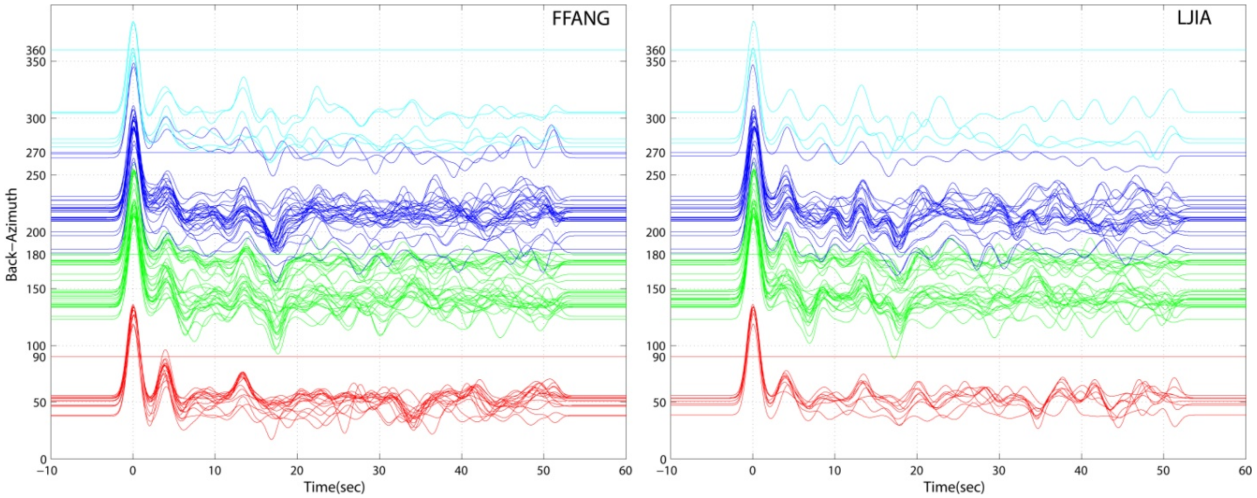

Figure 5. Receiver functions versus back-azimuth for all events recorded at stations FFANG (Left: 93 events) and LJIA (Right: 78 events) with Gaussian window parameters α of 1.0.

Surface Waves

McMechan and Yedlin (1981) outline a methodology for estimating phase velocities under a network and extracting the fundamental mode Rayleigh wave. Data is projected onto a line that follows the great circle path and a *p*-τ stack is applied. These results are transformed into *p*-ω space providing an estimate of the dispersion. We used seven stations from our deployment in his procedure, thus assuming a uniform structure beneath these stations for depths larger than about 1/3 the smallest wavelength.

Fundamental mode Rayleigh waves from the 95 events of this study were extracted using Multiple Filter Analysis (Dziewonski *et al.*, 1969) and Phase Matched Filtering (Herrin and Goforth, 1977). The fundamental mode Rayleigh waves for event 2007256-2 (20 to 100 s) are displayed in Figure 6. Phase velocities are estimated using the stacking technique previously discussed with the mean phase velocities and errors resulting from this analysis displayed in Figure 6. Phase velocity estimates ranged from 3.5 to 4.23 km/s increasing with period (20 to 80 seconds). Standard deviations of the estimates ranged from 0.001 to 0.41 km/s. Typically the depth sensitivity of these phase velocities is proportional to 1/3 to ½ a wavelength (Beaty *et al.*, 2002; Li and Detrick 2006). In particular for our period range, the upper mantle velocity structure is constrained by the dispersion curves. The small scatter in phase velocities is attributable to the narrow array aperture, local site effects, and non-plane waves across the array. The mean phase velocities at each frequency are used in the inversions weighted by the standard deviation of the estimates.

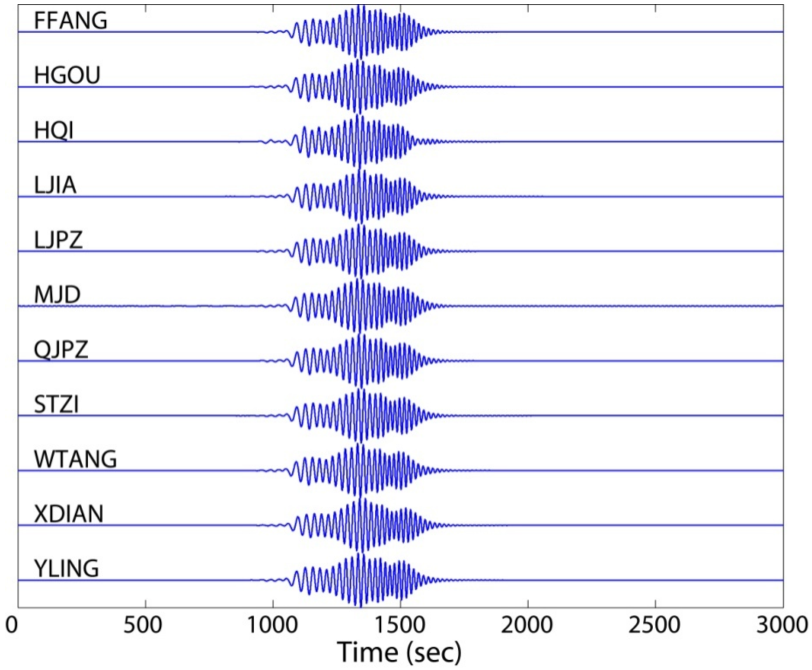

Figure 6. Fundamental Rayleigh wave (20-100 sec) extracted from vertical component seismograms using multiple filter analysis and phase matched filter for event 2007256_2.

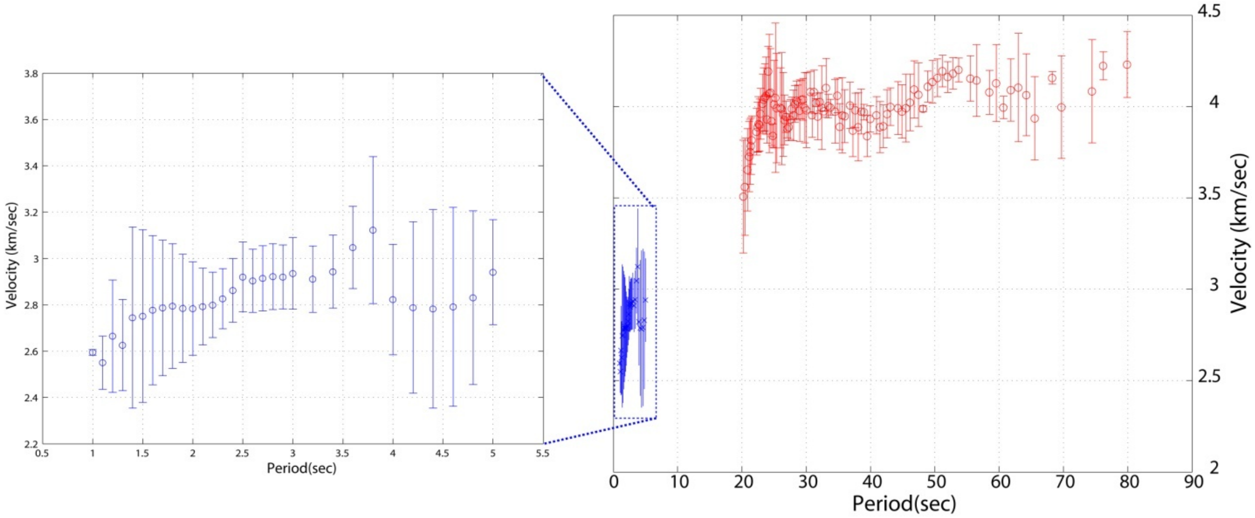

Figure 7. Averaged phase velocity (red) and group velocity (blue) dispersion curves with ± 1 standard deviation.

Noise Correlation and Extraction of Short Period Surface Waves

Using ambient noise and correlation techniques to extract surface waves between pairs of stations has evolved significantly since the first work by Shapiro et al. (2005). These noise correlation techniques have proven to provide data that is useful in constraining the shallow crust and upper mantle in a large number of studies and have been particularly useful in areas where there are few regional events that generate intermediate period surface waves. Continuous vertical-component seismic data from the initial five stations deployed in the Haicheng-Xiuyan region (FFANG, HSONG, LJIA, MJD and XDIAN, Figure 1) provided five-months of data from 2004 to which this analysis approach was applied. Stacked cross-correlation functions for pairs of these five stations are illustrated in Figure 8. Fundamental Rayleigh waves were extracted using Multiple Filter Analysis and Phase Matched Filtering as discussed previously. The resulting dispersion curves are reproduced in Figure 9. The estimated group velocities range from 2.55 to 3.12 km/s over the period range of 1 to 5 seconds with standard deviations between 0.012 and 0.43 km/s (Figure 7).

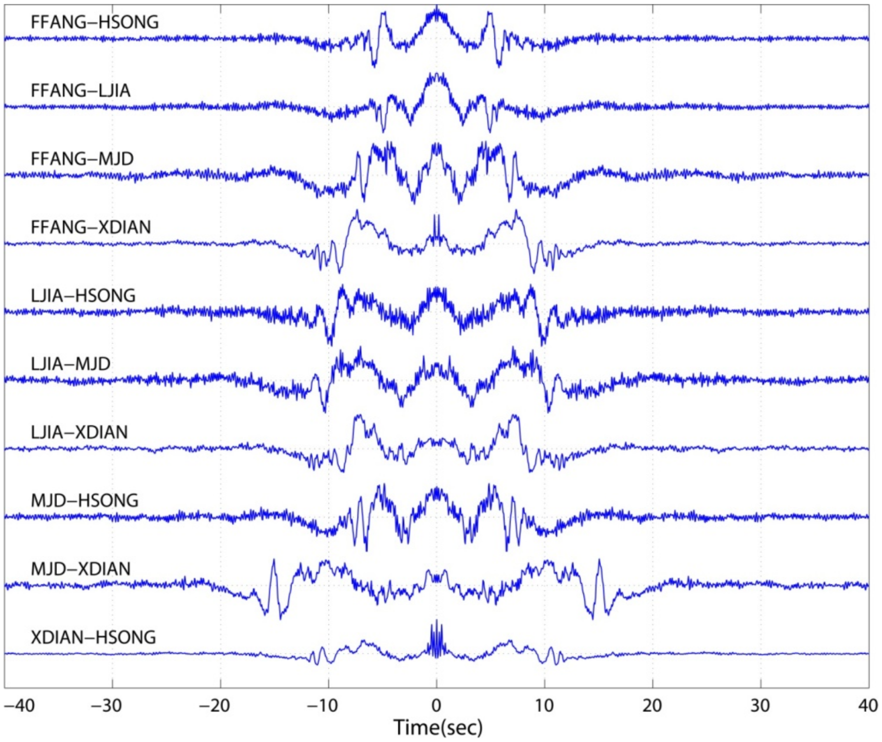

Figure 8. Cross-correlation functions between station pairs from continuous vertical-component seismic data from the five stations (FFANG, HSONG, LJIA, MJD and XDIAN) deployed in the Haicheng-Xiuyan region over the first five months of 2004.

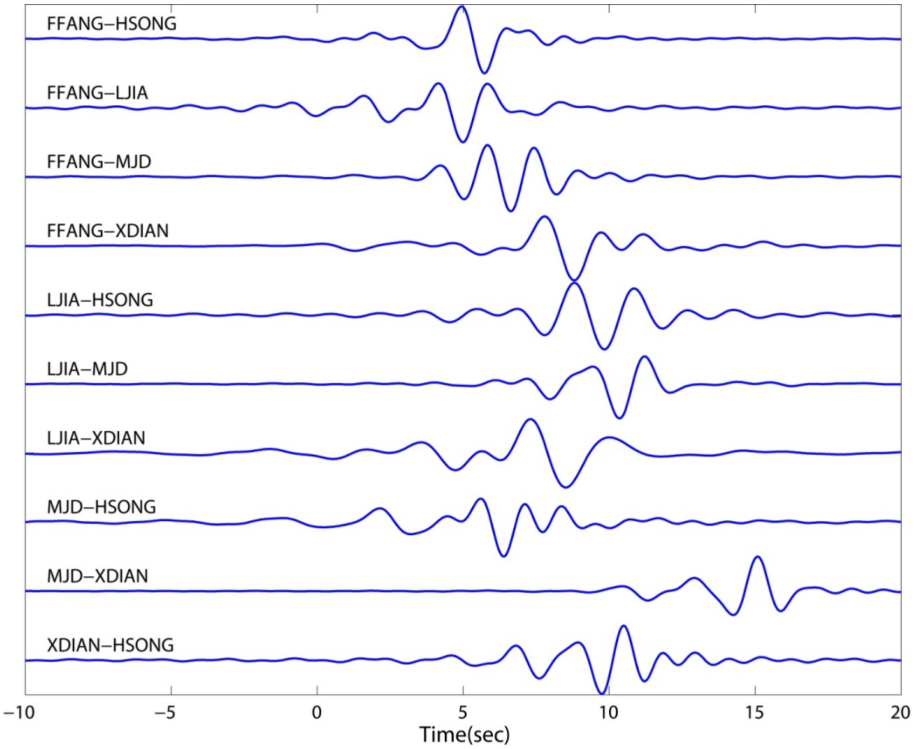

Figure 9. Fundamental Rayleigh waves extracted from cross-correlations in Figure 7 and station pairs illustrated in Figure 1.

JOINT INVERSION RESULTS AND CONCLUSIONS

The linearized and iterative, least-squares waveform fitting procedure as described by Herrmann and Ammon, 2002 was used in the data inversion for shear velocity. Partial derivatives of the surface wave dispersion curves relative to model parameters were computed analytically and the partial derivatives of the theoretical receiver functions relative to model parameters were numerically estimated. Shear wave velocities were estimated by fixing the ratio of P to S velocity in each layer. Density was computed from the P velocity at each iteration in the procedure. In order to estimate a smooth velocity model, a constraint was applied by solving for the change in velocity at each boundary. The assumed depth model consisted of forty-five plane layers extending from the surface to 200 km with the first 25 layers each 2 km thick (50 km depth), the next 10 layers each 5 km thick (100 km depth), and the last 10 layers each 10 km thick (200 km depth). The first 50 km of the model started with the single velocity value of AK135-F at 50 km. Below this depth model started with the velocity specified in the AK135-F continental model (Kennett *et al.*, 1995 and Montagner and Kennett, 1995) at each depth. Fast velocities in the shallow crust provide a starting model that is unbiased. We did not want to make assumptions about the depth to the Moho or any other crustal layering affecting the choice of starting model. Additionally, we did not allow large departures from the starting model below 80 km so that the resulting models would be consistent with global experience

The joint inversion of the receiver functions and surface wave dispersion curves at each station across the study area was conducted. Figure 10 illustrates the starting model in black and the final velocity model in blue at each station in the network. The number of receiver functions used at each station varied as not all 95 events were well recorded by every station: FFANG - 93, HGOU - 36, HQI - 43, HSONG - 34, LJIA - 78, LJPZ - 48, MJD - 62, QJPZ - 32, SQUAN - 5, STZI - 38, WTANG - 61, XDIAN - 44 and YLING - 33. Based on the similarity of receiver functions across the network (Figure 4) and the similarity of receiver functions with azimuth (Figure 5), a joint inversion using all of the receiver functions at the 13 stations and group velocities from the ambient noise analysis was conducted in order to estimate an averaged velocity model for the region. Figure 10 compares the station specific velocity models (blue) against the averaged model (red dotted) for the stations. The individual velocity models at depth exhibit little or no difference across the network as expected based on the common surface wave dispersion data and receiver functions.

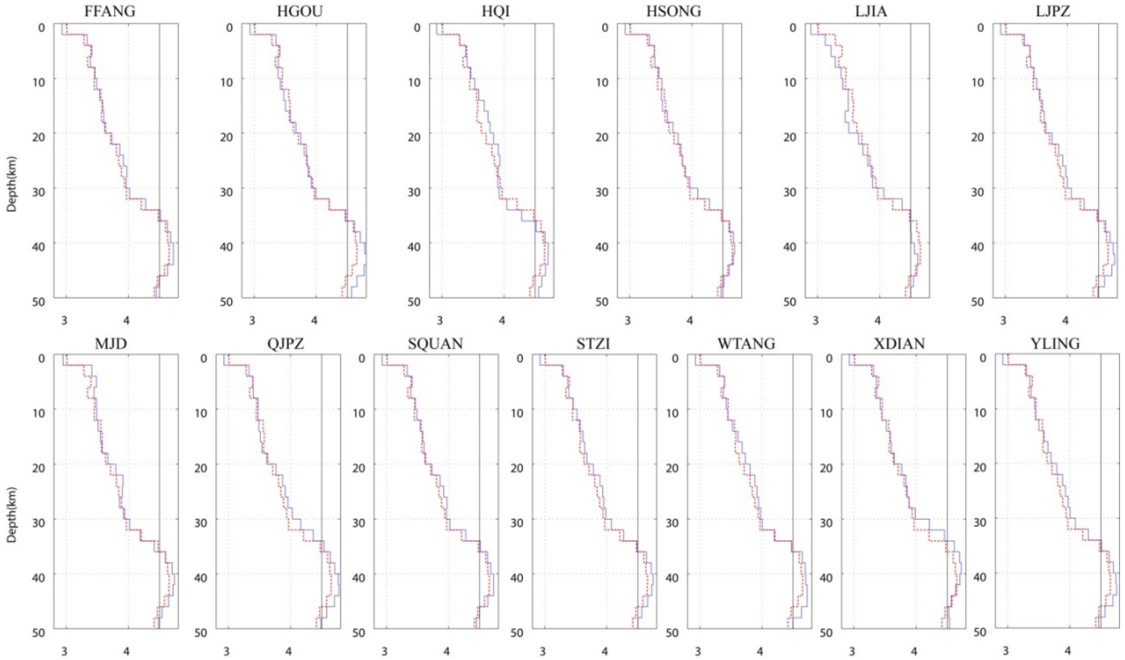

Figure 10. Comparison of shear-wave velocity models from joint inversions at each of the 13 stations (blue solid) to the averaged model inverted using all 13 stations (red dotted) simultaneously. Black line is the starting model.

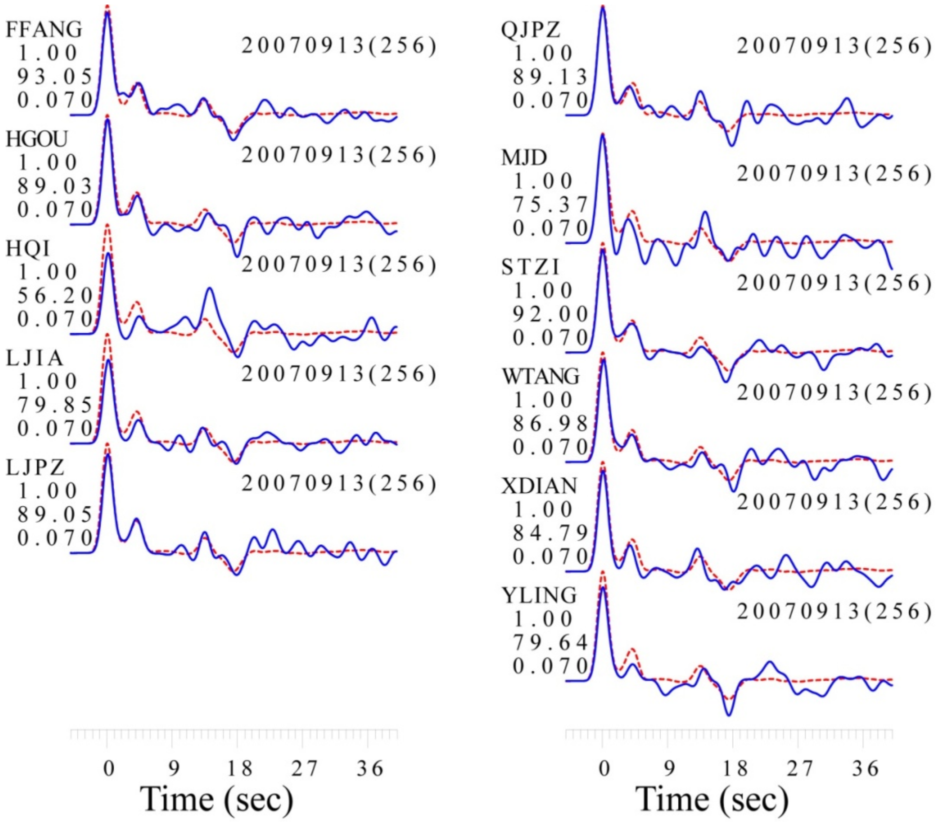

Figure 11. Comparison between observed (blue solid) and predicted receiver functions (red dotted) after inversion. The receiver functions are labeled with the year/month/day (day of year) to the upper right of each trace, and with the station name, Gaussian filter parameter, the percentage of fit, and the ray parameter (sec/km) to the left of each trace.

Figure 11 presents the comparison between observed (blue) and predicted receiver functions (red) after inversion. The receiver functions are labeled with the year/month/day (day of year) to the upper right of each trace, and with the station name, Gaussian filter parameter, the percentage of fit, and the ray parameter (sec/km) to the left of each trace. At most of stations, the predicted receiver functions match the observed with 80% or higher of the filtered radial signal.

A number of studies of crustal and upper mantle structure have been conducted in the area of northeast China after the 1975 Haicheng Earthquake (Lu, 1985; Lu *et al.*, 1987; Lu *et al.*, 1990; Niu *et al.*, 2000; Pan, *et al.*, 2001; and Lu *et al.*, 2005). Their results indicated that the depth of Moho discontinuity is 31–34 km under the Haicheng-Xiuyan area and possible low velocity layer exists at the depth range between 21–28 km. Our averaged velocity model for this region is consistent with Moho depths estimated by these earlier studies although there is little evidence of a significant low velocity zone.

A joint inversion of teleseismic receiver functions and surface wave group velocities from ambient noise analysis has been conducted and the shallow crustal shear velocity structure around Xiuyan area estimated. Crustal thickness beneath the Xiuyan area is about 34 km, which is consistent with the results from other geophysical studies in this region.

ACKNOWLEDGEMENTS

The authors would like to thank Mary Templeton, Eliana Arias, Xiang-Wei Yu, Xiang-Tong Xu and Shi-Yu Bai for their help with network installation, data collection, and archiving. A large portion of the success of this experiment is due to the outstanding help and support of the seismological bureaus and seismic station operators in these regions. IRIS PASSCAL Instrument Center provided the STS-2 seismometers, Quanterra Q-330 and Baler systems.

REFERENCES

Ammon, C. J. (1991). The isolation of receiver effects from teleseismic P waveforms, *Bull. Seism. Soc. Am.* **81,** 2504-2510.

Beaty, K. S, D. R. Schmitt, and M. Sacchi (2002). Simulated annealing inversion of multimode Rayleigh wave dispersion curves for geological structure, *Geophys. J. Int.* **151,** 622-631.

Cassidy, J. F. (1992). Numerical experiments in broadband receiver function analysis, *Bull. Seism. Soc. Am.* **82,** 1453-1474.

Dziewonski, A., S. Bloch, and M. Landisman (1969). A technique for the analysis of transient seismic signals, *Bull. Seism. Soc. Am.* **59,** 427-444.

Herrin, E., and T. Goforth (1977). Phase-matched filters: application to the study of Rayleigh waves, *Bull. Seism. Soc. Am.* **67,** 1259-1275.

Herrmann, R. B. and C. J. Ammon (2002). *Computer Programs in Seismology: Surface Waves, Receiver Functions and Crustal Structure*, Version 3.15.

Kennett, B. L. N., E. R. Engdahl, and R. Buland R. (1995). Constraints on seismic velocities in the earth from travel times, *Geophys. J. Int* **122,** 108-124.

Kikuchi, M. and H. Kanamori (1982). Inversion of complex body waves, *Bull. Seism. Soc. Am*. 72**:** 491–506.

Li, A., and R. S. Detrick (2006). Seismic structure of Iceland from Rayleigh wave inversions and geodynamic implications, *Earth Planet. Sci. Lett.* **241,** 901-912.

Ligorria, J. P. and C. J. Ammon (1999). Iterative deconvolution of teleseismic seismograms and receiver function estimation, *Bull. Seism. Soc. Am.* 89**:** 1395–1400.

Lu, Z.-X. (1985). Progress of geophysical prospecting study on the deep structure of Haicheng earthquake area, *Earthquake Research in China* 1**,** 56–65 (in Chinese with English abstract).

Lu, Z.-X., G.-C. Zhang, J.-Z. Li, L.-Z. Wang, and J.-M. Zhao (1987). Research on tectonic characteristics of the crust and upper mantle in Haicheng seismic area, *Journal of Changchun College of Geology* 17 (1): 99–108 (in Chinese with English abstract).

Lu, Z.-X., G.-D. Liu, M.-H. Wei, B.-Z. Meng, and J.-M. Zhao (1990). Lateral inhomogeneity of crust and upper mantle in South Liaoning, China and its relationship with the *M* 7.3 Haicheng earthquake, *ACTA Seismological Sinica* 12**:** 367–378 (in Chinese with English abstract).

Lu, Z.-X., D.-L. Jiang, Y. Bai, X. Niu, and B.-Z. Meng (2005). Exploration and research on the structure of the crust and upper mantle in Northeast China, *Seismological Research of Northeast China* 21(1): 1–8 (in Chinese with English abstract).

McMechan, G. A., and M. J. Yedlin (1981). Analysis of dispersive waves by wave field transformation, *Geophysics* **46,** 869-874.

Montagner, J. P. and B. L. N. Kennett (1995). How to reconcile body-wave and normal-mode reference Earth models? *Geophys. J. Int.* **125,** 229-248.

Niu, X., Z.-X. Lu, D.-L. Jiang, Q.-Q. Lei, and S.-C. Shi (2000). Crust-mantle structure feature and the seismic activity of the main tectonic units in the North Tanlu fault zone, *ACTA Seismologica Sinica* 13**:** 159–165.

Owens, J. T., G. Zandt and S. R. Taylor (1984). Seismic evidence for an ancient rift beneath the Cumberland Plateau, Tennessee: A detailed analysis of broadband teleseismic P waveforms, *J. Geophys. Res.* **89,** 7783-7795.

Özalaybey, S., M. K. Savage, A. F. Sheehan, J. N. Louie and J. N Brune (1997). Shear-wave velocity structure in the Northern Basin and Range Province from the combined analysis of receiver functions and surface waves, *Bull. Seism. Soc. Am.* 87, 183-199.

Pan, K., X.-Q. Jiang, Z.-Z. Lu, and P. Zhang (2001). Three dimension velocity image of the crust and upper mantle in Liaoning and its neighbor regions, *Seismological and Geomagnetic Observation and Research* 22**:** 92–98 (in Chinese with English abstract).

Shapiro, N. M., M. Campillo, L. Stehly, and M. H. Ritzwoller (2005). High resolution surface wave tomography from ambient seismic noise, *Science* 307: 1615–1618.

Wang, A.-D., G.-Y. Gu, H. Huang and Y. Zhang (2002). Haicheng-Xiuyan 5.4 and 5.1 earthquakes on November 29, 1999, and January 12, 2000, in Liaoning Province, *Earthquake Cases in China (1997-1999)*, edited by Q.-F. Chen. Seismological Press, Beijing, China (in Chinese with English abstract).

Zhou, R.-M., B. W. Stump, Y.-T. Chen, C. T. Hayward, Z.-X. Yang, M. Templeton, X.-W. Yu, S.-Y. Bai and X.-T. Xu (2003). Network installation in the Yanqing-Huailai Basin and preliminary study of natural and man-induced events. *Proceedings of the 25th Seismic Research Review — Nuclear Explosion Monitoring: Building the Knowledge Base*, September 2003, LA-UR-03-6029, Los Alamos National Laboratory, Los Alamos, NM, 504-513.

Chapter 3

Infrasonic Observations from the February 21, 2008 Wells Earthquake

Authors: Relu Burlacu(1), Stephen Arrowsmith(2), Chris Hayward(3), Brian Stump(3Z)

Affiliation and Addresses of Authors:
(1) University of Utah Seismograph Stations
(2) Los Alamos National Laboratory
(3) Roy M. Huffington Department of Earth Sciences
Southern Methodist University
Dallas, TX 75275, USA

Prepared for USGS publication on the Wells Earthquake Sequence

ABSTRACT

Infrasonic signals from the February 21, 2008 Wells earthquake were observed at five infrasonic arrays in Nevada, Utah and Wyoming. The records include acoustic signals generated in the epicentral area that propagated through the atmosphere to the arrays and signals generated by ground motion at the infrasonic array (local infrasound) that coupled into the atmosphere close to the array (before reaching the arrays these waves propagated as seismic waves). There are also observations that we associate with infrasonic signals generated by secondary sources—regions that can be remote from the epicenter.

INTRODUCTION

Infrasonic signals, which correspond to acoustic energy at frequencies below the audible range of the human ear (~20 Hz), can be generated by avalanches, meteors, ocean waves, weather systems, volcanoes, explosions, earthquakes, and communication between animals (Bedard and Georges, 2000). Low frequency infrasound (< 5 Hz) propagates efficiently and can be detected at large distances (>300 km). Sound velocity, a function of altitude dependent on the temperature and wind distribution, controls where upward radiated acoustic energy turns downward in the atmosphere and reaches stations on the ground. Measuring infrasound using arrays of sensors allows for the estimation of phase velocity and the direction (backazimuth) of the signal wavefront and separation of signals from local noise sources generated by winds. Infrasound is one of the technologies used to monitor nuclear explosions, especially those in the atmosphere, using infrasonic arrays installed as part of the International Monitoring System (http://ctbto.org).

Several studies document infrasound generated by medium to large earthquakes (Cook, 1971; Kim et al., 2004; Mutschlecner and Whitaker, 2005; Le Pichon et al., 2006) and describe three possible mechanisms to explain this process: (1) conversion of surface ground motions to sound pressure in the epicentral area and propagation through atmosphere to the infrasound recording stations (also known as epicentral infrasound); (2) induced pressure changes due to vertical ground displacement of the seismic waves that travelled from the epicentral area and coupled acoustically near the infrasound recording station (local infrasound); (3) radiated pressure waves as a result of the interaction of seismic surface waves with mountain ranges (diffracted infrasound). For some infrasound sensors, the local infrasound can be in part contaminated by the response of the microbarometer (sensor) to ground motion (Alcoverro et al. 2005; Le Pichon et al., 2006). The sensors used in this study are relatively insensitive to ground motion and thus minimize this problem.

Understanding how earthquakes generate infrasound—including the effects of magnitude, depth, source mechanism—is an active area of research. Most studies documenting earthquake generated infrasound are based on the analysis of very large earthquakes (Le Pichon et al., 2002, Kim et al., 2004, Le Pichon et al., 2006). The Wells earthquake is an interesting case because it is a moderate to strong earthquake that was recorded regionally by multiple arrays, providing a good opportunity to advance our understanding of the mechanism by which earthquakes generate infrasound. The recordings of the Wells earthquake at five infrasonic arrays in Nevada, Utah and Wyoming allow us to estimate phase velocity and backazimuth values using array processing techniques and to use this information in a location exercise based on infrasound data only.

On February 21, 2008 at 14:16:02 UTC an earthquake of magnitude M_W 6.0, epicentral coordinates 41.153°N, 114.867°W, depth 6.7 km (University of Nevada, Reno (UNR) solution on the USGS website, http://earthquake.usgs.gov/eqcenter/eqinthenews/2008/us2008nsa9/), with a focal mechanism indicating normal faulting, occurred in the proximity of Wells, Nevada. The

earthquake was felt in Nevada, Utah, California, Idaho, Montana, Wyoming, Arizona, Oregon, and Washington. More than 3100 entries in more than 300 ZIP areas were reported on the "Did you feel it" website (http://pasadena.wr.usgs.gov/shake/STORE/X2008nsa9/ciim_display.html).
This event was very well recorded by many seismic stations, including the EarthScope TA stations, and was also recorded by three infrasonic arrays in Utah (BGU, EPU, NOQ), one in Nevada (NVIAR), and one in Wyoming (PDIAR). Figure 1 shows the map with the UNR location of the Wells event (red star) and the five infrasonic arrays. Also shown is the infrasound location polygon (red lines) resulting from the application of a grid-search location scheme implemented in the InfraMonitor software package (Arrowsmith et al., 2008).

THE UTAH INFRASONIC ARRAYS

The University of Utah Seismograph Stations (UUSS) has integrated three infrasonic arrays into its regional seismic network. The infrasound integration was related to an experiment conducted during the summer of 2007 in order to measure seismo-acoustic signals associated with the rocket motor detonations in northern Utah (Stump et al., 2007). The infrasonic arrays, co-located with UUSS-operated seismic stations BGU, EPU, and NOQ, record continuous data. Each array consists of four infrasound gauges with 3 gauges on a triangle ~100 m on a side plus one in the center of the triangle. To reduce wind noise, the infrasound sensors are attached to a set of porous hoses.

The array design (geometry of the sensor distribution, distance between sensors) allows for signal enhancement through beamforming of the coherent signals from individual sensors. Array processing techniques take advantage of the coherent signals to estimate phase velocity and backazimuth values for the signals of interest. An important source of inherent noise for the infrasound sensors is wind and this noise increases with wind velocity (Stump et al., 2004).
Data from all three arrays are telemetered in real-time to UUSS, at the University of Utah, in Salt Lake City. Table 1 presents the characteristics of the Utah infrasonic arrays.

Infrasonic Observations

Using the UNR location for the Wells main event, the great circle distance between the epicenter and the five arrays is estimated between ~160 km and ~470 km, with azimuths between ~65° and ~225°. Table 2 displays the information related to distance, azimuth, and backazimuth values from the earthquake to the five infrasonic arrays. The waveforms recorded at the five infrasonic arrays (band-pass filtered between 1 and 5 Hz), shown in figure 2, have durations from 15-18 min for BGU, EPU, and NOQ to ~30 min for NVIAR and PDIAR. The main characteristics of the waveforms from the five arrays are: (1) the presence of signals corresponding to P and S arrivals—they are the result of the coupling-to-air of the seismic waves that traveled to the vicinity of the infrasonic stations (local infrasound); (2) the presence of signals corresponding to a secondary source of infrasound between the source and receiver; and (3) the epicentral infrasound (acoustic energy that was generated by the ground motion at the epicenter and traveled through the atmosphere to the arrays at air sound speed). Due to large differences between seismic and air sound speed, the epicentral infrasound arrives at the stations well after the local infrasound. Table 3 presents the amplitude measurements (in Pa) for the three Utah arrays (waveforms filtered between 1 and 5 Hz) for local infrasound from both P and S waves and epicentral infrasound.

Figure 3 compares the acoustic signal recorded at one of the sensors of the arrays BGU, EPU, and NOQ (blue traces) with the seismic signal recorded on the vertical component of a co-located seismic station (red traces). BGU and NOQ are equipped with broadband instruments, while EPU is a short-period seismic station. Waveforms from seismic and infrasound sensors were band-pass filtered between 1 and 5 Hz. P and S waveforms for the main event and the aftershock that occurred at 14:21 (M 4.7) are evident on the seismic records at BGU, EPU, and NOQ. The waveforms recorded at the infrasonic arrays exhibit more complex features (local and epicentral infrasound from the main event are observed on all the arrays).

To understand the infrasound signal character, we used the software programs PMCC (Cansi, 1995), InfraTool (MatSeis, Hart and Young, 2005), and InfraMonitor (Arrowsmith et al., 2008). These software programs use array processing techniques to estimate the phase velocity and the backazimuth of coherent signals. InfraMonitor uses a coherent detector with an adaptive noise hypothesis to account for variations in ambient noise (Arrowsmith et al., 2009). Using the bulletin data generated by the coherent detector, the InfraMonitor software package searches a geographic region (using a grid-search algorithm) to locate the source based on estimated backazimuths and inter-array delay times. The location of the Wells event using epicentral arrivals only (with corresponding uncertainties) is represented in figure 1 by the outlined area in red.

Results from the preliminary analysis of the waveforms recorded at the BGU infrasonic array, using InfraTool (Hart and Young, 2005) are shown in figure 4. The panels in figure 4 present, from top to bottom, results of correlation, trace velocity, azimuth, and the waveforms of one of the BGU sensors. The phase velocity and azimuth estimates for the epicentral infrasound (well correlated waveforms from14:25 to 14:30) are 370 m/s and 281°, respectively. The azimuth value is in good agreement with the great circle backazimuth of 280° (table 2). This agreement suggests that the observed signal originated in the epicentral area (conversion from seismic waves to sound pressure) and traveled through the atmosphere to BGU, following a path along the great circle between the epicenter and the recording station. The long duration of the epicentral infrasound can be attributed to the complexity of the propagation paths, including possible refractions at different atmospheric heights and multiple bounces of the acoustic energy on the ground surface.

Two interesting signals identified on the records at BGU occur at ~14:19 and ~14:24 and are presented in figure 5. This figure shows the results of beamforming using the PMCC software (Cansi, 1995) for the signals at ~14:19 (top) and ~14:24 (bottom). They have similar waveform characteristics, a phase velocity of ~350 m/s, an azimuth of ~265°, and dominant frequency of 3 Hz. The good correlation of the two signals (the delays that resulted from the beamforming process are very similar) and the fact that the maximum amplitude for the first signal (~14:19) has a corresponding travel time (with respect to the M_W 6.0 event) equal to the one of the maximum amplitude of the second signal (~14:24) relative to the origin time of the aftershock at ~14:21, suggest that: (1) the two signals are related to two different events (main shock and aftershock), and (2) they seem to share a similar mechanism. For each event, the group velocities associated with the arrivals at ~14:19 and ~14:24 are too slow to be pure-seismic and too fast to be pure-acoustic signals. A possible interpretation of this mechanism is that the seismic surface waves from the main shock (or the aftershock) traveled from the epicenter to an area where they coupled to the atmosphere and generated pressure waves that arrived at the station traveling through the atmosphere along an azimuth (265°) different from the station-event azimuth (280°). Based on the arrival azimuths (and the associated uncertainties) and the travel times, this coupling location may correspond to the Floating Island, an isolated mountain, northeast of the area of Bonneville Salt Flats State Park, in the western Great Salt Lake Desert, Utah. If this model is correct, the area where the coupling occurred acts as a secondary source (the approximate location of the Floating Island is 40.915° N, 113.638° W). A detailed analysis of these signals will be presented in a forthcoming paper. The interaction of the seismic surface waves from earthquakes with topographic features, acting as secondary sources of acoustic energy, is often described as a diffraction process (Le Pichon et al., 2002; Mutschlecner and Whitaker, 2005).

CONCLUSIONS

Infrasonic observations from the Wells earthquake were recorded at five infrasonic arrays in Nevada, Utah and Wyoming. A preliminary analysis of the waveforms recorded at the infrasonic array BGU indicates the presence of local and epicentral infrasound, as well as infrasound generated by a secondary source. The Wells earthquake presents an interesting case study that can improve our understanding of how earthquakes generate infrasound. To make this improvement, detailed studies that relate the seismic wave field to infrasound are needed. Also, modeling studies are necessary to better identify the source of different infrasonic signals recorded by the five arrays.

ACKNOWLEDGMENTS

We thank Kris Pankow and Jim Pechmann for insightful discussions.
Contract FA8718-05-C-0020, Air Force Research Laboratory, has supported the array deployments at BGU, EPU, and NOQ.

REFERENCES

Alcoverro, B., Martysevich, P.N., and Starovoit, Y.O., 2005, Mechanical sensitivity of microbarometers MB2000 (DASE, France) and Chaparral 5 (USA) to vertical and horizontal ground motion: Inframatics, vol. 09, March 2005.

Arrowsmith, S.J., Whitaker, R., Taylor, S.R., Burlacu, R., Stump, B., Hedlin, M., Randall, G., Hayward, C., and ReVelle, D., 2008, Regional monitoring of infrasound events using multiple arrays -: Application to Utah and Washington State: Geophyical Journal International, vol. 175, p. 291-300.

Arrowsmith, S.J., Whitaker, R., Katz, C., and Hayward, C., 2009, The F-detector Revisited: An Improved Strategy for Signal Detection at Seismic and Infrasound Arrays: Bulletin of the Seismological *Soc*iety of America, vol. 99, p. 449-453.

Bedard, A.J. and Georges, T.M., 2000, Atmospheric infrasound: Physics Today, vol. 53(3), p. 32-37.

Cansi, Y., 1995, An automatic seismic event processing for detection and location - the PMCC method: Geophysical Research Letters, vol. 22, p. 1021–1024.

Cook, R.K., 1971, Infrasound radiated during the Montana earthquake of 1959 August 18, Geophysical Journal of the Royal Astronomical Society, vol. 26, p. 191–198.

Hart, D. and Young, C., 2005, MatSeis, User's manual, version 1.10, Sandia National Laboratories.

Kim, T.S., Hayward, C., and Stump, B., 2004. Local infrasound signals from the Tokachi-Oki earthquake: Geophysical Research Letters, doi:10.1029/2004GL021178.

Le Pichon, A., Guilbert, J., Vega, A., Garcés, M., and Brachet, N., 2002, Ground-coupled air waves and diffracted infrasound from the Arequipa earthquake of June 23, 2001: Geophysical Research Letters, vol. 29 (18), doi i10.1029/2002GL015052.

Le Pichon, A., Mialle, P., Guilbert, J., and Vergoz, J., 2006, Multistation infrasonic observations of the Chilean earthquake of 2005 June 13: Geophysical Journal International, vol. 167(2), p. 838-844.

Mutschlecner, J.P. and Whitaker, R.W., 2005, Infrasound from earthquakes: Journal of Geophysical Research, 110, doi:10.1029/2004JD005067.

Stump,., B., Jun, M.S., Hayward, C., Jeon, J.S., Che, I.Y., Thomason, K., House, S.M., and McKenna, J., 2004, Small-aperture seismo-acoustic arrays - design, implementation, and utilization: Bulletin of the Seismological Society of America, vol. 94, p. 220-236.

Stump, B., Burlacu, R., Hayward, C., Bonner, J., Pankow, K., Fisher, A., and Nava, S., 2007, Seismic and infrasound energy generation and propagation at local and regional distances: Phase 1 – Divine Strake experiment, Paper presented at the 29th Monitoring Research Review, Denver, Co., 25 - 27 Sept.

Table 1. Characteristics of the infrasonic arrays installed in Utah

Characteristics	NOQ array	BGU array	EPU array
Number of elements	4	4	4
Sensor type	Chaparral 2	Chaparral 2	Chaparral 2.5
Digitizer	REF TEK 130	REF TEK 130	REF TEK 130
Real-time telemetry	Yes	Yes	Yes
Average distance between sensors (m)	118	115	119
Installation date	May 4, 2006	April 17, 2007	July 13, 2007
Co-located seismic station type	Broadband (BB)	Broadband (BB)	Short Period (SP)
Start date of the archived data	May 4, 2006 IRIS DMC	April 17, 2007 UUSS	July 13, 2007 UUSS

Table 2. Distance, azimuth, and backazimuth values from the earthquake to one element of the infrasonic arrays.

Array	Dist (km)	Az (deg)	Baz (deg)
BGU	157	99	280
EPU	208	82	264
NOQ	238	103	284
NVIAR	422	225	43
PDIAR	472	66	250

Table 3. Amplitude measurements (in Pa) for the P, S, and epicentral infrasound

Array Amplitude	BGU	EPU	NOQ
P	0.44	0.25	0.64
S	0.89	0.63	1.16
Epicentral	0.48	1.59	1.87

Figure Captions

Figure 1.
Location map of the Wells epicenter (red star) and the five infrasonic arrays (yellow triangles) in Nevada (NVIAR), Utah (BGU, EPU, NOQ) and Wyoming (PDIAR). Also shown is the location polygon (red line) resulting from the grid-search location scheme implemented in InfraMonitor.

Figure 2.
Waveforms recorded at the five infrasonic arrays. Data were filtered between 1 and 5 Hz. Note the presence of the P and S groups (local infrasound), ground-air coupled infrasound between the source and receiver, and the epicentral infrasound time windows defined by red vertical lines.

Figure 3.

Comparison between the infrasound (blue) and seismic (red) waveforms recorded at BGU, EPU, and NOQ. The seismic stations BGU and NOQ have broadband instruments, and EPU is a short-period seismic station. The amplitude scales are different and the seismic signal at EPU is clipped. Seismic and infrasound data were band-pass filtered between 1 and 5 Hz. P and S waveforms for the main event and the aftershock that occurred at 14:21 are evident on the seismic records at BGU, NOQ, and EPU. The infrasound waveforms recorded at the infrasonic arrays exhibit more complex features (local and epicentral infrasound from the main event are observed for all the arrays). This figure was generated using GSAC, part of the Computer Programs in Seismology by R. B. Herrmann (http://www.eas.slu.edu/People/RBHerrmann/CPC330.html).

Figure 4.

Analysis of the infrasonic signals recorded at BGU array using Infra Tool. From top to bottom, the panels represent the correlation, the phase velocity, the azimuth, and the waveforms at one of the array elements. The vertical lines indicate detections of correlated waveforms.

Figure 5.

Beamforming results from PMCC for the signals at ~14:19 (top) and ~14:24 (bottom) recorded at the BGU array. The two signals are very similar and may represent acoustic energy from the main shock and the ~14:21 aftershock that resulted from coupling of the ground motion into the air in an area between the epicenter and the array.

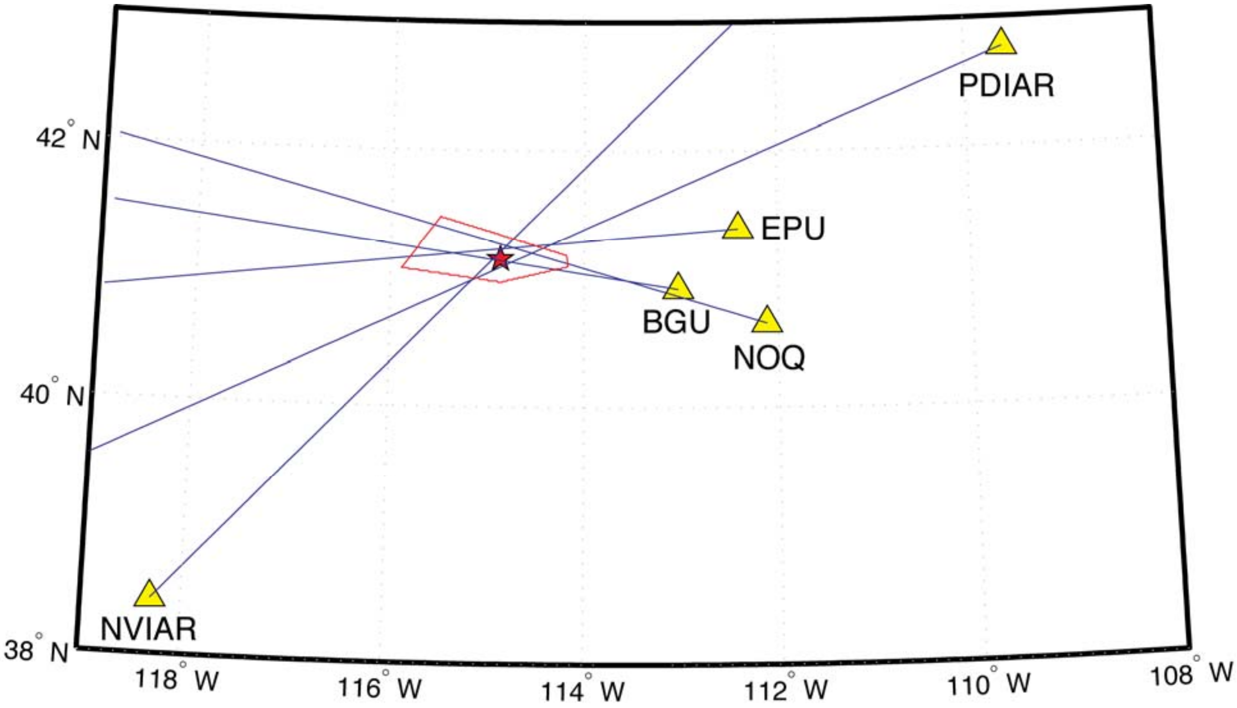
PDIAR
42° N
EPU
BGU
NOQ
40° N
NVIAR
38° N
118° W
116° W
114° W
112° W
110° W
108° W

Figure 1.

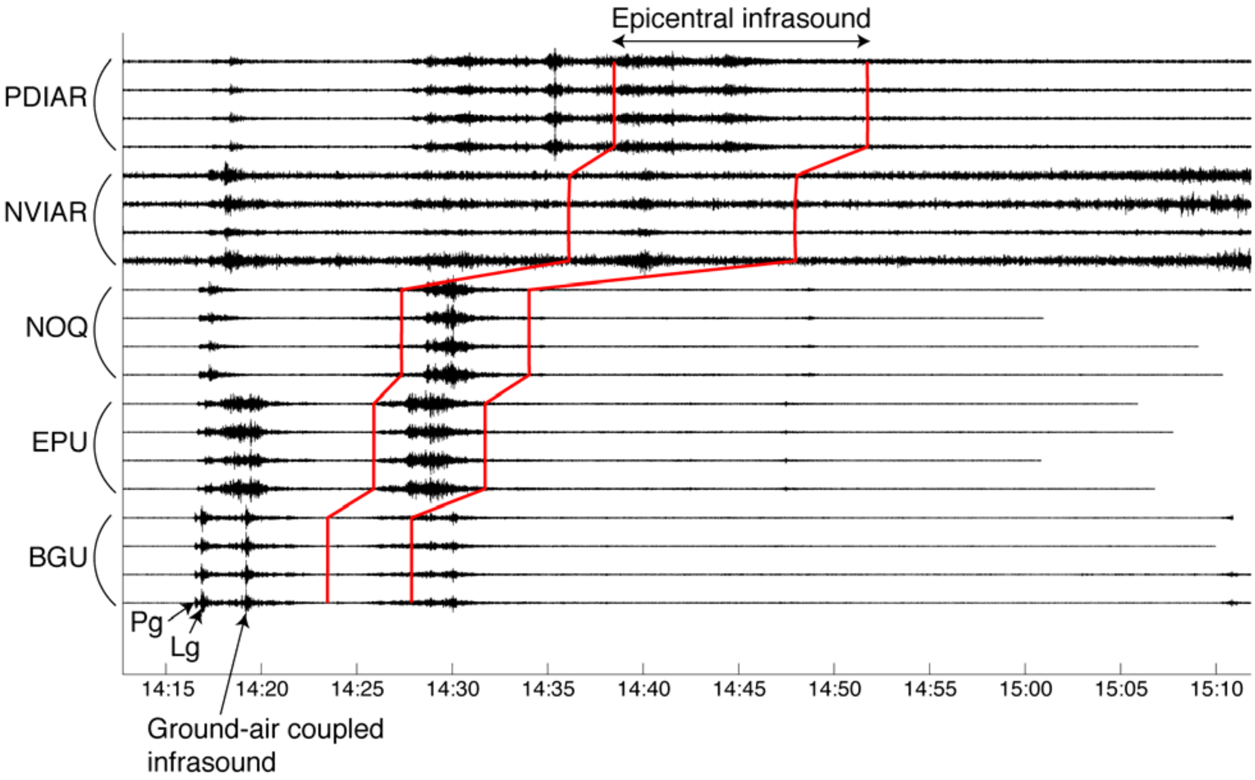
Epicentral infrasound
PDIAR
NVIAR
NOQ
EPU
BGU
Pg
Lg
Ground-air coupled infrasound
14:15
14:20
14:25
14:30
14:35
14:40
14:45
14:50
14:55
15:00
15:05
15:10

Figure 2.

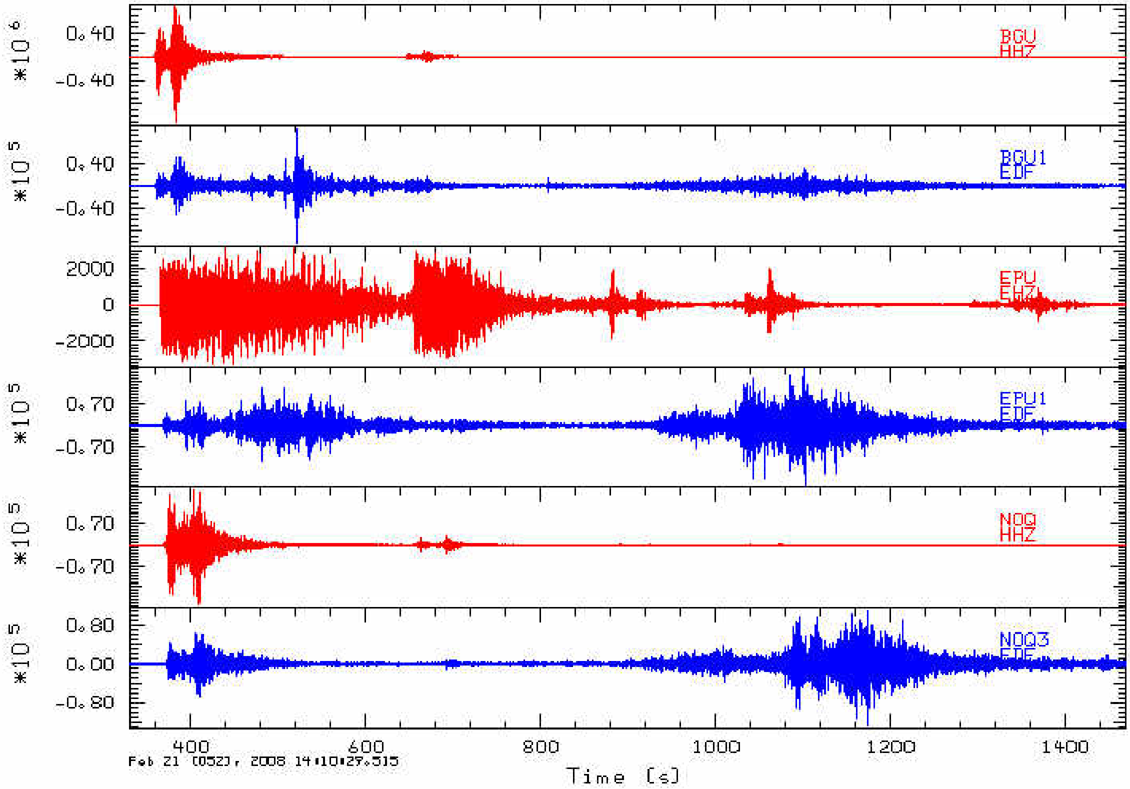
*10 6
0.40
-0.40
BGU
HHZ
*10 5
0.40
-0.40
BGU1
EDF
2000
0
-2000
EPU
EHZ
*10 5
0.70
-0.70
EPU1
EDF
*10 5
0.70
-0.70
NOQ
HHZ
*10 5
0.80
0.00
-0.80
NOQ3
EDF
400
600
800
1000
1200
1400
Feb 21 (052), 2008 14:10:29.515
Time [s]

Figure 3.

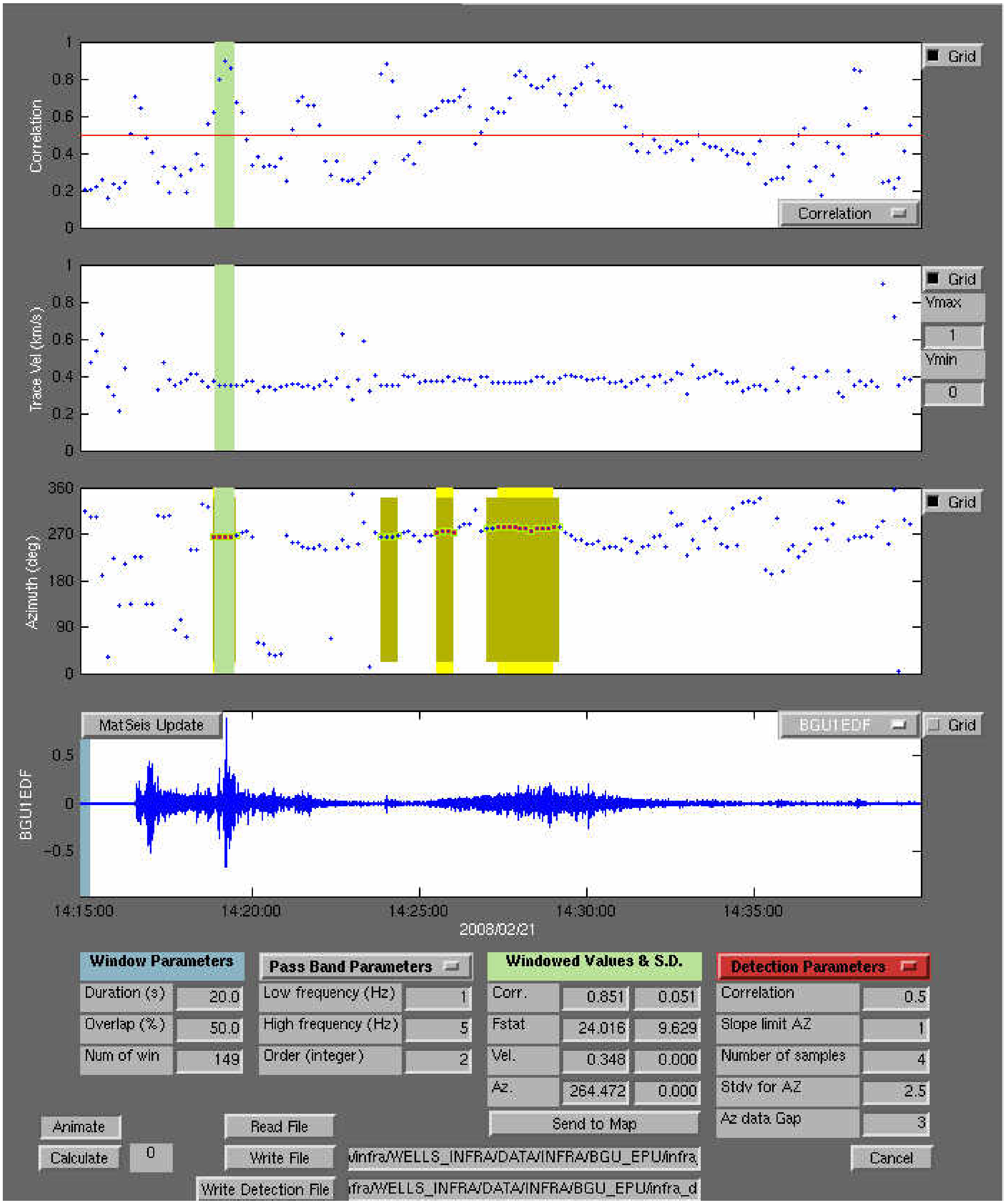

Window Parameters

Duration (s)	20.0
Overlap (%)	50.0
Num of win	149

Pass Band Parameters

Low frequency (Hz)	1
High frequency (Hz)	5
Order (integer)	2

Windowed Values & S.D.

Corr.	0.851	0.051
Fstat	24.016	9.629
Vel.	0.348	0.000
Az.	264.472	0.000

Detection Parameters

Correlation	0.5
Slope limit AZ	1
Number of samples	4
Stdv for AZ	2.5
Az data Gap	3

Ymax 1

Ymin 0

Calculate 0

Write File: /infra/WELLS_INFRA/DATA/INFRA/BGU_EPU/infra

Write Detection File: fra/WELLS_INFRA/DATA/INFRA/BGU_EPU/infra_d

Figure 4.

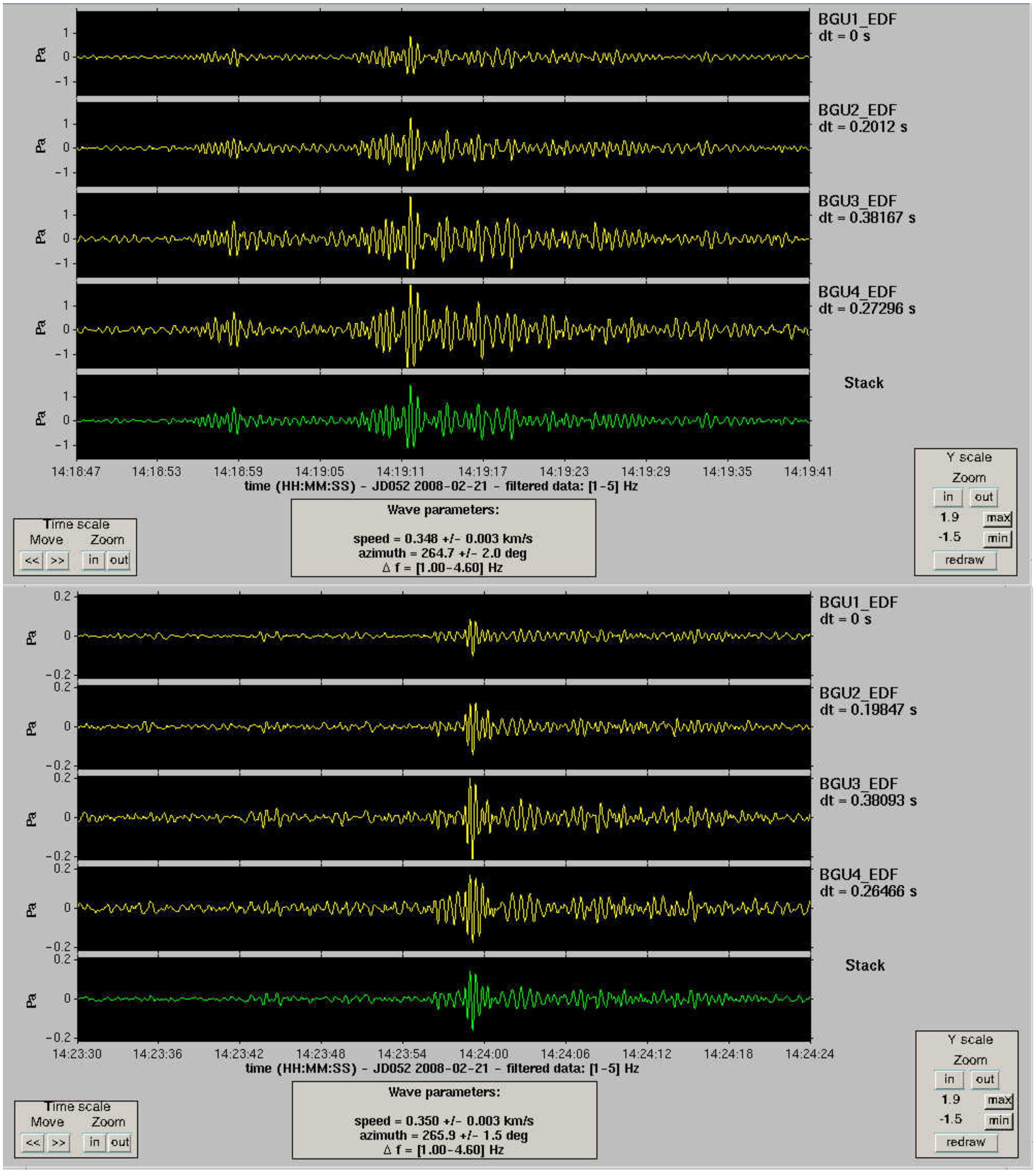

BGU1_EDF
dt = 0 s

BGU2_EDF
dt = 0.2012 s

BGU3_EDF
dt = 0.38167 s

BGU4_EDF
dt = 0.27296 s

Stack

time (HH:MM:SS) - JD052 2008-02-21 - filtered data: [1-5] Hz

Wave parameters:

speed = 0.348 +/- 0.003 km/s
azimuth = 264.7 +/- 2.0 deg
Δ f = [1.00-4.60] Hz

BGU1_EDF
dt = 0 s

BGU2_EDF
dt = 0.19847 s

BGU3_EDF
dt = 0.38093 s

BGU4_EDF
dt = 0.26466 s

Stack

time (HH:MM:SS) - JD052 2008-02-21 - filtered data: [1-5] Hz

Wave parameters:

speed = 0.350 +/- 0.003 km/s
azimuth = 265.9 +/- 1.5 deg
Δ f = [1.00-4.60] Hz

Figure 5.

CHAPTER 4

Seismo-Acoustic Observations from an Experiment in Northern Utah

Relu Burlacu[1], Tae Sung Kim[2], Brian Stump[2], Kristine Pankow[1], Chris Hayward[2], Sue Nava[3], Jessie Bonner[4], Sebastian Hoch[1], David Whiteman[1], Aileen Fisher[2], Ray Kubacki[2], Mark Leidig[4], James Britton[4], Dave Drobeck[1], Pete O'Neill[1], Kevin Jensen[1], Ken Whipp[1], Gordon Johanson[1], Paul Roberson[1], Ray Read[3], Ronald Brogan[3], and Steve Masters[3]

University of Utah[1]
Department of Earth Sciences, Southern Methodist University[2]
ENSCO, Inc.[3]
Weston Geophysical Corporation[4]

To be submitted **Seismological Research Letters**

INTRODUCTION

In the summer of 2007 a consortium comprised of universities—University of Utah (UU) and Southern Methodist University (SMU)—and industry—ENSCO and Weston Geophysical—designed and carried out an experiment in northern Utah (Figure 1). The main purpose of the experiment was to measure seismo-acoustic signals associated with the rocket motor detonations that take place quite frequently at the Utah Test and Training Range (UTTR) of the Hill Air Force Base (AFB). Seismic and acoustic equipment from PASSCAL and SMU was deployed from ~200 m to more than 200 km distance from the place where the detonations occurred. In addition to three infrasound arrays already installed in Utah, three infrasound arrays of five elements each and eleven single infrasound stations (and three additional near-source high pressure gauges) were collocated with existing seismic stations that are part of the regional seismic network operated by the University of Utah Seismograph Stations (UUSS) and the National Science Foundation (NFS) EarthScope Transportable Array (TA) network. The distribution of stations and the source location are presented in Figure 1. During the experiment, which covered four weeks of continuous on-site recording, data from four detonations were recorded. The detonations occurred on August 1, August 6, August 13, and August 27, 2010, respectively. The four events had seismic duration magnitudes between 1.8 and 2.0, calculated using the UUSS procedure described in Pechmann et al., 2007.

Although we recorded many other events during the four-week period, we present here preliminary results related to the four rocket motor detonations, emphasizing different observational aspects of the seismic and acoustic propagation from local to near-regional distances.

MOTIVATION

Although there is a resurgence of interest in seismo-acoustic observations from natural and manmade sources, there are still unanswered critical questions on the phenomenology surrounding the generation and local-to-regional distance propagation of seismic and low frequency acoustic energy from shallow sources (industrial and mining explosions, chemical test explosions, underground mine related stress release, and earthquakes) that impact the use of observations for source identification, location and characterization in areas with little ground truth. While there have been extensive seismic and acoustic observations of shallow sources (Dighe *et al.,* 1998; McKenna, 2005; Mutschlecner and Whitaker, 2005; Patton *et al.,* 2003; ReVelle *et al.,* 2004; Yang *et al.,* 1999) these have been limited in most cases to a moderate number of short-term stations for a single group of events or have focused on signals from one location into one possibly augmented array. Therefore, there is a need to extend the previous observational and theoretical studies using dense networks of collocated seismic and infrasound sensors that record signals from a wide variety of sources at local and regional distances. The acquisition of a dense number of observations along one or more profiles that characterize the wavefield transition from local to regional distances is a critical component needed to understand seismic and infrasound propagation. In addition, when available, ground truth information provides source constraints that are necessary for unique interpretations of the observational data.

Aside from the detonations that take place at UTTR, Utah is an ideal region for recording and investigating seismo-acoustic signals generated by a variety of sources like earthquakes, quarry blasts, mining induced events, etc. By coordinating the deployment of infrasound sensors with existing seismic stations, we were able to optimize resources, removing the need for deployment of additional seismic stations while maintaining the capability to use both seismic and infrasound recordings in source and propagation path assessment.

In order to understand seismic and infrasound propagation we rely on the acquisition along one or more profiles to characterize the wavefield transition from local to regional. A controlled experiment provides the opportunity to gather atmospheric profiles to help with interpretation of the resulting observations.

Another important aspect to take into account is the fact that the UTTR detonations take place at the same location and the source characteristics are repeatable, allowing us to study the propagation effects in varying atmospheric conditions.

THE EXPERIMENT

The experiment was motivated, in part, by seismo-acoustic signals recorded in Utah, starting in May 2006, when SMU and UUSS installed the first infrasound array in Utah, collocated with the seismic station NOQ (see Figure 1). The array, with an aperture of ~150 m, consists of four sensors digitized at 100 Hz and telemetred to the central location at UU, in Salt Lake City. For more than 2 years, the infrasound array NOQ recorded events from around Utah. Two categories of events were quarry blasts at Bingham copper mine and rocket motor detonations at UTTR. These types of events had been recorded by University of Utah’s regional seismic network for a long time, due to the presence of seismic stations in these areas. Each of these sources are repeatable and present an opportunity for recording and analyzing seismo-acoustic signals in order to characterize the wavefield from local to regional distances.

The opportunity to physically observe a UTTR detonation on June 4, 2007 (Figure 2 shows the detonation moment and the crater that resulted) motivated the consortium to organize a meeting in Salt Lake City to discuss the details of a plan for an experiment to recover a diverse set of seismo-acoustic records from planned future detonations. The recordings from the June 4 event and discussions with the UTTR personnel were important factors needed in the decision related to the number and distribution of stations, the field equipment, etc. The infrasound arrays BGU and NOQ recorded the detonation; examples of recordings from the June 4 event are presented in Figure 3 for BGU and Figure 4 for NOQ, respectively. Figures 3 and 4, also present noise and signal spectra of single elements of the arrays. At the time the temporary instruments were deployed in the field as part of the experiment, three infrasound arrays were already installed in Utah (collocated with the seismic stations NOQ, BGU, EPU). The experiment also included three temporary 5-element infrasound arrays collocated with seismic stations FSU, HVU, and WMUT and seven single infrasound sensors collocated with seismic stations HLJ, HONU, JLU, LDJ, NPI, RCJ, and SNUT that are part of the UU regional seismic network, four single infrasound sensors collocated with the TA seismic stations M12A, M13A, N12A, and P13A and three single infrasound sensors (collocated with seismic sensors) close to the detonation site.

The design of the experiment was driven by what the consortium considered important scientific goals for the study and included: (1) Collocation of the infrasound sensors with seismic stations in the area (operated by UUSS and EarthScope) to quantify the seismo-acoustic observations and cross coupling between the atmosphere and the solid earth; (2) Addition of 3 infrasonic arrays to the existing UUSS arrays in order to estimate the backazimuth and phase velocity of signals of interest that will be used to quantify infrasound propagation path effects and their temporal variation; (3) A distribution of infrasound sensors focusing on recordings at distances less than ~250 km ("zone of silence") with the goal to better understand propagation path effects in this distance range through the analysis of record sections and estimated group velocities for different recorded infrasonic phases; and (4) Measurement of atmospheric parameters (temperature, wind speed and direction) at the time of detonations and at multiple locations to help with developing and testing of the propagation models necessary to explain the characteristics of the observed infrasonic signals.

SOURCE DESCRIPTION AND SEISMO-ACOUSTIC OBSERVATIONS

At UTTR, rocket motors are destroyed using the open burn/open detonation (OB/OD) method. To avoid public complaints as a result of elevated noise levels and to comply with the regulatory noise limits, two semi-empirical sound models were developed, Blast Operation Overpressure Model (BOOM) and Sound Intensity Prediction System (SIPS) (McFarland et al., 2005). Both models are based on measured meteorological data. The decision to detonate at a particular day and time is based on the output from the two models. For the June 4, 2007 detonation, for example, the models based on the sound profile acquired at ~9 am, local time, suggested to postpone the detonation time, due to the presence of a slight inversion at lower altitudes. Later in the day, another balloon was launched and the new sound profile confirmed the favorable blasting conditions and the detonation occurred at 19:52 UTC. Figure 5 shows the sound velocity variation with altitude for four directions corresponding to paths to populated areas from the area of detonation corresponding to the first sound profile when the shot was delayed and the second one that was used to make the decision to detonate.

During the 4-week duration of the experiment, four detonations of Trident stage-1 missile motors were recorded by seismic and acoustic sensors. All four detonations had the same estimated yield, ~50,000 lb TNT equivalent.

Coordinating the deployment of infrasound sensors with existing seismic stations provides a leveraging of resources removing the need for deployment of seismic stations while retaining the capability to use both seismic and infrasound recordings in source and propagation path assessment. From the design stages of the experiment, an important part was to take advantage of the distribution of existing seismic stations (part of the UU regional seismic network and the USArray TA) by collocating infrasound sensors with seismic stations. The installation of six infrasound arrays and fourteen single infrasound sensors allowed us to develop record sections, both for seismic and infrasound signals (Figure 1 shows the station distribution along with shot and balloon launch locations). Record sections for the August 6, 2007 UTTR explosion are reproduced for the seismic (Figure 6) and for the infrasound stations (Figure 7). The seismic stations installed at UTTR, close to the detonation site, provided information on the time of the detonations;

we used this information to estimate group velocities from the record sections. As shown in Figure 7, for stations at distances up to ~100 km, the record section is dominated by energy traveling at estimated group velocity of ~350 m/s; this velocity is in agreement with the sound velocity that corresponds to the surface temperature measured at the time of the detonation. Velocities of ~300 m/s and ~280 m/s, estimated for the stations beyond 100 km distance, correspond to turning rays in the upper atmosphere. While the acoustic arrays were used to estimate the phase velocities and the backazimuths, data from singular acoustic sensors were very useful for creating the record sections that were critical to the wavefield interpretation.

The seismic record section of the August 6 detonation (Figure 6), spanning the same distance range as the infrasound observations, shows good signal-to-noise seismic observations across the range of distances. The acoustic to seismic coupled energy is also illustrated. The effects of both the direct infrasound waves at distances less than 100 km and turning rays at greater distances are observed.

SEISMIC AND ACOUSTIC AMPLITUDE CHARACTERISTICS

One interesting aspect of analyzing the data from the four detonations is the amplitude variation, from shot to shot. There are substantial differences in the amplitudes of the infrasound arrivals at common stations for the four detonations. In contrast, the seismic records at common stations show small amplitude variations, from shot to shot (Figure 8). From Figure 8 (left), which represents the waveforms from the four detonations recorded at the seismic station BGU at ~26 km from the detonation site and filtered in the 1-5 Hz range, it is apparent that the four shots exhibit (1) small amplitude variations and (2) coherent signals for the first 5 sec of the signals. In contrast, Figure 8 (right) shows significant amplitude variations and a lack of coherency of the waveforms recorded by one element of the infrasound array at BGU and filtered in the same 1-5 Hz range. For seismic signals, recorded at seismic station FSU at ~160 km, the comparison of waveforms and the P wave spectra from the four detonations shows very similar results (Figure 9).

Another interesting aspect of the acoustic amplitude analysis is its variation with range for the four detonations. (Figure 10) shows anomalies at distances of ~50 km and >150 km. To understand the acoustic amplitude characteristics at distances <100 km, using the atmospheric profiles recorded at UTTR and the Antelope Island, we made preliminary modeling efforts by applying the frequency-based two-dimensional Parabolic Equation (PE) model implemented in the InfraMAP software (Gibson and Norris, 2006) for the detonation on August 6, 2007. Amplitude attenuation results from the PE method show that the inversion layer between 1 and 2 km at azimuths 45° and 113° is responsible for the trapped energy at high frequencies (1 or 3 Hz) and explains the acoustic arrivals at short distance range (< 100 km), (Figure 11).

SPATIAL AND TEMPORAL VARIATION IN ATMOSPHERIC OBSERVATIONS

Quantification of atmospheric conditions at the time of detonation is a critical component of the experiment. As mentioned previously, the detonations at UTTR are preceded by launching atmospheric balloons to measure temperature and wind speed and direction. Temperature and wind data from the surface up to 30 km altitude are essential in quantifying possible effects on infrasound propagation in the “zone of silence”.

To account for possible variations of the atmospheric observations, in space and time, twelve balloon launches were completed at the Antelope Island (Figure 12) along the infrasound propagation path during the monitoring period. The times of these launches were planned to coordinate with the UTTR meteorological measurements and with the detonation times (the first launch was in the morning and the second in the afternoon at the shot time). It is also important to note that meteorological measurements are taken twice a day at the Salt Lake City airport. When comparing meteorological data recorded at the detonation site (UTTR) with those recorded at the Antelope Island we observed, in general, that temperature variation is relatively small compared to wind effects.

CONCLUSIONS

During the summer of 2007, an experimental plan was developed for deploying seismic and infrasound gauges to record UTTR near-surface explosions over a 4-week time period. A total of six infrasound arrays, three close-in infrasound and seismic stations and eleven single infrasound sensors collocated with existing seismometers were deployed. During this time interval, seismic and infrasound signals from four UTTR detonations were recorded. Preliminary data observations and analysis indicate that the sources were documented from within several hundred meters out to distances of 250 km. The distribution of infrasound sensors focusing on recordings at distances corresponding to the “zone of silence” allowed a better understanding of propagation path effects in this distance range through the analysis of record sections and estimated group velocities for different recorded infrasonic phases. Balloon launches before and at the time of the explosions were used to characterize the shallow atmosphere. This study suggests that short-term variations in the troposphere may greatly affect not only the amplitude but also the wave characteristics in the “zone of silence”.

Infrasound record sections suggest that guided waves along the ground-air interface are observed to distances as great as 100 km, with turning rays in the atmosphere at greater distances. Strong variations in infrasound signals from the four identical explosions are observed while there is little variation in seismic observations. The variability of these signals and the ability to make infrasound observations on some of the seismic stations has motivated a preliminary modeling study (Chapter 5, this report). The seismic record sections indicate the presence of acoustic phases related to acoustic to seismic coupling effects. These observations suggest the possibility, with proper calibration, of using seismic stations as proxy for recording acoustic signals in areas where infrasound sensors are not present. Another observation of the characteristics of the seismic signals from the four detonations is the consistency of seismic observations for repeated sources, both in time and frequency domains.

Although, in general, seismic signals are being used to characterize sources and propagation paths through the solid earth and infrasound signals are used for sources and paths through the atmosphere, this study shows the complementary nature of the two types of observations in jointly characterizing signals, noise, sources and propagation paths in the two media.

ACKNOWLEDGMENTS

Instruments for the planned portable deployment described in Figure 1 are being provided by PASSCAL. Contract FA8718-05-C-0020, Air Force Research Laboratory, has supported the array deployments at NOQ, BGU and EPU separately. The August 2007 deployment was supported under contract FA8718-06-C-0028 (Stump et *al.* 2007). The deployment of infrasound gauges at sites M13A, M14A, N12A and P13A were supported by EarthScope and thus NSF and in particular with the help of Bob Busby. Help from the UTTR personnel allowing the consortium members to observe on-site the June 4, 2007 detonation and to install instruments in the proximity of the detonation site is greatly acknowledged.

REFERENCES

Dighe, K., R. Whitaker, W. Armstrong (1998). Modeling Study of Infrasonic Detection of a 1 kt Atmospheric Blast. *20th Annual Seismic Research Symposium on Monitoring.* Santa Fe, New Mexico

Gibson, R. and D. Norris (2006). *User's Guide for InfraMAP, Version 5.1*. DTRA01-01-C-0084.

McFarland, M.J, J.W. Watkins, M.M Kordich, D.A. Pollet, G.R. Palmer (2004). Use of Noise Attenuation Modeling in Managing Missile Motor Detonation Activities, J. Air and Waste Manag. Assoc., 342–351.

McKenna, M. H. (2005). Infrasound wave propagation over near-regional and tele-infrasonic distances, Ph. D thesis at Southern Methodist University.

Mutschlecner, J.-P., and R.W. Whitaker (2005). Infrasound from earthquakes, J. Geophys. Res., 110, doi:10.1029/2004JF005067.

Patton, H.J., J. L. Bonner, and I. Gupta (2003). Modeling a CLVD + Monopole Explosion Source For the Shagan Depth of Burial Explosions. Poster Presentation at the *25th Annual Seismic Research Review on Nuclear Monitoring Technologies, Tucson, AZ.*

Pechmann, J. C., S. J. Nava, F. M. Terra, and J. C. Bernier (2007). Local magnitude determinations for Intermountain Seismic Belt earthquakes from broadband digital data, Bull. Seism. Soc. Am. 97, 557-574.

ReVelle, D., R.W. Whitaker, J.-P. Mutschlecner, and M.D. Renwald (2004). Discrimination of Earthquakes and Mining Blasts using Infrasound, Paper presented at the 26th Seismic Research Review, Orlando, FL, 21-23 Sept.

Stump, B., R. Burlacu, C. Hayward, K. Pankow, S. Nava, J. Bonner, S. Hoch, D. Whiteman, A. Fisher, T. S. Kim, R. Kubacki, M. Leidig, J. Britton, D. Drobeck, P. O'Neill, K. Jensen, K. Whipp, G. Johanson, P. Roberson, R. Read, R. Brogan and S. Masters, 2007, Seismic and Infrasound Energy Generation and Propagation at Local and Regional Distances: Phase I-Divine Strake Experiment, Air Force Research Laboratories report AFRL-RV-HA-TR-2007-1188, 11 October 2007, Hanscom AFB, MA 01731-3010.

Yang, X., B. W. Stump and D. C. Pearson (1999). Moment tensor inversion of single-hole mining cast blasts, *Geophys. J. Int.*, **139**, 679-690.

FIGURE CAPTIONS

Figure 1. Seismo-acoustic stations in Utah including those deployed for the 2007 experiment. Yellow star is UTTR, the detonation site. Solid black diamonds are permanent infrasound arrays, red diamonds are temporary infrasound arrays, and red circles are locations of single infrasound gauges. Sites where sound profiles were acquired are represented by green circles.

Figure 2. Moment of the June 4, 2007 detonation captured on camera (left) and the crater that resulted from the detonation (right).

Figure 3. Waveforms from the June 4, 2007 detonation recorded at acoustic array BGU (left) and the corresponding noise, plotted as a dashed line, and signal spectra (right).

Figure 4. Waveforms from the June 4, 2007 detonation recorded at acoustic array NOQ (left) and the corresponding noise and signal spectra (right). As in Figure 3, the noise spectrum is plotted as a dashed line.

Figure 5. Two sound profiles plotted for four directions corresponding to populated areas east of the detonation site obtained on June 4, 2007 at the UTTR location. Computer models based on the sound profiles determined the decision to (a) postpone the detonation in the morning hours (first profile, on the left) and (b) to complete it later in the day based (second profile, on the right).

Figure 6. Seismic record section for the August 6, 2007 UTTR explosion. Note the acoustic phases present on the seismic traces as a results of acoustic to seismic coupling. The red, green, and blue lines represent group velocities of 350, 300, and 280 m/s, respectively.

Figure 7. Acoustic record section for the August 6, 2007 UTTR explosion. Energy traveling at estimated group velocity of ~350 m/s, recorded at stations at <100 km, corresponds to direct infrasound waves and for group velocities of ~300 m/s and ~280 m/s, for stations beyond 100 km, corresponds to turning rays in the upper atmosphere. The red, green, and blue lines represent group velocities of 350, 300, and 280 m/s, respectively.

Figure 8. Comparison of seismic and acoustic recordings at seismic station BGU and one element of the acoustic array that is collocated with the seismic station. Amplitude and coherent signals characterize the seismic traces, while there is a significant variability in amplitude of the acoustic signals.

Figure 9. Seismic waveforms and corresponding spectra at station FSU for the four detonations to illustrate the consistency in time and frequency domain, from shot to shot. Noise spectrum is plotted in gray.

Figure 10. Acoustic amplitude variation with range for the four detonations. Amplitude anomalies are observed at distances of ~50 km and >120 km, respectively.

Figure 11. Amplitude attenuation results from the PE method for three different directions using the sound speed profile based on the meteorological data recorded on August 6, 2007.

Figure 12. Example of balloon launches for atmospheric measurements at the Antelope Island to quantify the atmospheric conditions at the time of detonations.

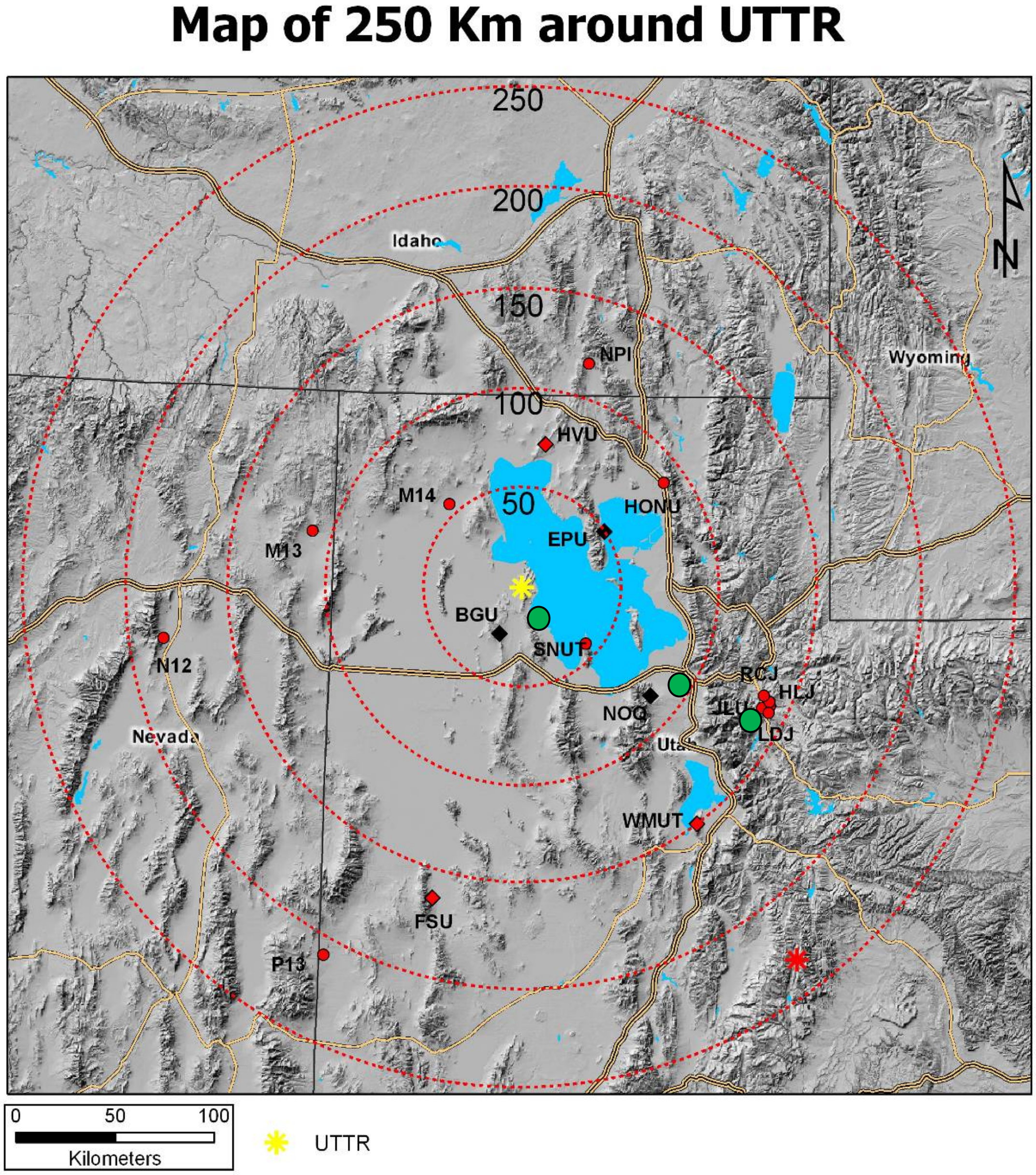
Map of 250 Km around UTTR
250
200
150
100
50
Idaho
Wyoming
Nevada
Uta
NPI
HVU
M14
HONU
EPU
M13
BGU
SNUT
N12
RCJ
HLJ
JLU
LDJ
NOQ
WMUT
FSU
P13
N
0
50
100
Kilometers
UTTR

Figure 1.

Figure 2.

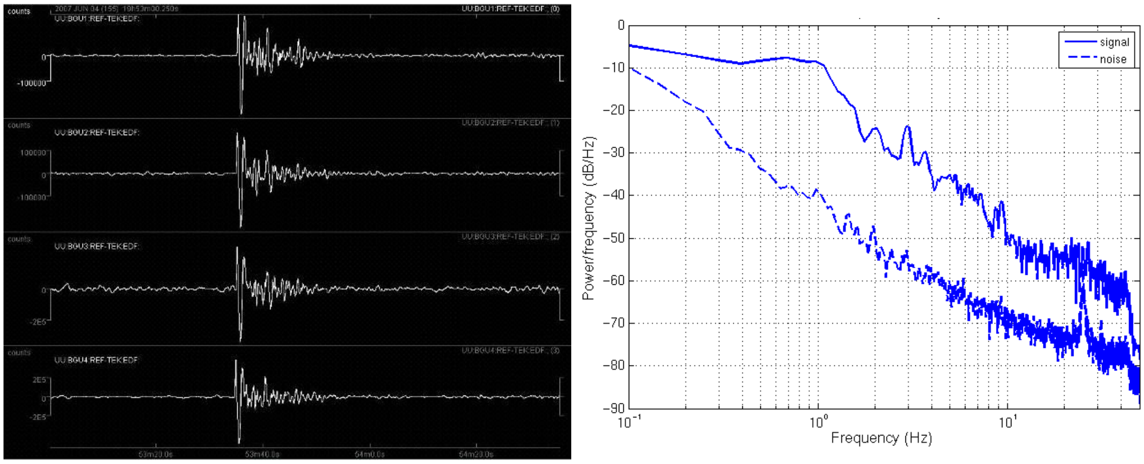
counts
2007 JUN 04 (155) 19h53m00.250s
UU:BGU1:REF-TEK:EDF: ; (0)
UU:BGU1:REF-TEK:EDF:
0
-100000
counts
UU:BGU2:REF-TEK:EDF: ; (1)
UU:BGU2:REF-TEK:EDF:
100000
0
-100000
counts
UU:BGU3:REF-TEK:EDF: ; (2)
UU:BGU3:REF-TEK:EDF:
0
-2E5
counts
UU:BGU4:REF-TEK:EDF: ; (3)
UU:BGU4:REF-TEK:EDF:
2E5
0
-2E5
53m20.0s
53m40.0s
54m0.0s
54m20.0s
signal
noise
Power/frequency (dB/Hz)
0
−10
−20
−30
−40
−50
−60
−70
−80
−90
10^{-1}
10^{0}
10^{1}
Frequency (Hz)

Figure 3.

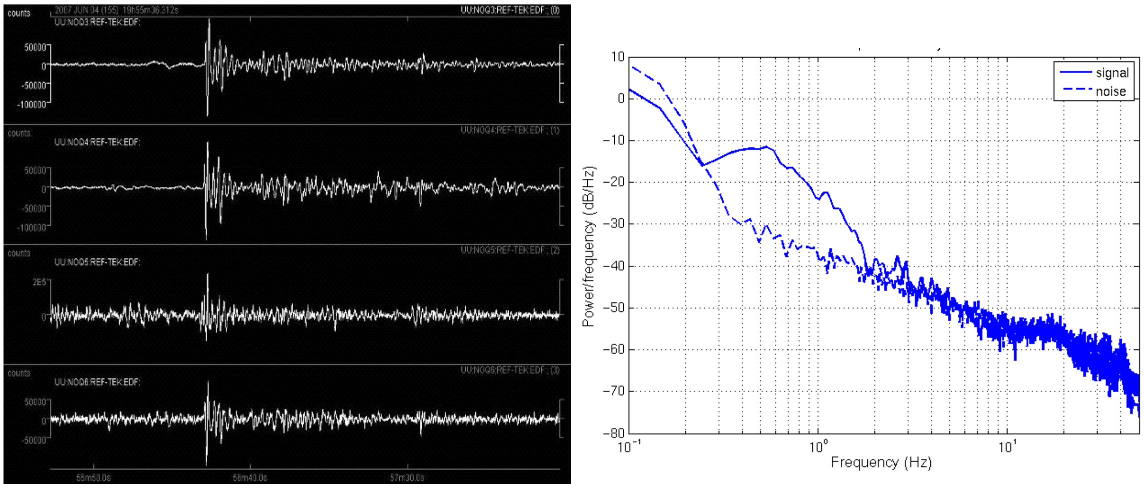
counts
2007 JUN 04 (155) 19h55m36.312s
UU:NOQ3:REF-TEK:EDF:; (0)
UU:NOQ3:REF-TEK:EDF:
50000
0
-50000
-100000
counts
UU:NOQ4:REF-TEK:EDF:; (1)
UU:NOQ4:REF-TEK:EDF:
50000
0
-50000
-100000
counts
UU:NOQ5:REF-TEK:EDF:; (2)
UU:NOQ5:REF-TEK:EDF:
2E5
0
counts
UU:NOQ6:REF-TEK:EDF:; (3)
UU:NOQ6:REF-TEK:EDF:
50000
0
-50000
55m50.0s
56m40.0s
57m30.0s
10
0
−10
−20
−30
−40
−50
−60
−70
−80
Power/frequency (dB/Hz)
10^{-1}
10^{0}
10^{1}
Frequency (Hz)
signal
noise

Figure 4.

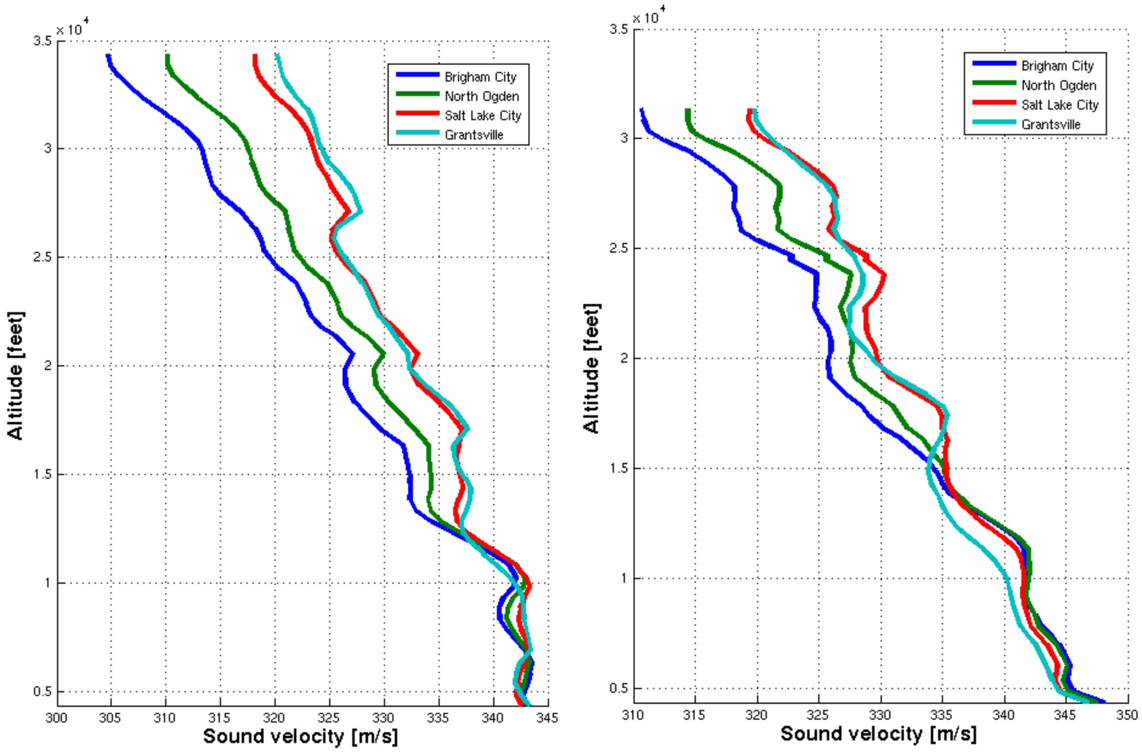
× 10^4
3.5
3
2.5
2
1.5
1
0.5
Altitude [feet]
300
305
310
315
320
325
330
335
340
345
Sound velocity [m/s]
Brigham City
North Ogden
Salt Lake City
Grantsville
× 10^4
3.5
3
2.5
2
1.5
1
0.5
Altitude [feet]
310
315
320
325
330
335
340
345
350
Sound velocity [m/s]
Brigham City
North Ogden
Salt Lake City
Grantsville

Figure 5.

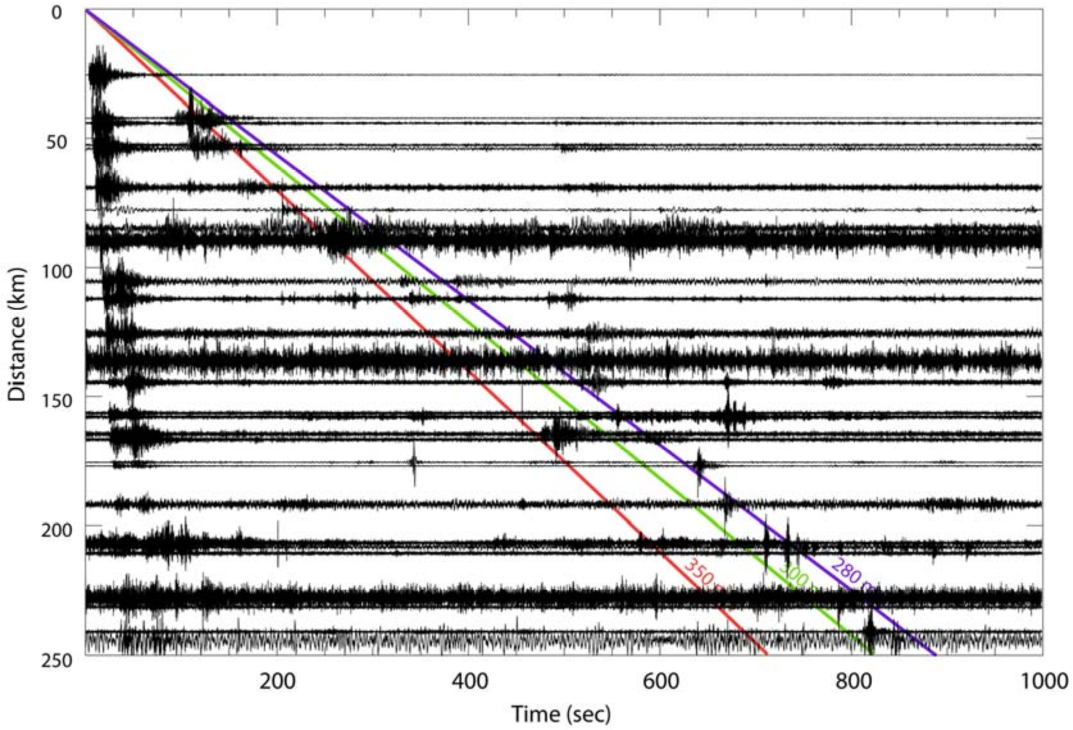

0
50
100
150
200
250
Distance (km)
200
400
600
800
1000
Time (sec)
350
300
280

Figure 6.

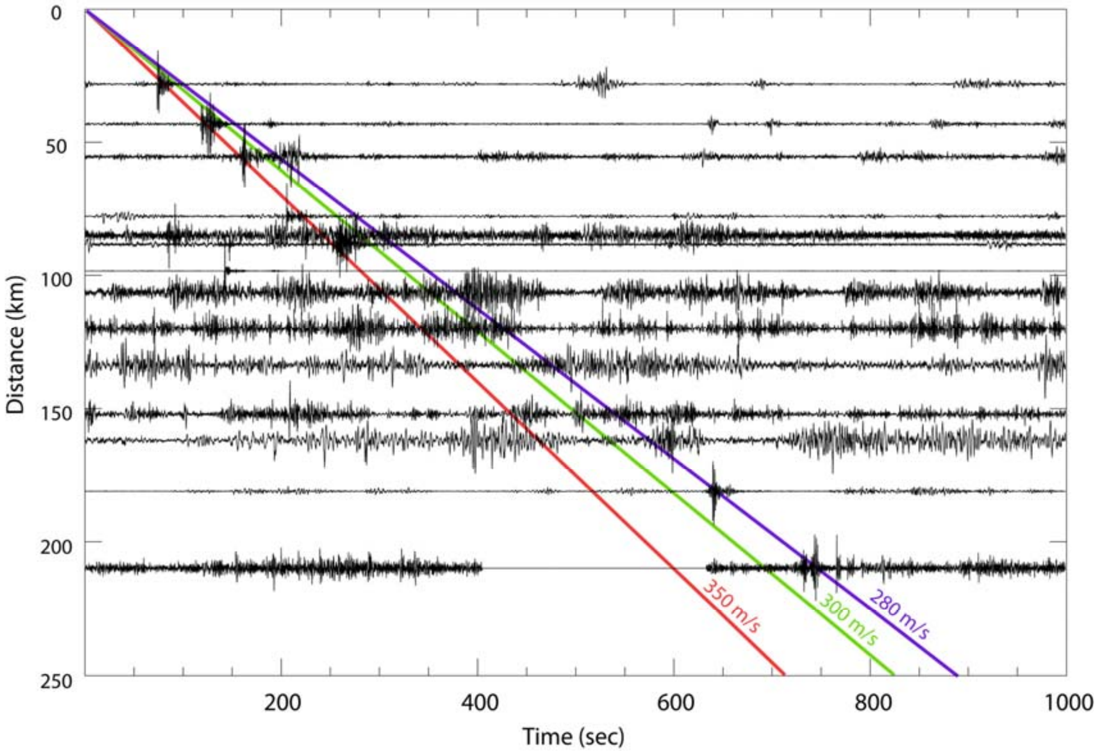
0
50
100
150
200
250
Distance (km)
200
400
600
800
1000
Time (sec)
350 m/s
300 m/s
280 m/s

Figure 7.

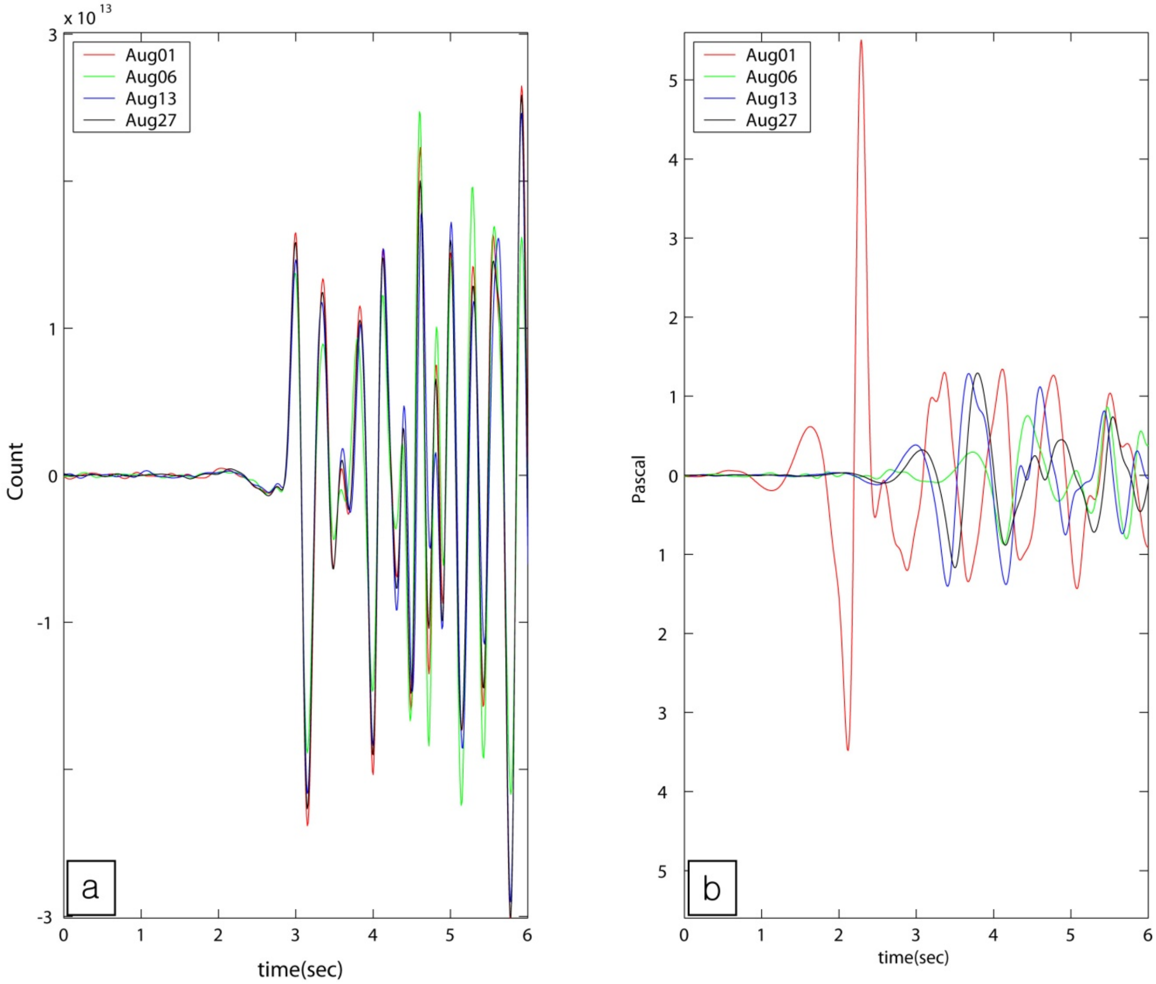
x 10 13
3
1
0
-1
-3
Count
Aug01
Aug06
Aug13
Aug27
a
0
1
2
3
4
5
6
time(sec)
5
4
3
2
1
0
1
2
3
4
5
Pascal
Aug01
Aug06
Aug13
Aug27
b
0
1
2
3
4
5
6
time(sec)

Figure 8.

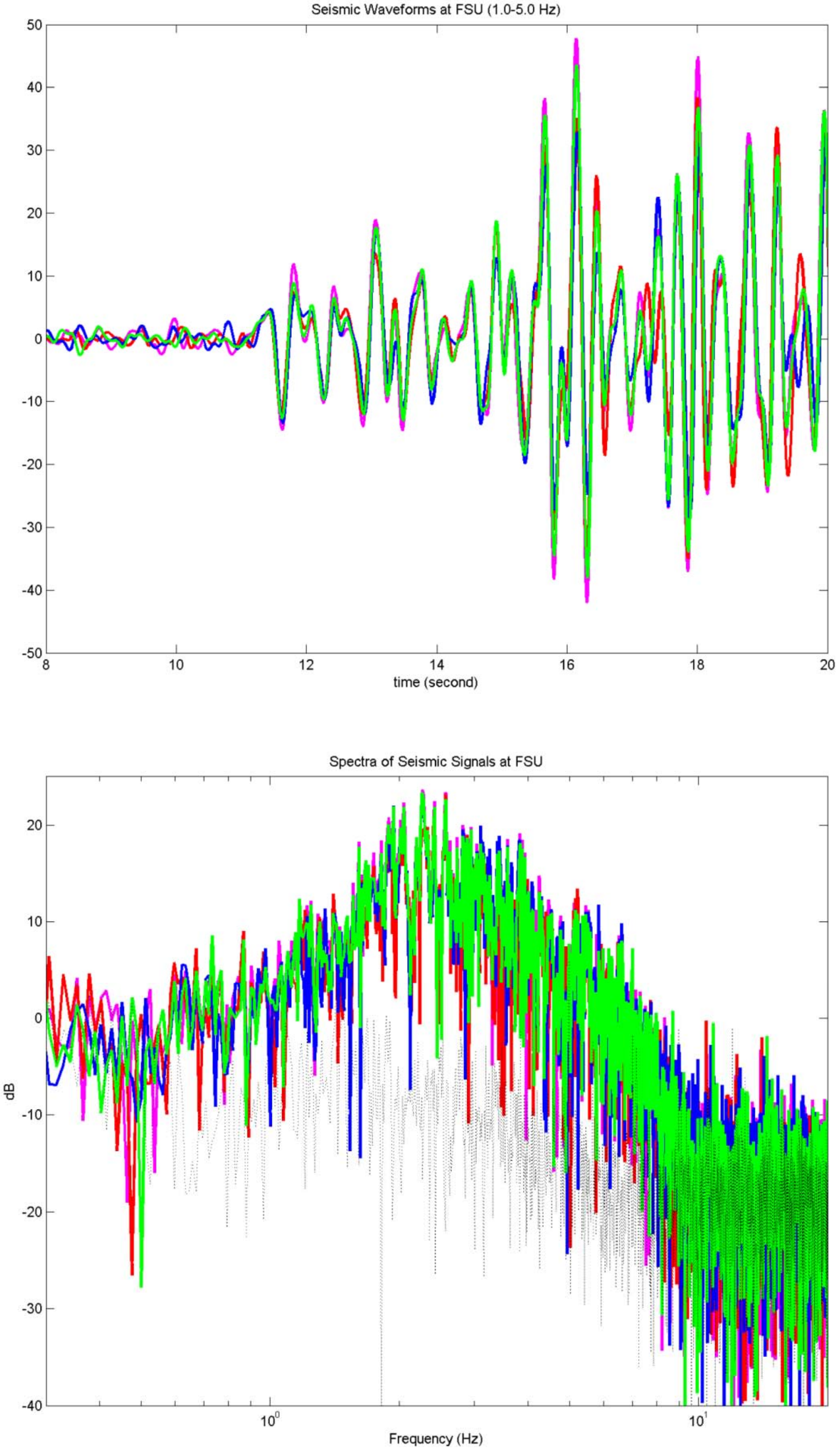
Seismic Waveforms at FSU (1.0-5.0 Hz)
50
40
30
20
10
0
-10
-20
-30
-40
-50
8
10
12
14
16
18
20
time (second)
Spectra of Seismic Signals at FSU
20
10
0
-10
-20
-30
-40
dB
10^0
10^1
Frequency (Hz)

Figure 9.

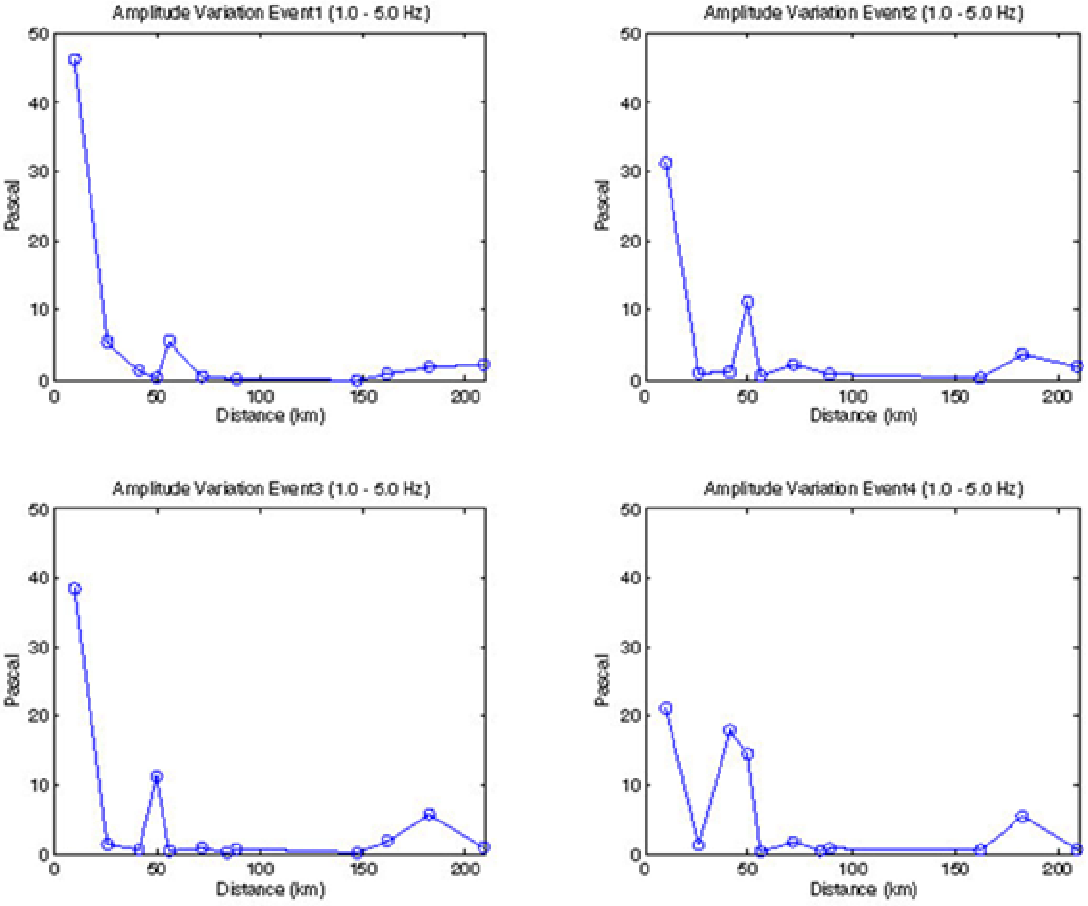

Amplitude Variation Event1 (1.0 - 5.0 Hz)

Amplitude Variation Event2 (1.0 - 5.0 Hz)

Amplitude Variation Event3 (1.0 - 5.0 Hz)

Amplitude Variation Event4 (1.0 - 5.0 Hz)

Figure 10.

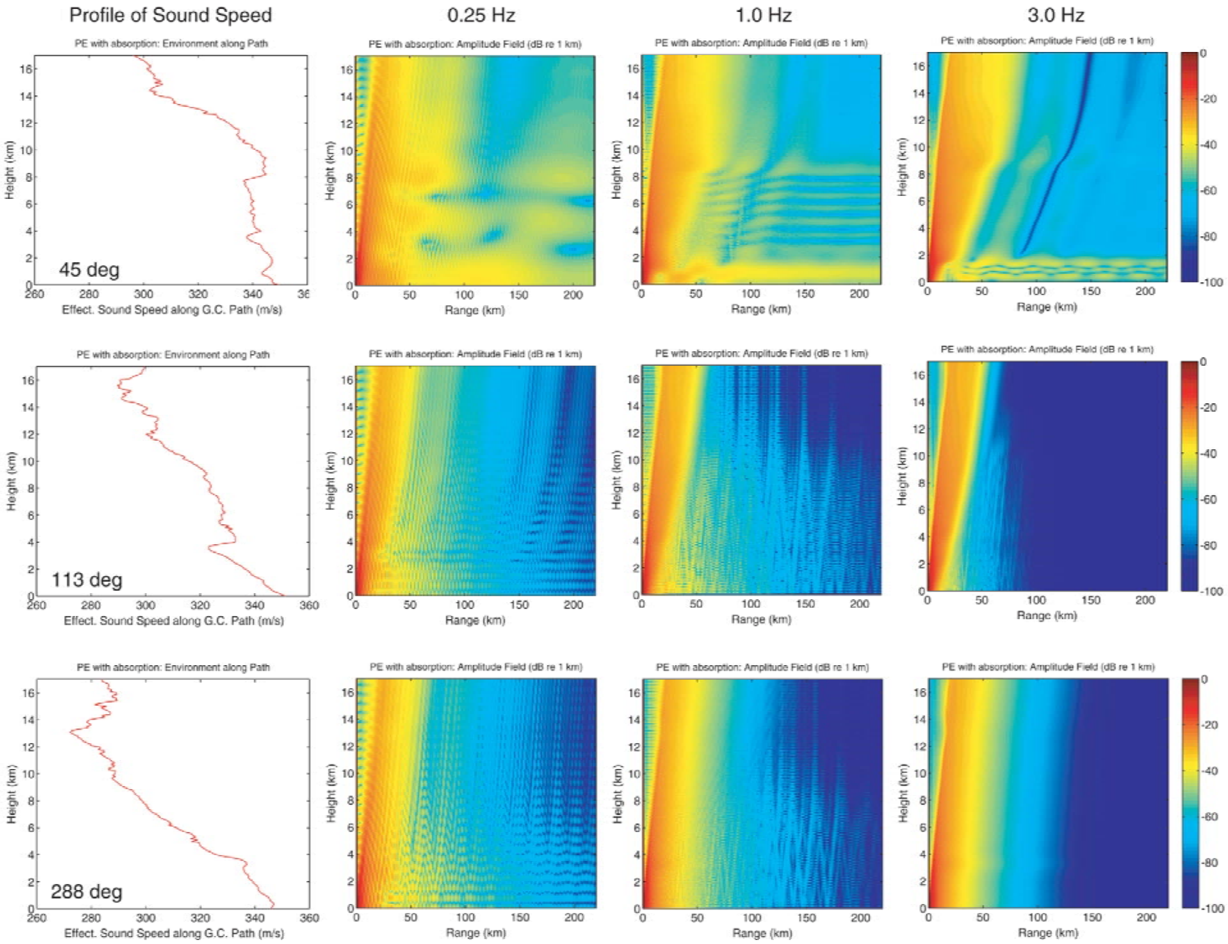
Profile of Sound Speed
0.25 Hz
1.0 Hz
3.0 Hz
PE with absorption: Environment along Path
PE with absorption: Amplitude Field (dB re 1 km)
Height (km)
Range (km)
Effect. Sound Speed along G.C. Path (m/s)
45 deg
113 deg
288 deg
0
2
4
6
8
10
12
14
16
260
280
300
320
340
360
50
100
150
200
0
-20
-40
-60
-80
-100

Figure 11.

Figure 12.

CHAPTER 5

Infrasound Observed and Modeled in the 1-210 km Range from Controlled Sources at UTTR

Tae Sung Kim[1], Brian W. Stump[2], Chris T. Hayward[2], Relu Burlacu[3] and Kristine Pankow[3]

Korea Institute of Geoscience and Mineral Resources[1], Southern Methodist University[2], University of Utah Seismograph Stations[3]

Abstract

Regular and repeated explosions detonated at the Utah Test and Training Range provided an opportunity for a controlled seismo-acoustic experiment in August 2007. During this time period, there were four identical explosions with an estimated explosive weight of 50,000 lbs. each. These detonations provided the opportunity to deploy a large number of infrasound gauges (11 single gauge stations and 3, near-source high pressure gauges) and six, four and five-element arrays for purposes of characterizing the infrasonic wavefield from ~ 200 m to 210 km. All infrasound sites were collocated with existing seismometers. This range of distances was chosen in order to investigate the characteristics of infrasonic wave propagation through the so-called “zone of silence.” A second goal of the work was to quantify the temporal and spatial variability of the atmosphere and its effect on the infrasonic observations. Balloons with radiosondes were launched from three locations, one at the explosion site, and used to quantify the shallow atmosphere to heights as great as 25 km. Infrasound observations show significant variability in arrival times and amplitudes from shot to shot while the seismic observations at a single station were nearly identical documenting the strong effect of atmospheric conditions on infrasonic wave propagation. Despite this variability, a number of consistencies in the infrasonic characteristics were identified and included: (1) infrasound arrivals from 100 m to 100 km composed of a sharp first arrival and followed by arrivals with a duration of 15 seconds and group velocity of 0.35 km/s; (2) No clear infrasound arrivals in the distance range from 100 to 140 km; and (3) Strong infrasound signals from all four explosions that arrive at regional distances from 140 to 210 km with group velocities from 0.28 to 0.3 km/second. The observed infrasound data at distances less than 100 km is consistent with geometrical spreading of r^{-1}. Multiple balloon launches before and after every shot at two of the sites provides a quantification of the spatial and temporal variability of the shallow atmosphere and identifies shallow wave propagation ducts along certain azimuths that correlate with the azimuths of observations. Observed azimuthal variations of group velocity at distances of less than 100 km are also consistent with the observed wind measurements. The atmospheric data was used in a ray tracing and parabolic equation modeling exercise. The ray tracing results support the shallow waveguide interpretation for the signals observed at distances of less than 100 km and suggest a possible focusing of energy near 50 km, consistent with the amplitude data. The PE models document azimuthal variation in signal strength because of winds that are qualitatively in agreement with the observations. The data, analysis and modeling at distance ranges of 0 to 100 km details the critical importance of real-time atmospheric data in data interpretation. Additional work is needed on the interpretation of the data to the farthest ranges.

Introduction

Infrasound observation in the shadow zone

Infrasound signals are low frequency acoustic waves ranging from 0.01 to 20 Hz. The arrival of these low frequency acoustic waves is not predicted at distances less than 250 km in the standard atmospheric model, a distance range called the “zone of silence” (Mckenna, 2005). Empirical studies, however, show that infrasound signals can be recorded in this “shadow zone” (Reed, 1969; Che et al., 2002; Pinsky et al. 2006; Evers et al., 2007). Reed, 1969, used acoustic signals created by Nevada atmospheric nuclear tests from 1951 to 1961 to quantify the relationship between climatological patterns and long-range infrasound propagations. He discussed the effects of tropospheric ducts and ionospheric returns on the propagation and amplitude magnification of infrasound signal at local and regional distances based on single station data. Che et al., (2002), showed that one seismo-acoustic array in the Republic of Korea recorded 67 infrasound arrivals from a rock quarry that was 49.6 km from the array. He modeled the infrasound arrivals using local meteorological data and concluded that local winds had a major effect on infrasound arrivals at short distance ranges and contributed to the variation of travel times observed. Pinsky et al., (2006), documented infrasound signals at distances of several tens of kilometers using four infrasound arrays. They showed refined relocation results using the grid search method. Evers et al., (2007), documented infrasound signals from the explosion of a high-pressure gas pipeline. The infrasound signals from this explosion were recorded on seismic and infrasonic networks at distances from 15 to 737 km. They used the infrasound data to constrain the origin time, location, and yield of the event.

Background of Experiment

Even though these earlier studies document infrasound signals recorded in the so-called “shadow zone”, the physics of infrasound propagation in this distance range is not well quantified due to the limited quality of ground truth, sparse station distribution, and the lack of realistic atmospheric profiles. An experiment conducted in Utah in August, 2007 provided the opportunity to overcome a number of these limitations (Stump *et al.,* 2007, Chapter 4 of this report). Large surface explosions (~50,000 lbs) were regularly performed at the Utah Test and Training Range (UTTR) of the Hill Air Force Base and provided the opportunity for a planned experiment to document the infrasonic wavefield produced from a number of these explosions. High quality ground truth (GT0) was produced approximately once a week at the UTTR source. During the period of data acquisition reported here, four rocket motors were detonated on the surface of the UTTR site (Table 1) and infrasound signals were recorded on single stations and arrays deployed at distances from ~200 m to 210 km. Atmospheric profiles at multiple sites were taken before and after the detonations to investigate the relationship between the infrasound propagation and the temporal and spatial variations of the atmosphere.

Table 1. Origin time, location and size of the detonations at UTTR

Origin Time (GMT)	Location	Size
08/01/2007 20:01:24.5	41.13152 -112.89577	50,000 lbs
08/06/2007 20:33:02.6		
08/13/2007 19:38:20.6		
08/27/2007 20:43:12.0		

In this paper we document the data and a modeling exercise designed to illustrate the phenomenology associated with infrasound generation and propagation in the shadow zone using the high quality ground truth.

Data Acquisition - Infrasound Stations and Atmospheric Profiles

Station Deployment

The experiment in Utah included a dense deployment of infrasound gauges consisting of six arrays and thirteen single stations at distances from ~200 meters to over 210 kilometers (Figure 1).

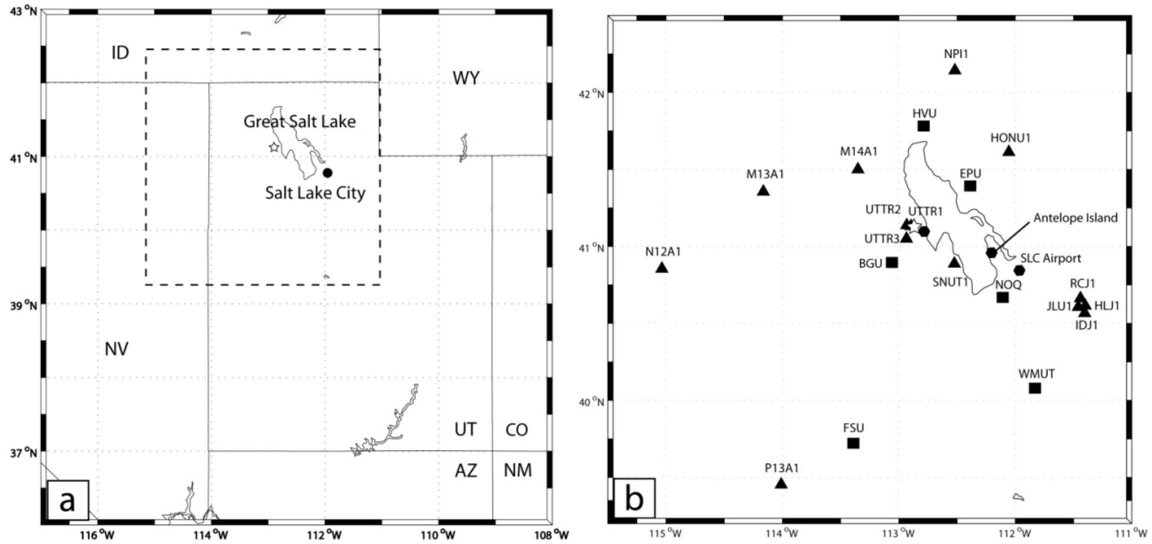

Figure 1. Study area around UTTR a) Seismic and acoustic sensors are installed within the box outlined by the broken line. b) The area within the broken line box. Black triangles represent single acoustic station. Black squares represent acoustic arrays. Black hexagons represent the sites where balloons were launched. White star is the source location at UTTR.

Three 100-m aperture arrays were composed of four-element acoustic gauges while the other three 200-m aperture box-type arrays were installed with five-element acoustic gauges (Figure 2). The types of acoustic gauges utilized in the experiment included the Chaparral 2.0, Chaparral 2.5, and Validyne P55D. Each acoustic sensor except the near-source stations - UTTR1, UTTR2, and UTTR3 - was connected to a 10-element flexible hose array (8 m hose length) to reduce the effect of uncorrelated wind noise. The data stream was digitized with RT-130 digitizers provided by PASSCAL. The sampling rate at the near-source stations UTTR1 and UTTR2 was 500 samples/second while other stations' sampling rate was 100 samples/second. Data was recorded in continuous mode for the one-month duration of the deployment.

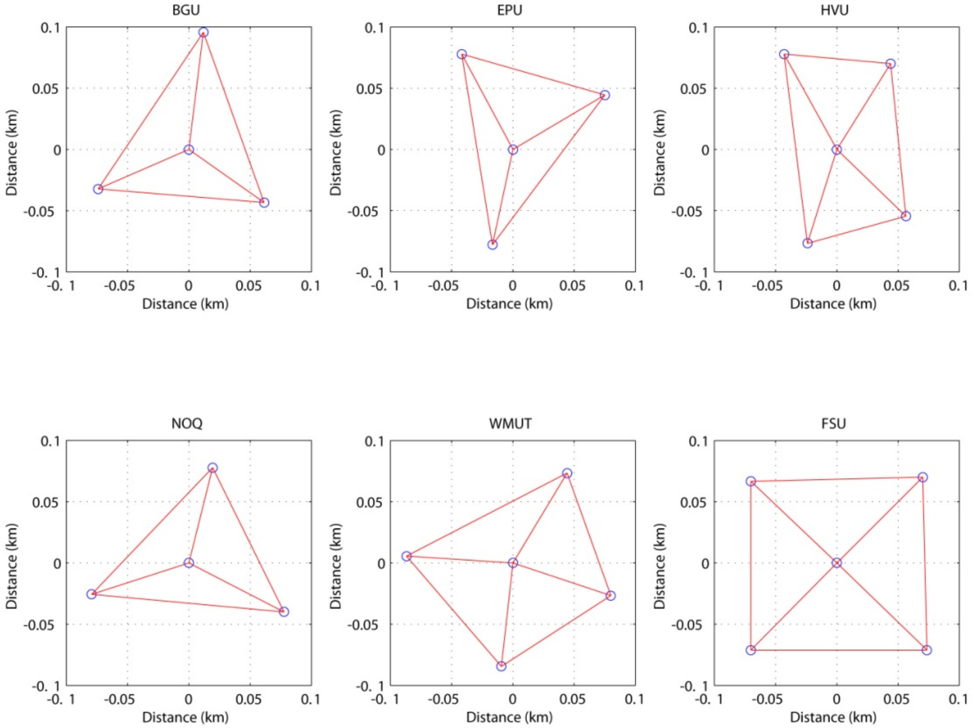

Figure 2. The geometry of six arrays deployed around UTTR

Atmospheric Profiling with Balloons

The atmospheric profile was sampled from the surface to a maximum height of 25 km using radiosondes launched at the UTTR source site, Antelope Island and Salt Lake City airport (Figure 3). At UTTR and Antelope Island, balloons were launched before and after the detonations while at the airport, the atmosphere was sampled every 12 hours: 0 GMT, 12 GMT. All the balloon launch sites are within 50 km of the source, which provided an opportunity to assess local variations in atmospheric conditions and use the empirical atmospheric structure for modeling infrasound propagation to local distances.

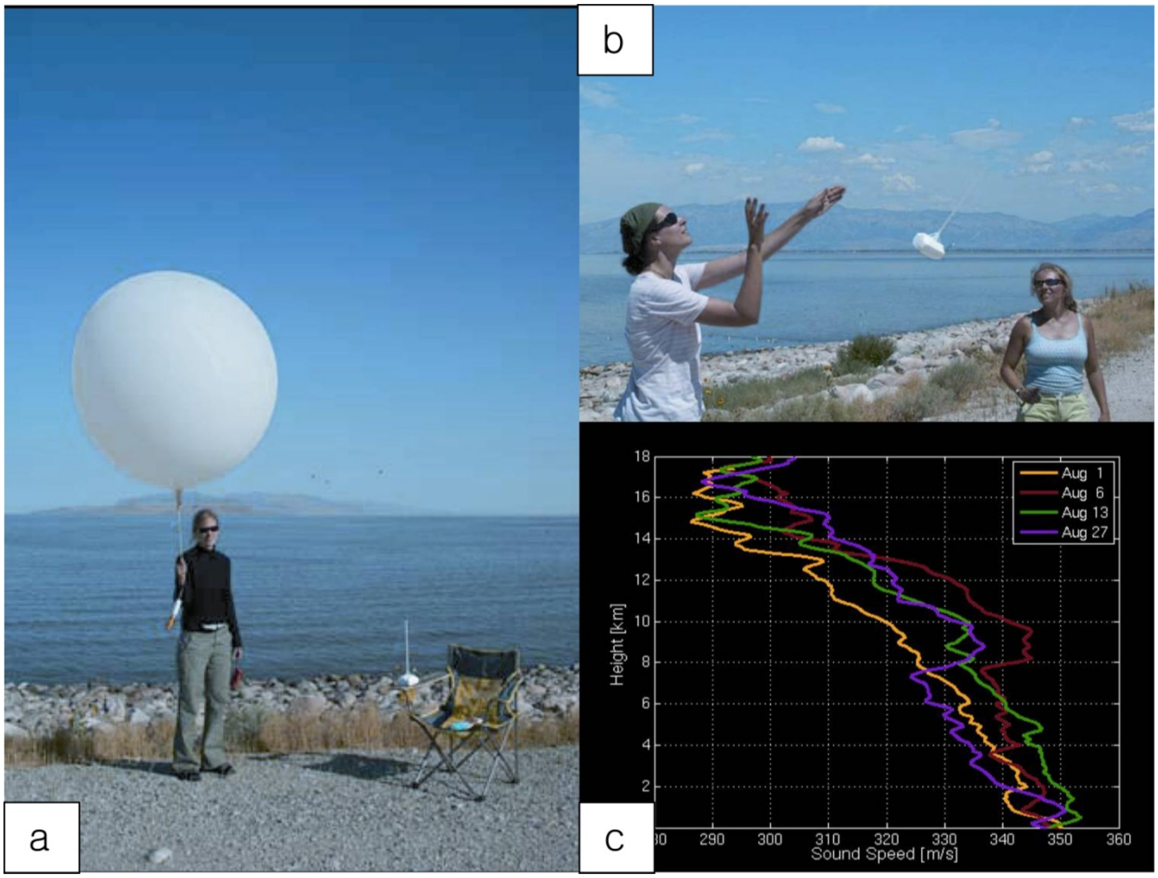

Figure 3. Pictures at the Antelope Island balloon launch site a) Inflated balloon ready for launch. b) Radiosonde attached to balloon. c) Four profiles of sound speed attained from radiosondes launched on the four days of the explosions.

Data and Analysis

The Utah seismic and infrasound network successfully recorded seismic and infrasound signals from four rocket motor detonations during the one-month duration of the experiment. Systematic analysis of the observed infrasound signal including travel time and amplitude variations were performed in this study.

Observed Seismic and Infrasound Signals

Infrasound Signals

Typical examples of seismo-acoustic signals recorded at the station FSU are illustrated in Figure 4. Clear seismic Pn, Pg and Lg phases were recorded at the existing seismic stations (Figure 4a) with group velocities ranging from 3 to 7 km/s while infrasound signals with relatively slower group velocity of around 0.28 km/s arrive later at the co-located infrasound array (Figure 4b). The infrasound energy was strong enough to generate air-to-ground coupling that is recorded at the seismic channel (Figure 4c). In this study, we focus on the analysis of the infrasound signals.

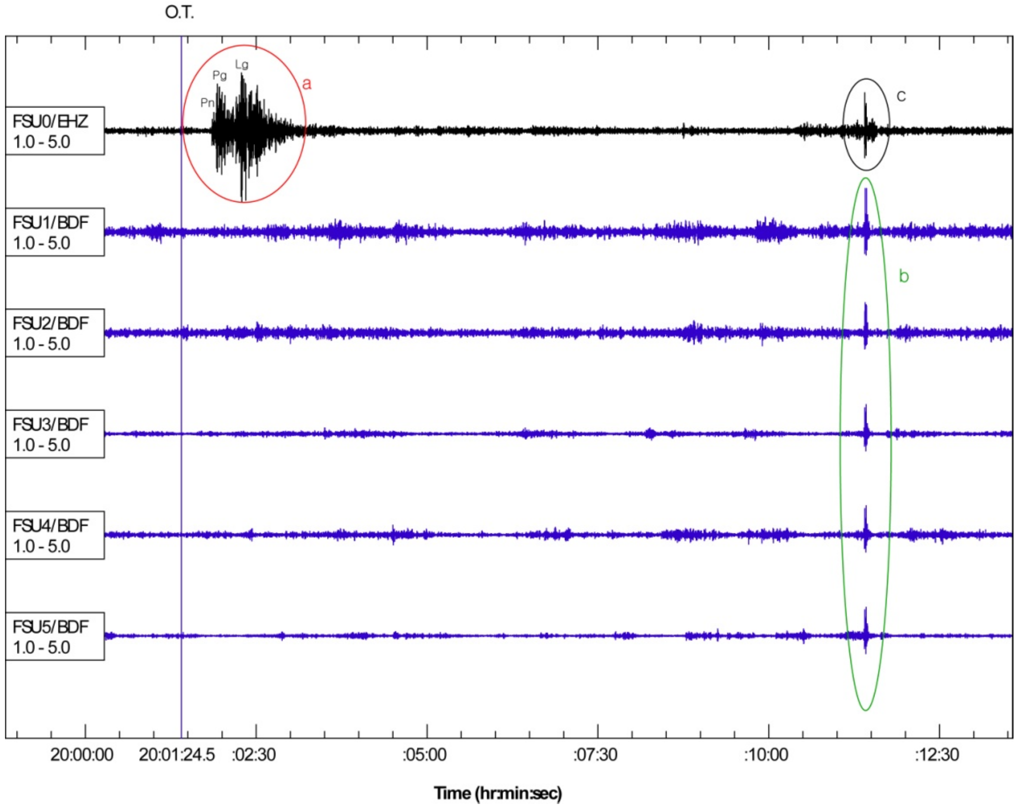

Figure 4. Seismo-acoustic signals (1.0 – 5.0 Hz) recorded at the array FSU a) Seismic phases b) infrasound signals recorded at the FSU c) Air-to-ground coupling recorded on the seismometer at FSU.

To assess the frequency content of infrasound signals, spectra of infrasound signals were estimated for eight infrasound stations. 20.48s time windows were tapered with a 10% cosine window to avoid the window effect and then transformed into the frequency to produce the spectral estimate. The signal spectra are compared to the spectrum of highest background acoustic noise (Figure 5) in order to document the bandwidth of the signals. The frequency content of the infrasound signals vary for different shots even though the location of the sources and stations remain the same as well as the sizes of the four sources.

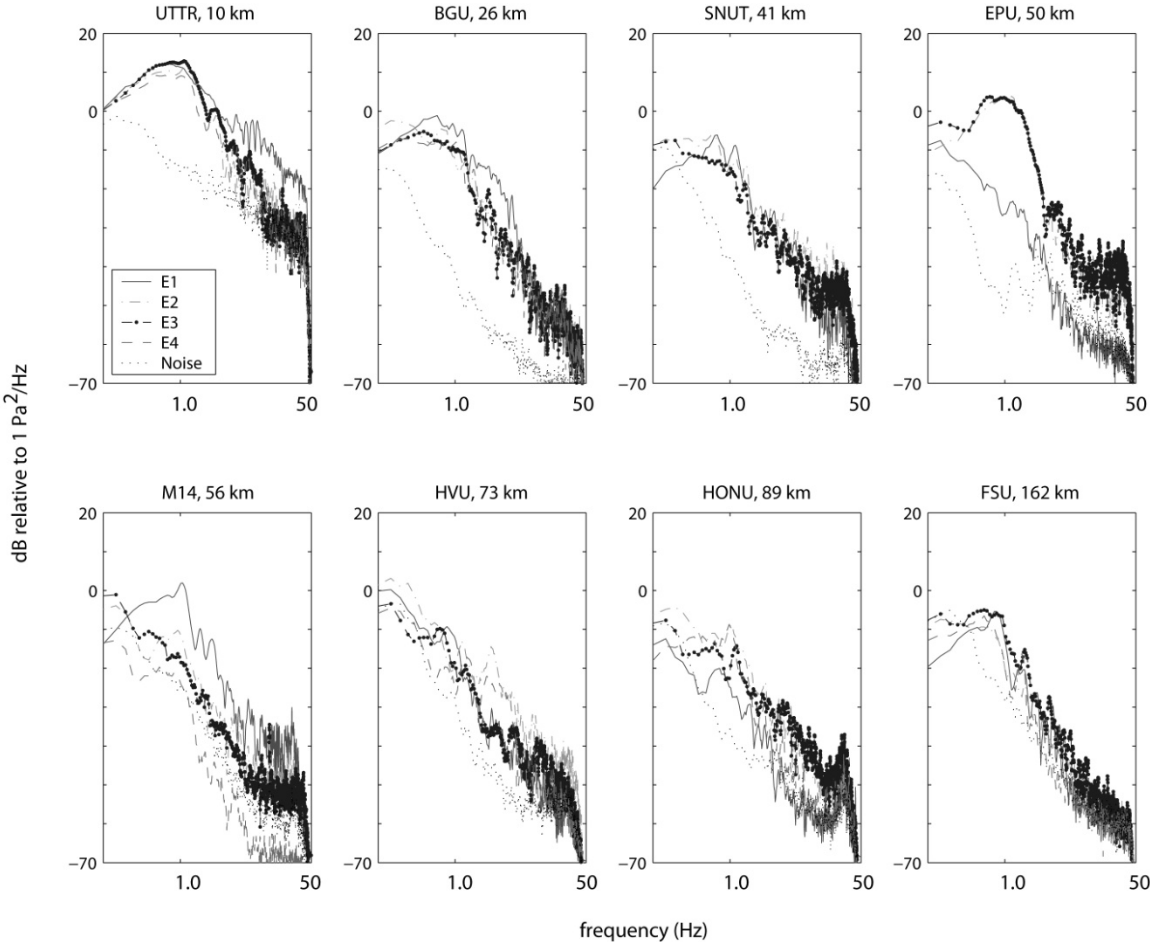

Figure 5. Comparison of signal and noise spectra for the four explosions at the eight infrasound stations. In each spectral plot, the spectrum with highest background noise is compared to the individual signal spectra.

For example, the infrasound signals recorded at station BGU (26 km) from the first detonation is enriched in frequencies from 3-10 Hz relative to the infrasound spectra from the other three detonations. The variations in frequency content of the infrasound signals can be observed in the time domain as well. The comparison of four seismic and infrasonic waveforms at BGU showed that waveforms of infrasound signals are quite different from each other while the seismic signals from the four explosions are identical (Figure 6). This comparison suggests that the time-varying atmospheric sound velocity structure can strongly affect both the waveform and frequency content of the infrasound signals since the source size, source location and station location are not changed for the different explosions.

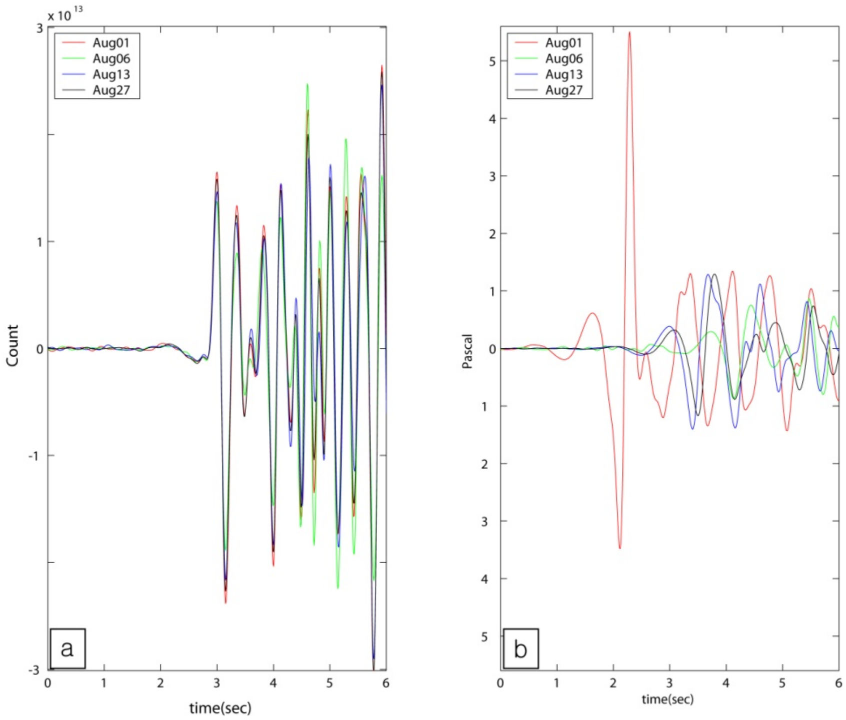

Figure 6. Comparison of waveforms and arrival times a) seismic signals and b) infrasound signals recorded at BGU

Group Velocity Estimation

The comparison of band pass filtered record sections (1.0-5.0 Hz) for the four explosions reveals that there are common characteristics in the group velocity of infrasound arrivals even though the detonation days for the four explosions are different (Figure 7). First, in all cases there are infrasound arrivals from the near-source region to 100 km (local distance range). The typical waveform in this distance range is composed of a sharp first arrival and followed by arrivals with a duration of 15 seconds. The group velocity for the first arrival in this distance range is 0.35 km/s. Second, there are no clear infrasound arrivals in the distance range from 100 to 140 km where background noise dominates the time series. This ‘zone of silence’ is relatively narrow compared to that based on the standard atmospheric model as will be demonstrated in the modeling section. Third, there are strong infrasound signals from all four explosions that arrive at regional distances from 140 to 210 km. The group velocities for these arrivals vary from 0.28 to 0.3 km/second, which is relatively slower than that of the local distance range. Multiple arrivals at this distance range are documented in a similar study in Korea and interpreted as multipath propagation of infrasound in the stratosphere (Che, 2003).

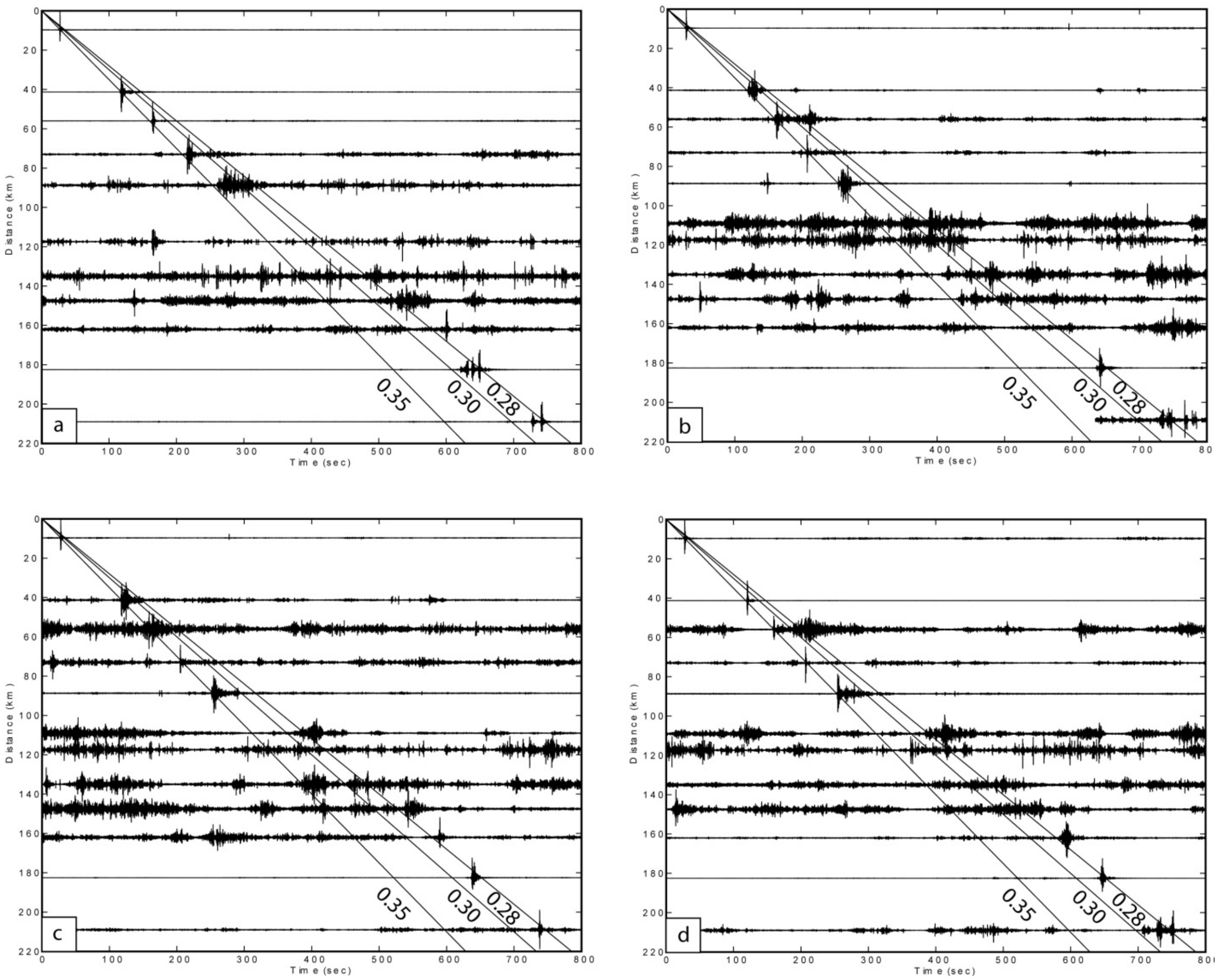

Figure 7. Band pass filtered record sections of the infrasound signals from the four detonations. a) Record section from the shot on August 1, 2007; b) Record section from the shot on August 6, 2007; c) Record section from the shot on August 13, 2007; and d) Record section from the shot on August 27, 2007.

Phase Velocity and Back-azimuth Estimation

If the wave front arriving at the array is a plane, theoretical time delay t_{ij} between array elements i and j is as follows:

$$t_{ij} = \frac{-\sin\theta(x_j - x_i) - \cos\theta(y_j - y_i)}{V}$$

where t_{ij} is the delay time, θ the back azimuth, x and y the sensor's relative coordinates to the reference coordinate, and V the phase velocity.

The delay time from data, T_{ij}, can also be attained from waveform cross-correlation. The array parameters, phase velocity and back azimuth, can be estimated with t_{ij} and T_{ij}:

$$S(\theta, V) = \min\left[\sum_{i,j} \left|T_{ij} - t_{ij}\right|^2\right]$$

For estimates of phase velocity and back azimuth from the data we used the Progressive Multichannel Cross-Correlation (Cansi, 1995) method. An example PMCC result at EPU is illustrated in Figure 8. The estimates of array parameters are summarized in Table 2 and plotted in Figure 9.

The phase velocities estimated are not faster than 0.37 km/s (Figure 9). Based on the phase velocity estimates, propagation is near the surface, possibly related to a shallow waveguide. The difference between predicted and estimated back azimuth in short distance range (<50 km) is relatively large (~5°) compared to that of regional distance around 170 km (~3°) (Figure 10).

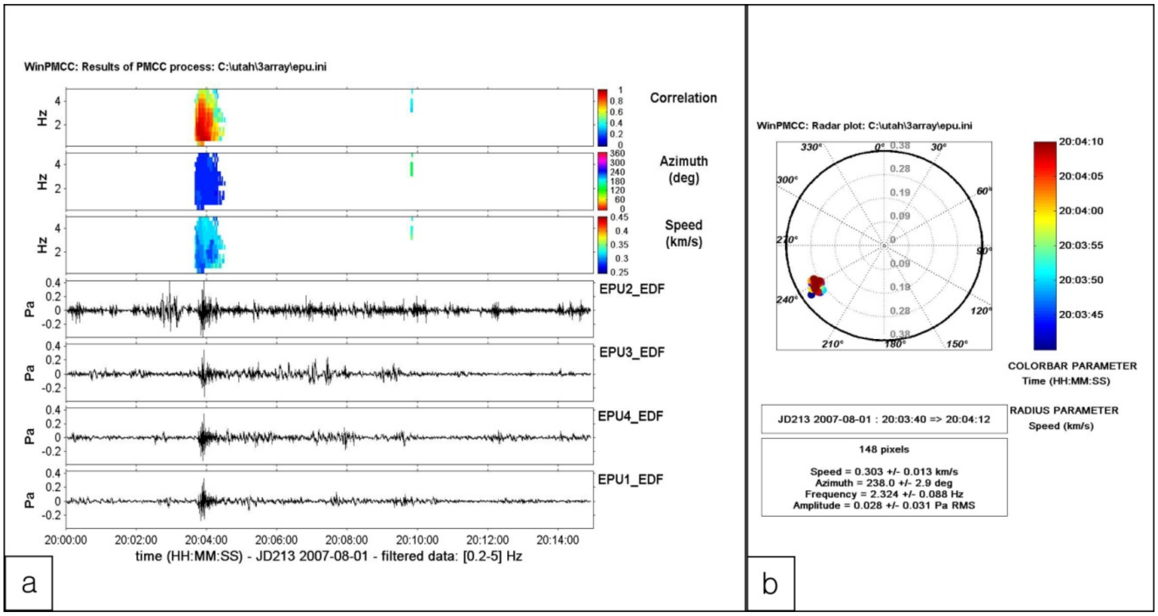

```
JD213 2007-08-01 : 20:03:40 => 20:04:12

148 pixels

Speed = 0.303 +/- 0.013 km/s
Azimuth = 238.0 +/- 2.9 deg
Frequency = 2.324 +/- 0.088 Hz
Amplitude = 0.028 +/- 0.031 Pa RMS
```

Figure 8. An example of PMCC output for the infrasound array EPU: a) Cross correlation coefficient, back azimuth and phase velocity are estimated for the detonation on August 1, 2007; b) Radar plot shows phase velocity and back azimuth estimates.

Table 2. Array Parameter Estimates at Each Array
A: Array Parameter Estimates for August 1, 2007. B: Array Parameter Estimates for August 6, 2007. C: Array Parameter Estimates for August 13, 2007. D: Array Parameter Estimates for August 27, 2007.

Array (Epicentral Distance)	A (Phase Velocity) (Back Azimuth)	B (Phase Velocity) (Back Azimuth)	C (Phase Velocity) (Back Azimuth)	D (Phase Velocity) (Back Azimuth)
BGU (26 km)	(0.362±0.008km/s) (30.9±3.7°)	(0.341±0.012km/s) (33.5±1.8°)	(0.340±0.010km/s) (32.1±4.3°)	(0.348±0.016km/s) (30.0±3.2°)
EPU (50 km)	(0.303±0.013km/s) (238.0±2.9°)	(0.298±0.008km/s) (241.7±1.1°)	(0.297±0.014km/s) (239.8±1.8°)	(0.298±0.014km/s) (238.7±1.6°)
HVU (73 km)	(0.340±0.011km/s) (193.0±2.3°)	(0.355±0.010km/s) (192.0±2.9°)	(0.351±0.011km/s) (189.4±3.6°)	(0.347±0.011km/s) (189.5±3.2°)
NOQ (84 km)	(0.288±0.005km/s) (300.0±4.0°)	(0.308±0.020km/s) (308.2±3.3°)	(0.313±0.016km/s) (311.5±3.2°)	(0.306±0.012km/s) (311.8±2.8°)
WMUT (147 km)	(0.349±0.027km/s) (324.9±5.1°)	(0.338±0.022km/s) (318.4±2.3°)	(0.312±0.019km/s) (325.3±2.1°)	(0.316±0.022km/s) (328.0±2.4°)
FSU (162 km)	(0.341±0.009km/s) (12.2±2.3°)	(0.335±0.011km/s) (11.6±2.8°)	(0.338±0.009km/s) (12.3±1.9°)	(0.346±0.014km/s) (13.2±2.8°)

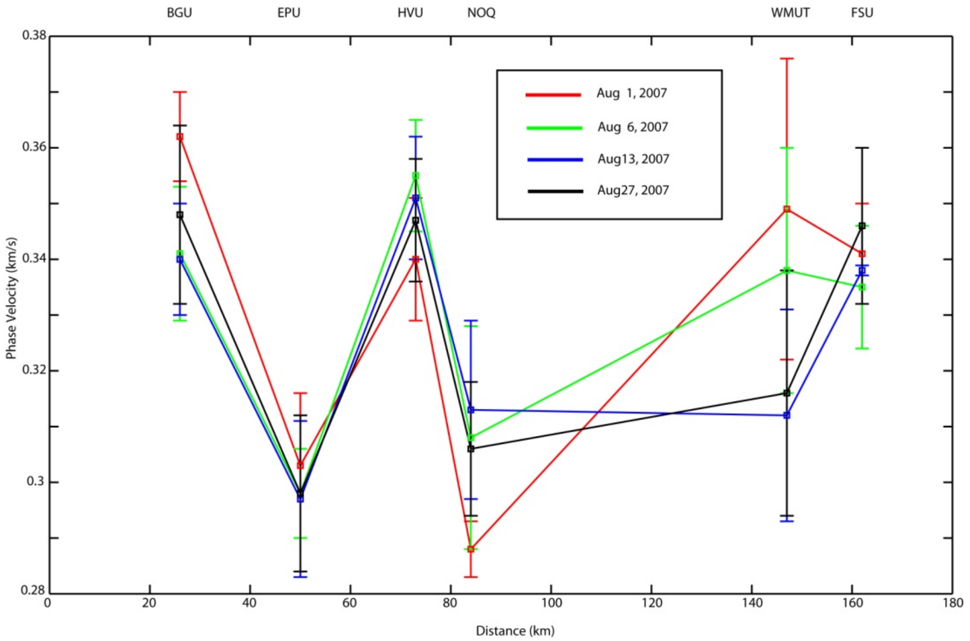

Figure 9. Variations in phase velocity estimates using PMCC are illustrated as a function of epicentral distance for the different explosions. The error estimates documented in Table 2 are expressed as error bars. The four detonations are illustrated in different colors.

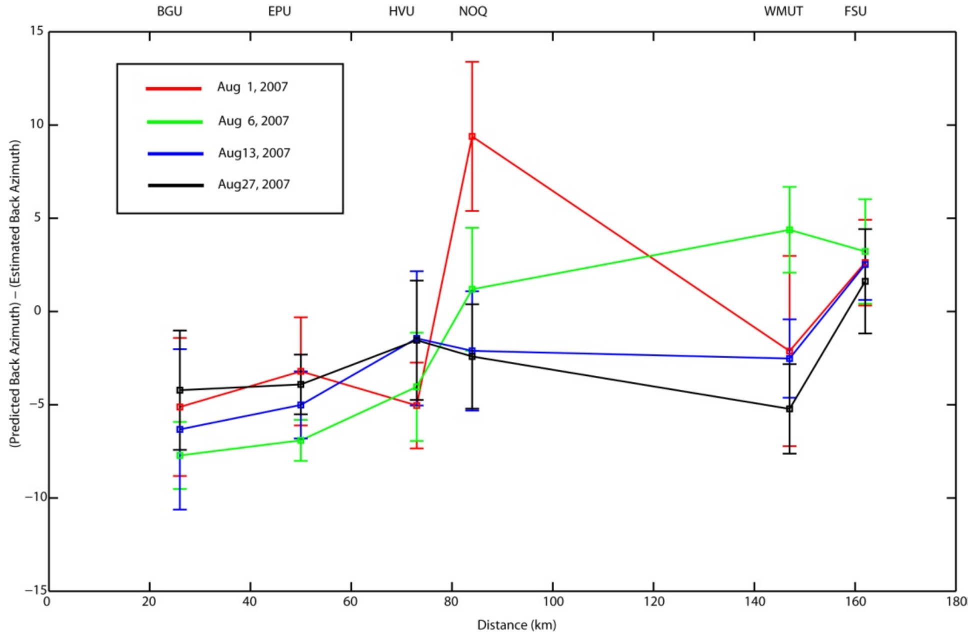

Figure 10. The difference between predicted and estimated back azimuth. The error bars and color scheme follow from Figure 9.

Travel Time Variation of Infrasound Signal at Local Distance Range

Travel time variations were observed at local distance ranges of less than 80 km, which results in variations of group velocity. The comparison between theoretical and observed group velocity variation from the four shots from stations at distances less than 80 km is illustrated in Figure 11. Similar trends between theoretical and observed group velocity implies that the first arrivals at local distance range depend on the surface temperature and local wind condition.

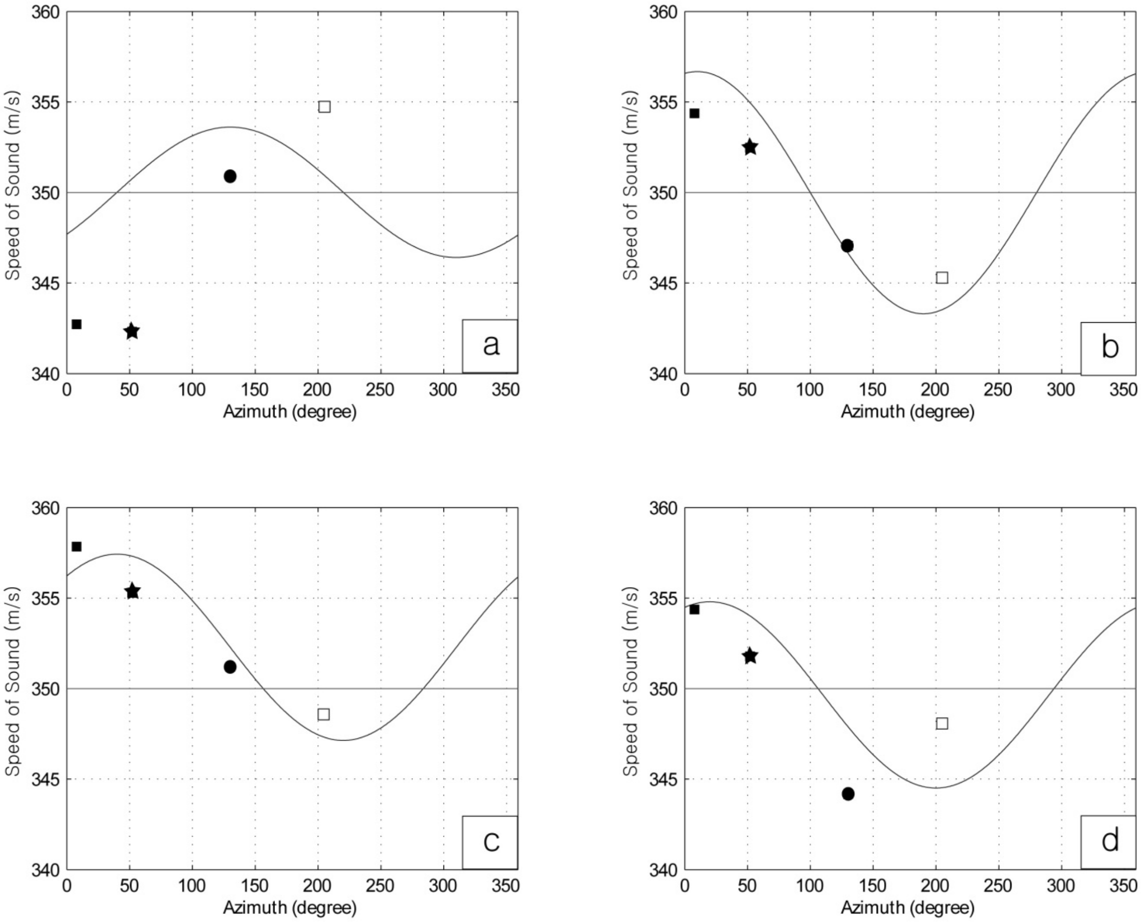

Figure 11. Comparisons between predicted speed of sound for different directions and observed infrasound group velocity from the four detonations. The blue curves represents the speed of sound calculated from the surface air temperature and winds measured at the UTTR site. Black squares are HVU (73 km). Black stars are EPU (50 km). Black circles are SNUT1 (41 km). White squares are BGU (26 km).

Amplitude Variation and Geometrical Spreading

Analysis of the observed infrasound signals documents a strong range effect on the infrasound amplitudes. The relationship between source size, infrasound amplitude and distance range has been investigated by several researchers (Reed, 1969; Clauter and Blandford, 1998; Mutschlecner et al., 1999). Reed (1969) quantified the range effect for different size atmospheric nuclear explosions. He suggested that the amplitudes decay inversely with distance; R^{-1} or $R^{-1.2}$. Clauter and Blandford (1998) proposed $R^{-1.47}$ for the decay rate at distance ranges from 200 to 10,000 km. Mutschlecner et al. (1999) considered that the effect of distance is inversely proportional to the infrasound amplitude; $R^{-1.2} \sim R^{-1.5}$ for regional distances. The observed amplitude attenuation (1-5 Hz) is near to R^{-1} with the exception of observations at 50 km and distances longer than 150 km (Figure 12).

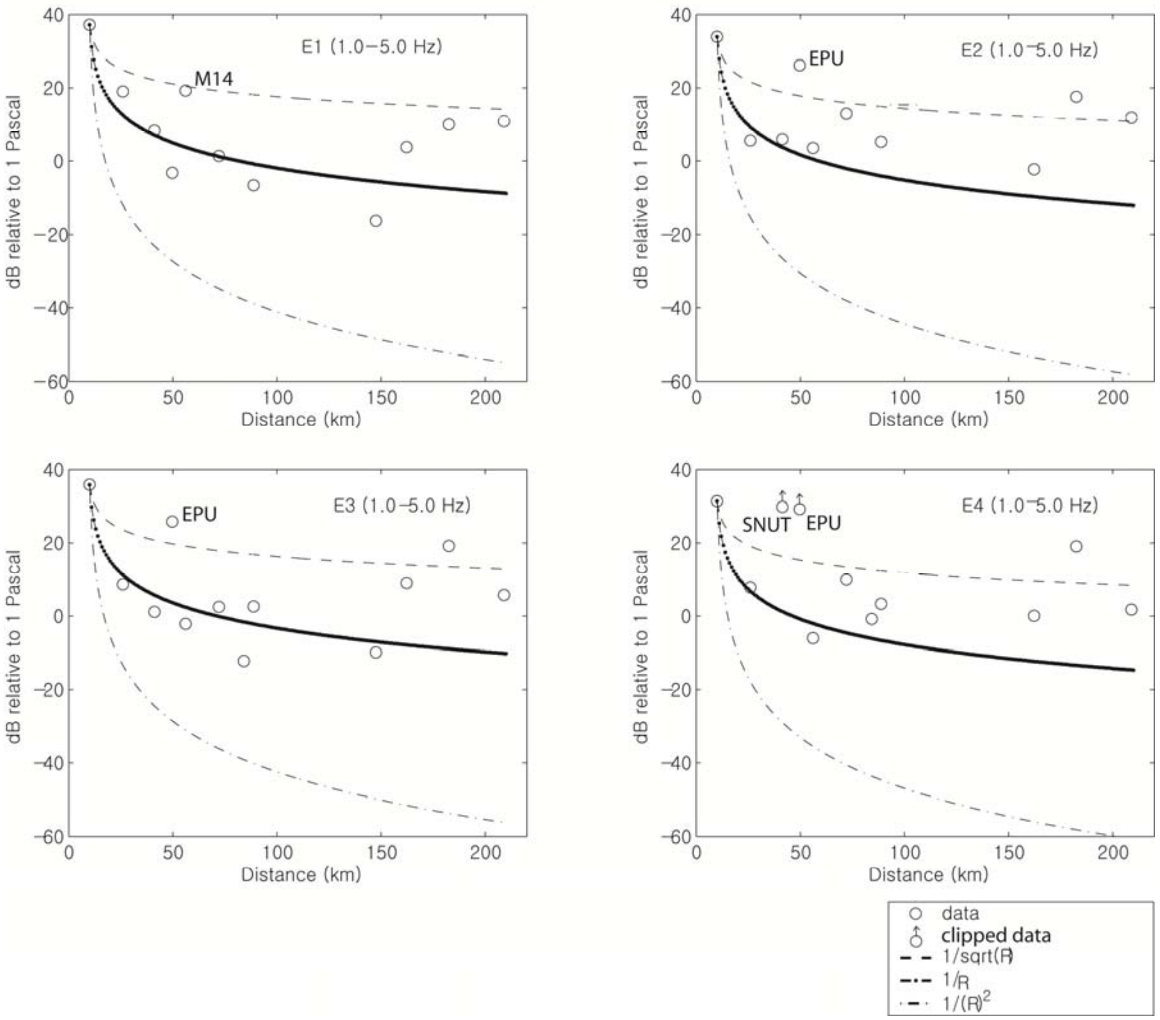

Figure 12. Attenuation of infrasound amplitude with increasing distance. E1 is the first shot. E2 is the second shot. E3 is the third shot. E4 is the fourth shot.

The data documents an increase in amplitude around 50 km (Figure 13), although the exact location of the focus changes by as much as 10 to 20 km from day to day and thus the absolute amplitude at stations in this distance range are strongly impacted for the four explosions. This focusing around 50 km is hypothesized to be due to local atmospheric structure and the propagation path of the infrasonic waves.

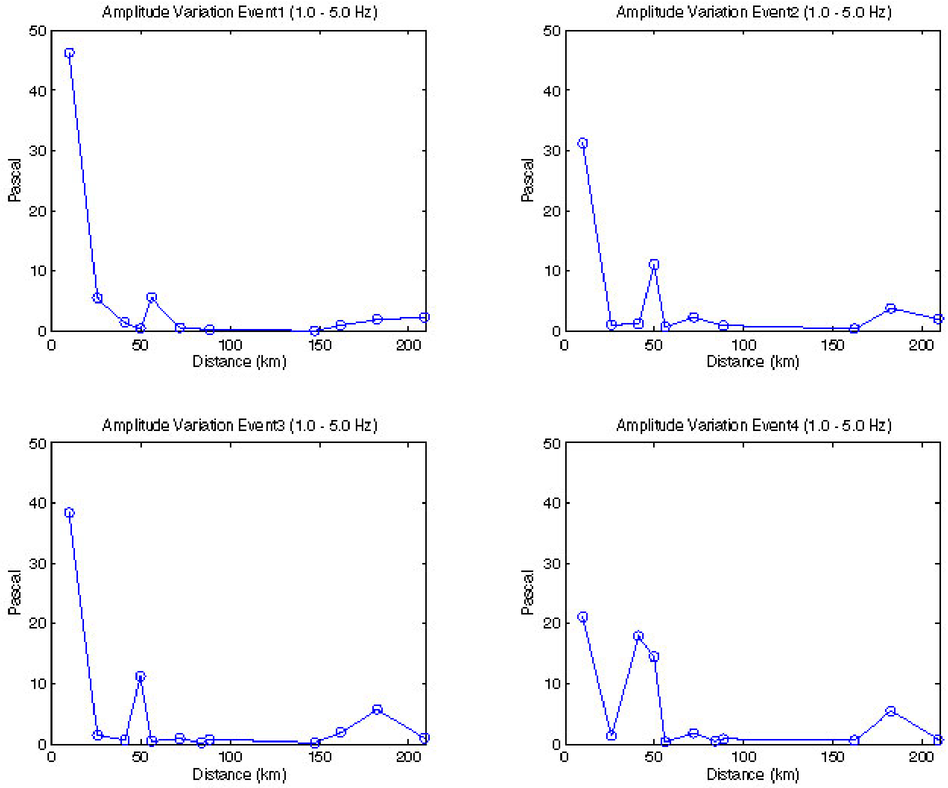

Figure 13. The figure 12 is redrawn in linear scale of amplitude for clear illustration of the amplitude anomaly around 50 km.

Modeling Study

Phase velocity estimates, variation of travel time at local distance range, waveform incoherency at the same station and amplitude anomalies around 50 km identified the possible importance of shallow waveguides to the observations in the 1-210 km distance range. The work in this section focuses on the spatial and temporal variability of these waveguides. Two approaches were undertaken to explore this variability. The first is a quantification of the spatial and temporal variation in the shallow atmosphere as sampled by the rawinsondes. The second approach involves the utilization of atmospheric models based upon the empirical data in ray tracing and PE models for the distances and azimuths for which there are infrasonic observations.

Quantification of Atmospheric Effects Including the Effect of Winds for Modeling

The infrasound recordings suggest that there may be a relationship between variation of infrasound waveform and changes in propagation path through the atmosphere. Therefore we first investigate this variation using the experimental quantification of the shallow atmosphere at the time of the four explosions.

Balloon launches were made before and at the time of each of the detonations. Launches were made at the explosion site as well as at a distance of 50 km from the source. The meteorological data is used to constrain the modeling of propagation path effects for the infrasound data. Spatial and temporal variations of atmospheric temperature and wind condition are assessed from atmospheric sampling at the time of the four detonations at the UTTR source site and at a range of 50 km as depicted in Figure 14. Variation of temperature is relatively small compared to large variations in the near-surface winds. This result illustrates the possible importance of three-dimensional effects at these distance ranges.

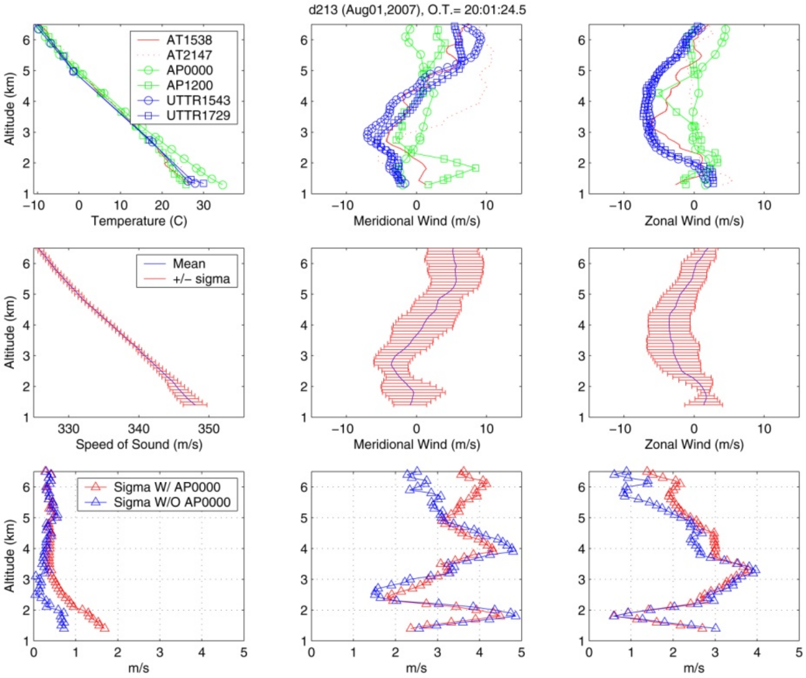

Figure 14. Atmospheric profiling was done at three sites in the region where the UTTR explosion was detonated on 1 August 2007. The first location is at the detonation site (UTTR), the second site is 50 km to the SE of the shot at Antelope Island (AP) and the final location is at the Salt Lake City airport (AP). The four digit numbers that accompany each site document the time (hours:minutes) of the atmospheric monitoring. The first row of figures represents the actual temperature, meridional and zonal winds at the three sites. The second row uses these data to create mean and variance estimates of atmospheric velocity. The third row plots the variance estimate as a function of altitude.

The temporal variation of these wind patterns is documented by comparing the results from 1 August 2007 (Figure 14) with similar data from 6 August 2007 (Figure 15). This data comparison documents the consistency of the temperature data across the three sampling sites and the large variation in winds over the first 6 km. The absolute wind values and their directions are quite different for the two days illustrating the importance of such sampling in order to quantify the wave propagation path effects.

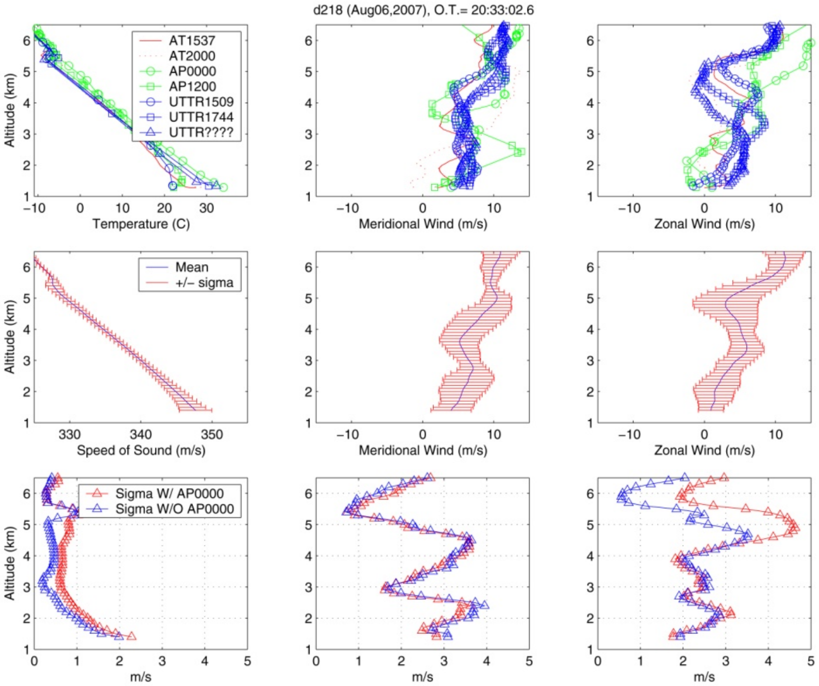

Figure 15. Atmospheric profiling was taken at three sites in the region where the UTTR explosions were undertaken 6 August 2007. Figure format is the same as in Figure 14.

Modeling of the Travel Time and Amplitude Variations of the Infrasound Signals

Ray Tracing and PE modeling was conducted using the atmospheric data in order to quantify the effects of time and space on the predicted travel times and amplitudes. The predicted effects are large in terms of predicted amplitudes from 1 to 210 km and suggest that temporal and spatial effects in the shallow atmosphere will be critical to the interpretation of the data.

Ray tracing and synthetic waveform were calculated to investigate possible ducting of infrasound energy in a shallow waveguide that produces signals at close distances. Figure 16 illustrates an example ray tracing result and the accompanying synthetic waveforms, which documents possible propagation of infrasound in the shallow waveguide at distances from the near source area to about 200 km and possible generation of the infrasound observations at 50 km.

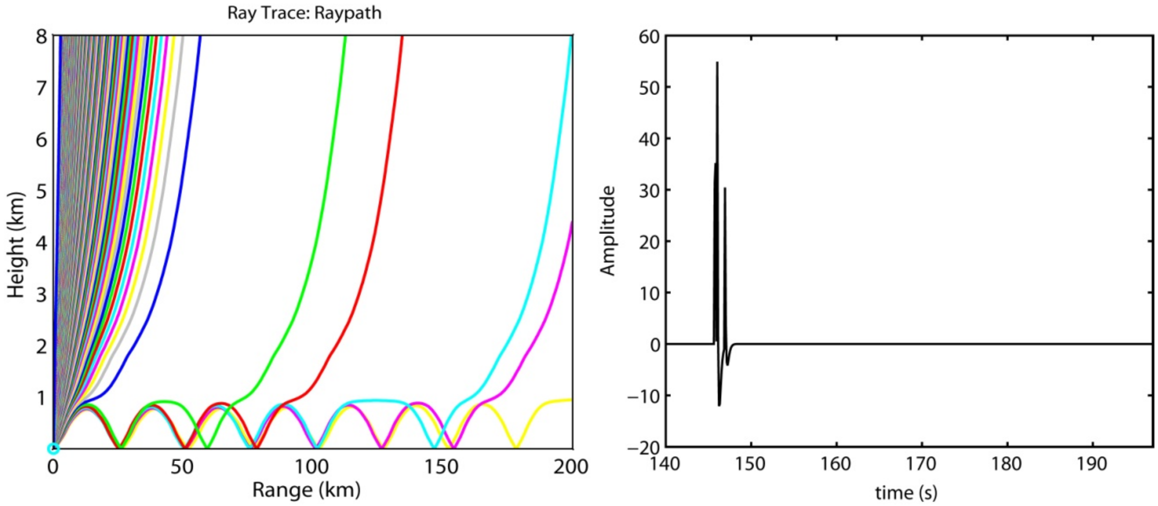

Figure 16. An example ray tracing with the atmospheric profile on 1 August, 2007 (left). The atmospheric profile from the source in the direction of 300° was used in this example. The synthetic infrasound waveform is based on the same atmospheric profile for the distance of 50 km where the observational data indicted a focusing effect (right).

Parabolic Equation Modeling

The Parabolic Equation (PE) modeling method (Lingevitch et al., 2002) using local atmospheric profiles was used to investigate the infrasound arrivals at local distance ranges and amplitude variation of infrasound signals. The software used for the modeling was InfraMAP (Norris and Gibson, 2006). Figure 17 illustrates azimuthal and temporal variations of local atmospheric structure at Antelope Island based on the empirical data for the four different days. These atmospheric characterizations were used as input into the PE modeling for comparison to the observed infrasound observations.

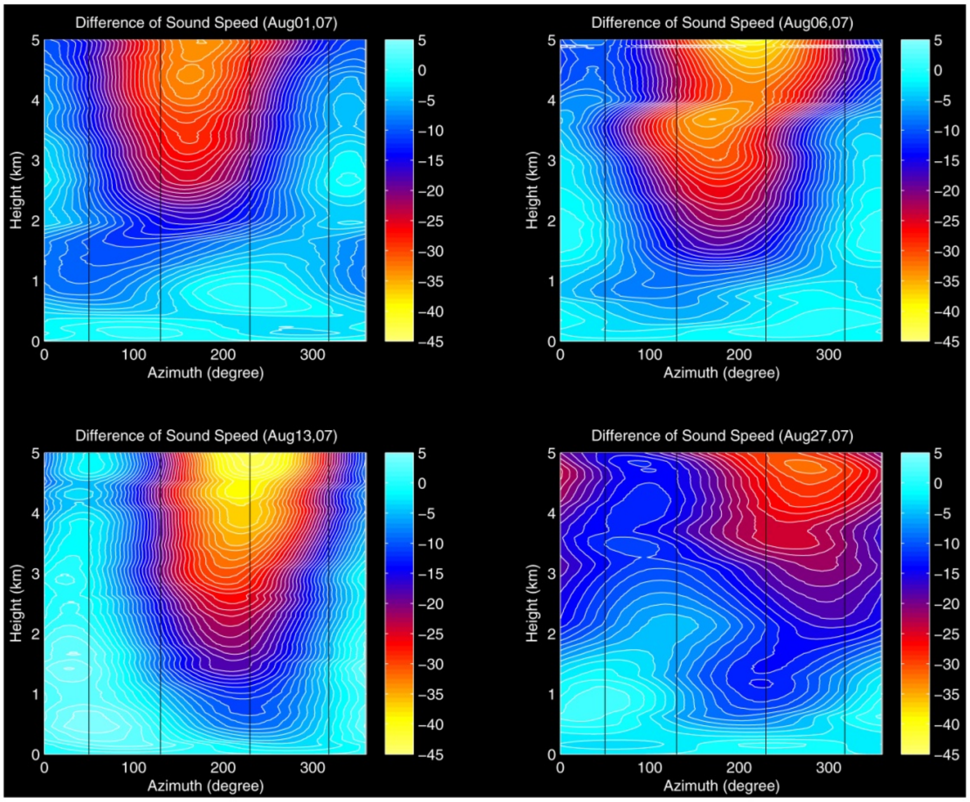

Figure 17. Azimuthal and temporal variation of local atmospheric structure for the four explosion days based on rawinsonde launched at or near the explosion time. The color scale represents the difference between the speed of sound at a specific height and that of surface (C_h-C_0, unit: m/s).

PE modeling was performed at three different frequencies (0.25, 1.0, and 3.0 Hz) using the source-station specific directions and the1-D local atmospheric structure along that direction based on the rawinsonde data summarized in Figure 17. One example of these PE solutions for Aug 01, 2007 20:00:00 GMT shows that there exist shallow ducts, 1~2 km, for acoustic energy in the near-source distances at receiver azimuths of 230° and 318° while calculations along the other two directions (50 and 180°) do not predict trapped energy (Figure 18). These results are consistent with the ranges and azimuths along which infrasound arrivals were identified in the data at local distance ranges extending to 100 km.

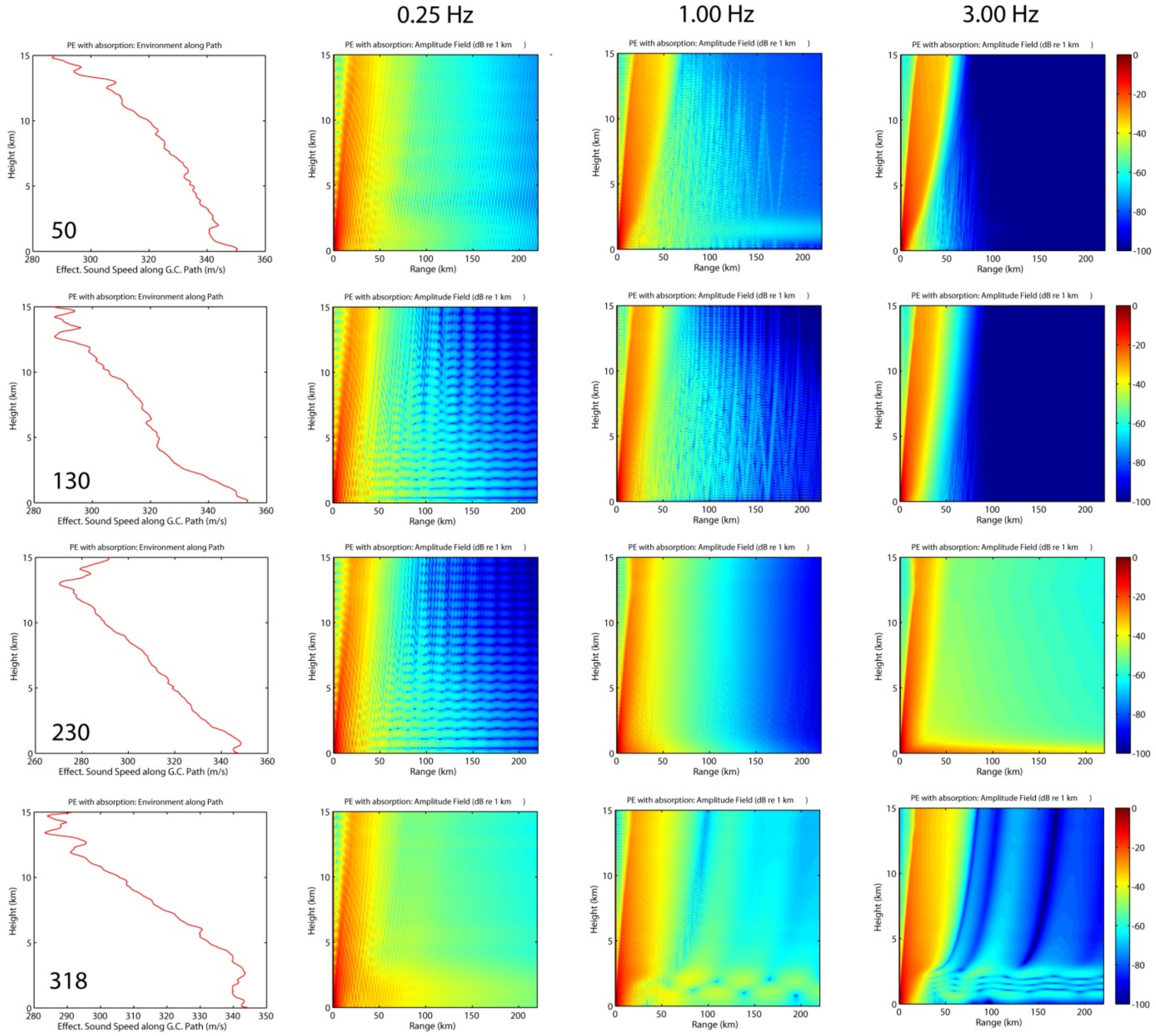

Figure 18. PE modeling for August 1, 2007 20:00:00 hour

For the three other shots, PE modeling produced arrivals from energy trapped in a shallow inverted layer between 1 and 2 km in height that were consistent with observations on those other days as well (Figure 19, 20, 21). The PE modeling suggests that observed acoustic arrivals at local distances (< 100 km) and focusing of amplitude maybe related to trapped acoustic energy between the surface and the shallow inverted atmospheric layer.

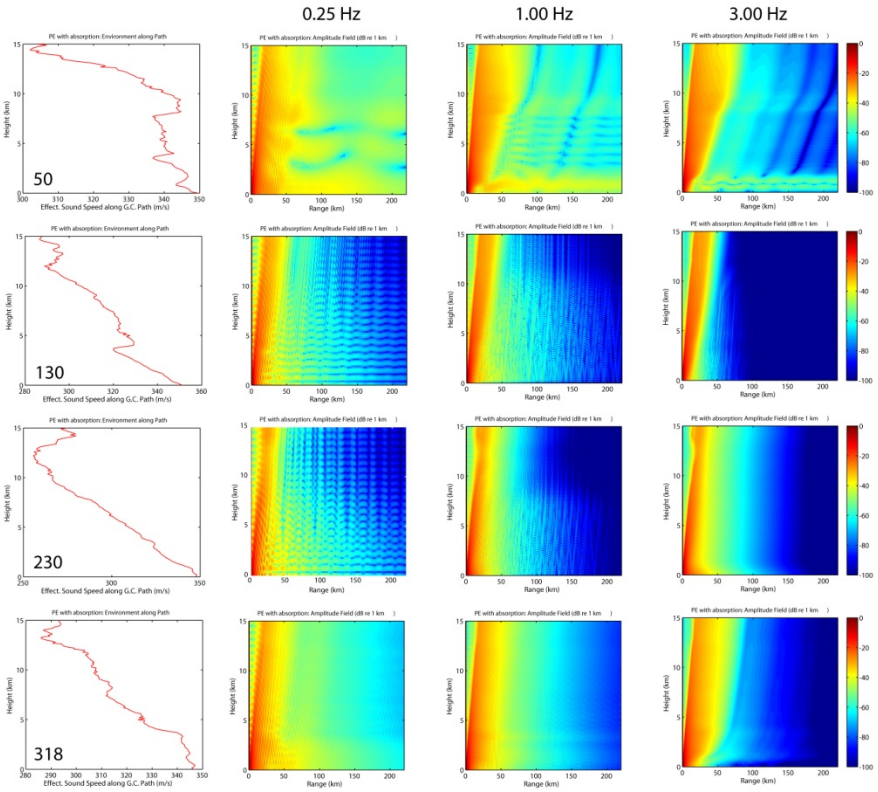

Figure 19. PE modeling for August 6, 2007 20:00:00 hour

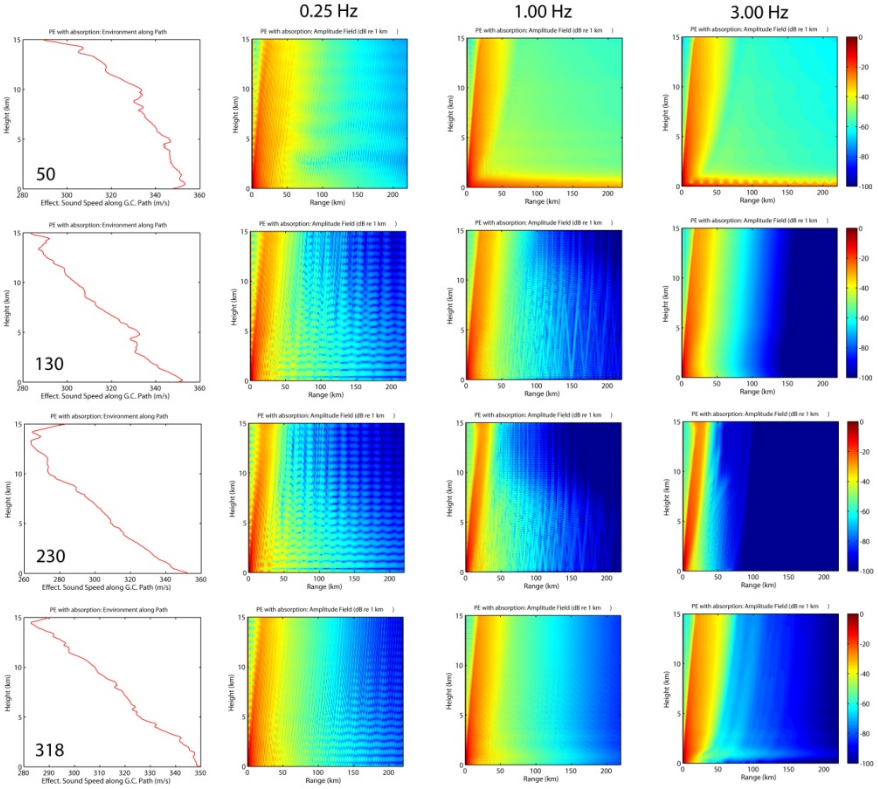

Figure 20. PE modeling for August 13, 2007 20:00:00 hour

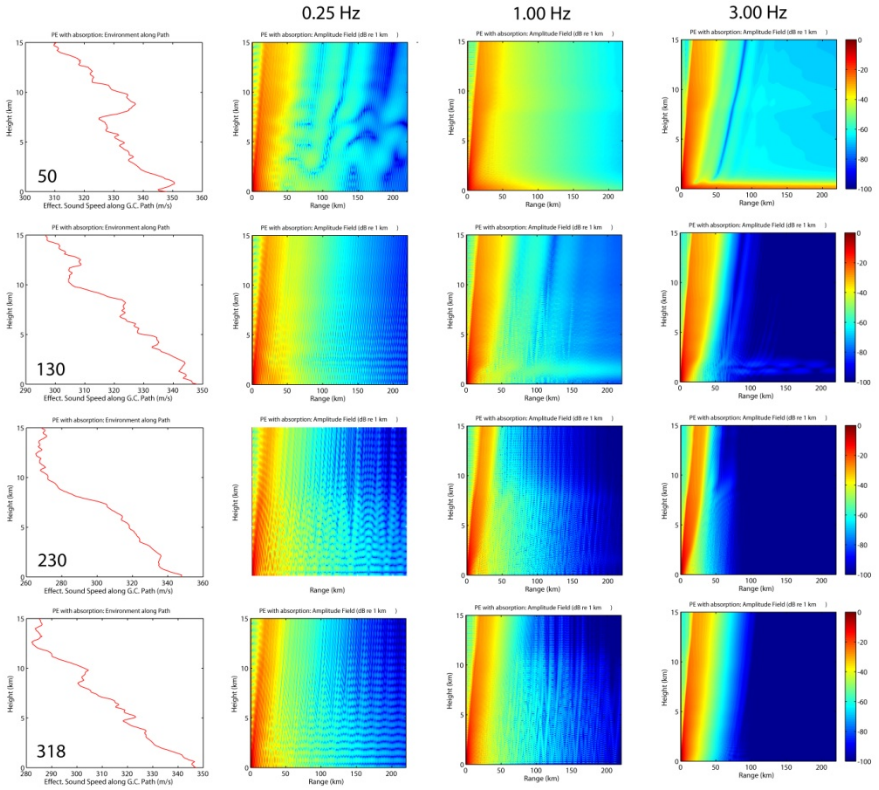

Figure 21. PE modeling for August 27, 2007 20:00:00 hour

Conclusions

Infrasound observations from the UTTR explosions show significant variability in arrival times and amplitudes from shot to shot while the seismic observations at a single station were nearly identical documenting the strong effect of atmospheric conditions on infrasonic wave propagation. Despite this variability, a number of consistencies in the infrasonic characteristics were identified and included: (1) infrasound arrivals from 100 m to 100 km composed of a sharp first arrival and followed by arrivals with a duration of 15 seconds and group velocity of 0.35 km/s; (2) No clear infrasound arrivals in the distance range from 100 to 140 km; and (3) Strong infrasound signals from all four explosions that arrive at regional distances from 140 to 210 km with group velocities from 0.28 to 0.3 km/second. The observed infrasound data at distances less than 100 km is consistent with geometrical spreading of r^{-1}.

Multiple balloon launches before and after every shot at two of the sites provides a quantification of the spatial and temporal variability of the shallow atmosphere and identifies shallow wave propagation ducts along certain azimuths that correlate with the azimuths of observations. Observed azimuthal variations in group velocity at distances of less than 100 km are also consistent with the observed wind measurements. The atmospheric data was used in a ray tracing and parabolic equation modeling exercise. The ray tracing results support the shallow waveguide interpretation for the signals observed at distances of less than 100 km and suggest a possible focusing of energy near 50 km, consistent with the amplitude data. PE models document azimuthal variation in signal strength because of winds that are qualitatively in agreement with the observations. The data, analysis and modeling at distance ranges of 0 to 100 km details the critical importance of real-time atmospheric data in data interpretation. Additional work is needed on the interpretation of the data to the farthest ranges.

References

Cansi, Y., 1995, An automatic seismic event processing for detection and location: The P.M.C.C. method, Geophysical Research Letters, 22, 1021 – 1024.

Che, I., M. Jun, J. Jeon, 2002, Analysis of local seismo-acoustic events in the Korean Peninsula, Geophysical Research Letters, 29, 12, 1029-1032.

Che, I.-Y., 2003, A Study on the Discrimination between Earthquakes and Artificial Explosion by using Cheorwon Seismic and Infrasound Array Data, Yonsei University, Ph. D. thesis, pp 157.

Clauter, D. and R. Blandford, 1998, Capability Modeling of the Proposed International System 60-Station Infrasonic Network, Los Alamos National Laboratory report LA-UR-98-56.

Evers, L.G., L. Ceranna, H.W. Haak, A. Le Pichon and R.W. Whitaker, A seismoacoustic analysis of the gas-pipeline explosion near Ghislenghien in Belgium, Bulletin of the Seismological Society of America, vol 97 no 2, 417-425, 2007. doi:10.1785/0120060061.

Lingevitch, J.F., M. D. Collins, D.K. Dacol, D.P. Drob, J.C. W. Rogers, and W. L. Siegmann, 2002, Parabolic Equations for Atmospheric Waves, research articles in NRL Review, Acoustics.

Mckenna, M. H., 2005, Infrasound wave propagation over near-regional and tele-infrasonic distances, Ph. D thesis at Southern Methodist University.

Mutshlecner, J. P., R. W. Whitaker, and L. H. Auer, 1999, An Empirical Study of Infrasound Propagation, Los Alamos National Laboratory report LA-13620-MS.

Norris D. and R. Gibson, 2006, User's Guide for InfraMAP (Infrasound Modeling of Atmospheric Propagation), Version 5.1, BBN Technical Memorandum W2078.

Pinsky, V., Y. Gitterman, A. Hofstetter and A. Shapiro, 2006. Robust location of surface explosions by a network of acoustic arrays, *Geopys. Res. Lett*, *Vol. 33*, L02317, 5PP., 2006. doi:10.1029/2005GL024304.

Reed, J. W., 1969, Climatology of Airblast Propagations from Nevada Test Site Nuclear Airbursts, Sandia Laboratories report SC-RR-69-572.

Stump, B., R. Burlacu, C. Hayward, K. Pankow, S. Nava, J. Bonner, S. Hoch, D. Whiteman, A. Fisher, T. S. Kim, R. Kubacki, M. Leidig, J. Britton, D. Drobeck, P. O'Neill, K. Jensen, K. Whipp, G. Johanson, P. Roberson, R. Read, R. Brogan and S. Masters, 2007, Seismic and Infrasound Energy Generation and Propagation at Local and Regional Distances: Phase I-Divine Strake Experiment, Air Force Research Laboratories report AFRL-RV-HA-TR-2007-1188, 11 October 2007, Hanscom AFB, MA 01731-3010.